Erlangen Centre for Astroparticle Physics

Systematic Errors of a 3D Template Background Model for IACTs and its Application to the Galactic Center

Systematische Fehler des 3D Untergrund Modells fuer IACTs und die Anwendung auf das Galaktische Zentrum

Der Naturwissenschaftlichen Fakultät
der Friedrich-Alexander-Universität Erlangen-Nürnberg
zur Erlangung des Doktorgrades Dr. rer. nat.

September 19, 2023

vorgelegt von
M.Sc. Kaori Nakashima
aus Maringa - Brasilien

Als Dissertation genehmigt von
der Naturwissenschaftlichen Fakultät der
Friedrich-Alexander-Universität Erlangen-Nürnberg

Tag der mündlichen Prüfung:	24.07.2023
Gutachter:	Prof. Dr. Stefan Funk

To all those who believe in the scientific method.

"The size and age of the Cosmos are beyond ordinary human understanding.
Lost somewhere between immensity and eternity is our tiny planetary home.
In a cosmic perspective, most human concerns seem insignificant, even petty.
And yet our species is young and curious and brave and shows much promise.
In the last few millennia we have made the most astonishing and unexpected discoveries
about the Cosmos and our place within it, explorations that are exhilarating to consider.
They remind us that humans have evolved to wonder,
that understanding is a joy, that knowledge is prerequisite to survival.
I believe our future depends on how well we know this Cosmos
in which we float like a mote of dust in the morning sky."
— Carl Sagan, Cosmos

Abstract

The simultaneous spectral and morphological analyses in complex regions in Imaging Atmospheric Cherenkov Telescopes data became possible due to the recently developed 3D template background model.
However, the capabilities of the model are partially restricted by systematic errors, particularly at low energies. Due to these uncertainties, the energy range of the analysis is usually shortened. A proper assessment of the model's systematic errors can validate its accuracy. Nevertheless, to date there is no general method of estimating it.

This work presents a method for calculating the systematic errors of a 3D template background model, which also includes the error for any dataset and improvements in the analysis due to the convolution of the error in the maximum likelihood computation. The method generates lookup tables with the expected level of systematic error for the background model per run, in energy bins. By construction, the method is applicable to any version of a 3D template background model and any dataset and the produced lookup tables can be used regardless of the origin of the error for estimating the error of any dataset.
This work presents the improvement of incorporating systematic errors in analysis, through nuisance parameters and it is validated on a Crab Nebula dataset. This procedure widens the energy range towards low energies and provides a more accurate background estimation, and consequently a better characterization of the region in the analysis.

The origins of the highest levels of systematic errors presented in the method are explored. The first one, caused by the spatial miss modeling at low energies, is a generic issue arising from the model's construction method and it is likely to appear in other versions. The second one, caused by the technique used for gamma-hadron separation intrinsic to this specific model version.

Finally, this framework was applied to spectral variability studies of the Galactic Center central source HESS J1745–290 in the TeV range, with H.E.S.S. data, including systematic errors in the 3D template background model. Motivated by the common analysis method, the corresponding source 4FGL J1745.6–285 observed by Fermi-LAT in the GeV range was included in this study. As a result of this investigation, no statistically significant spectral variability was observed nor was a correlation between the data from the different experiments. These results place constraints on two astrophysical models that predict spectrum variability due to flaring episodes from the central Super Massive Black Hole Sgr A* on a 15 year time scale.

Zusammenfassung

Das kürzlich entwickelte 3D-Vorlagen-Untergrundmodel ermöglichte die gleichzeitige spektrale und morphologische Analyse komplexer Regionen in den Daten von Imaging Atmospheric Cherenkov Telescopes. Durch unbekannte systematische Fehler, insbesondere bei niedrigen Energien, sind die Möglichkeiten des Modells jedoch eingeschränkt. Aufgrund dieser Unsicherheiten ist dieser Energiebereich in der Regel aus der Analyse ausgeschlossen. Eine angemessene Bewertung der systematischen Fehler des Modells kann seine Genauigkeit bestätigen. Bislang gibt es jedoch keine allgemeine Methode zur Abschätzung dieser Fehler.

In dieser Arbeit wird eine Methode zur Berechnung der systematischen Fehler eines 3D-Vorlagen-Untergrundmodells vorgestellt, die auch den Fehler für jeden Datensatz und Verbesserungen in der Analyse aufgrund der Berücksichtigung des Fehlers in der Maximum-Likelihood-Berechnung umfasst. Das Ergebnis der Methode sind Nachschlagetabellen mit der erwarteten Magnitude des systematischen Fehlers für das Untergrundmodell pro Observation und innerhalb bestimmter Energiebins. Die Methode ist unabhängig vom Ursprung des Fehlers und kann auf jede Version eines 3D-Vorlagen-Untergrundmodells und auf jeden Datensatz angewendet werden. In dieser Arbeit wird die Verbesserung einer Analyse durch die Einbeziehung von systematischen Fehlern durch Nuisance-Parameter vorgestellt und anhand eines Crab-Datensatzes validiert. Das Verfahren erweitert den Energiebereich in Richtung niedriger Energien und bietet eine genauere Untergrundabschätzung und folglich eine bessere Charakterisierung der Region in der Analyse.

Die Ursachen für die höchsten systematischen Fehler in der Methode werden untersucht. Der erste Fehler, der durch die räumliche Fehlmodellierung bei niedrigen Energien verursacht wird, ist ein allgemeines Problem, das sich aus der Konstruktionsmethode des Modells ergibt und wahrscheinlich auch in anderen Versionen auftritt. Das zweite Problem, das durch die Methode der Gamma-Hadron-Trennung verursacht wird, die für diese Modellversion verwendet wird, ist für diese spezielle Version charakteristisch.

Schließlich wurde diese Untersuchung auf Studien zur spektralen Variabilität der zentralen Quelle HESS J1745–290 im Galaktischen Zentrum mit H.E.S.S.-Daten angewendet. Es ist das erste Mal, dass diese Quelle in einer 3D-Analyse untersucht wurde, die systematische Fehler im 3D-Vorlagen-Untergrundmodell berücksichtigt. Im benachbarten Energiebereich wurde, motiviert durch die gemeinsame Analysemethode, die von Fermi-LAT beobachtete Quelle 4FGL J1745.6–285 in diese Studie einbezogen. Als Ergebnis dieser Untersuchung wurde bei keiner der Quellen eine statistisch signifikante spektrale Variabilität beobachtet, und es gab auch keine Korrelation zwischen den Daten der verschiedenen Experimente. Diese Ergebnisse ermöglichen die Überprüfung von zwei astrophysikalischen Modellen, die eine Spektralvariabilität aufgrund von ausbrechenden Episoden von Sgr A* innerhalb eines Zeitraums von 15 Jahren vorhersagen.

Contents

1 Motivation

Gamma rays are the highest part of the electromagnet spectrum, ranging from 100 keV to PeV energies. They access the most extreme environment in the cosmos and are produced during the interaction of accelerated charged particles with ambient fields. Due to the gamma-ray charge neutral feature, its incoming direction is traceable allowing the identification of the direction of the acceleration sites.

The abundance of these photons usually decreases with energy, for the standard candle gamma-ray source, the Crab Nebula, it is expected 1 photon per m^2 per second with 1 TeV energy. Due to the different available statistics with energy, different measurement techniques must be adopted, and they are in order of increasing energy: satellites, Imaging Atmospheric Cherenkov Telescopes (IACTs), and water tank experiments. They characterize the measured gamma-ray in four parameters, two spatial coordinates, its energy, and its time of detection.

With these four parameters, the gamma rays together with other wavelengths and other messengers, assist in shedding light onto the universe. For instance, a common underlying astrophysical model may predict different multi-wavelengths and/or multi-messengers.

For the IACT realm, the classical analysis techniques analyze either morphology or the spectrum of the source of interest; the simultaneous spectral-morphological analysis is not affordable. This was due to the lack of statistics for a proper estimation of the background. Although the classical techniques are sufficient for some source categories, it faces challenges for crowded regions, with overlapping sources and/or extended sources. This issue is solved with a new background estimation, consisting of a 3D template model, which uses a maximum likelihood analysis. This opens up the opportunity to analyze simultaneously the morphological and spectral features of any region, by calculating the probability of the data and the expected signal from input models in each spatial and energy coordinate. This new approach, besides solving the statistical issue, also converges the satellite and IACT analysis methods. Since the model is a novelty, its systematic errors are yet poorly understood.

A correct assessment of the systematic error allows the full capability of the model and the analysis method usage. Currently, systematic errors in the background model are specific to the individual analysis and not a generic scheme for estimation, hampering the comparison of models and results. Ideally, it is desired a unified method of systematic error estimation of a background model, and this is shown in chapter 3 of this work.

The applicability of the presented method and proper incorporation of it in the maximum likelihood analysis is applied in the Galactic Center (GC) region for the study of the source HESS J1745–290. The GC is a unique laboratory, it embeds different astrophysical sources in intense and diverse ambiance fields, creating fertile conditions to trigger many physical mechanisms. The complexity of the region required adaptive classical background estimations. However, no further adjustment is needed for the 3D analysis, since it naturally handles complex regions with multiple input models.

Within the H.E.S.S. spatial resolution, the HESS J1745–290 emission has two current candidates responsible for emission, the Super Massive Blach Hole (SMBH) Sagittarius A* and the Pulsar Wind Nebula (PWNe). The spatial resolution, at the limit of its capability, does not provide any further inputs to solve the source confusion. One alternative is the increased statistics over the years. A time variability analysis of the gamma-ray spectrum could favor Sgr A* flaring emission, over the steady emission of the PWNe.

Due to the adjacent energy range, the connection of GeV-TeV emission could assist in the description of the region and in the underlying astrophysical processes. To date, the Fermi-LAT and the H.E.S.S. emission present independent and distinct gamma-ray spectrum from the GC center, and there is no clear correlation between them.

In this work, the chapter 2.2 is devoted to a literature overview, which includes the physical process leading to gamma-ray production, overview of the gamma-ray instruments and the analysis techniques, with focus on Fermi-LAT and H.E.S.S. observatories, and an introduction about the GC environment.

The chapter **??** is dedicated to systematic studies of a 3D template background model. It introduces a general method to estimate the systematic errors for any model version, and a procedure to use it in the estimation of systematic errors due to the background model of any dataset. Additionally, it is presented an option to include the systematic error in the analysis via nuisance parameters. The enhancement in the analysis is presented by testing it on a Crab dataset.

The chapter 4 is devoted to the investigation of the spectral variability of the GC central source, 4FGL J1745.6–2859 from Fermi-LAT data and HESS J1745–290 for H.E.S.S.. For the latter source, the analysis pipeline introduced in the chapter is applied. For completeness, a discussion about the correlation search between the spectra is presented. Finally, the implication of these results in astrophysical models and contributions to the astrophysics context is discussed.

2 General Overview

2.1 Introduction

Gamma rays are the highest energy photons in the electromagnetic spectrum, ranging from 100 keV up to at least 1.4 PeV, the currently highest energy gamma-ray measured [1]. Since their production requires extremely high energies, the study of gamma rays opens up the door to understanding the most violent events and environments in the cosmos, which is inaccessible on Earth.

Gamma-ray astronomy started with its first measurement in the second half of the 20th century [2], being relatively young when compared to the history of other wavelengths. Nevertheless, in this short time period, the gamma-ray field has grown unstoppably reaching a robust level for experiments and analysis techniques. One milestone that elucidates the advancement of this field is the sky map seen in gamma rays shown in the cover image of this chapter above*. This measurement was carried out by the Large Area Telescope (LAT) [3], on board of the *Fermi* satellite. The sky map reveals the wealth of the gamma-ray sky, presenting many different and complex structures.

Due to the charge-neutral characteristic of gamma rays, they are not deflected by magnetic fields when traveling through the interstellar medium, in contrast to charged particles. Therefore, their incoming direction points back to the source position. Alongside the spatial coordinates, other properties, such as photon energy and arrival time, are typically obtained with gamma-ray telescopes. Based on these three quantities (spatial, energy, and time), the observation of gamma rays deepens our understanding of the cosmos.

For instance, gamma rays are produced in the same sites where Cosmic Rays (CR) are accelerated and therefore gamma rays assist in the understanding of the origin and acceleration

* Further details about the image: Gamma-ray sky map observed by *Fermi*-LAT from August 2018 to May 2021. The map is divided into RGB colors, with low energy gamma rays shown as red, middle energy gamma rays in green, and high energy in blue. Credit: D. Carlos, L. Siconato, R. de Menezes, R. Nemmen from the University of Sao Paulo, taken from back hole group.

mechanisms of CR. Gamma rays also endorse underlying physical models derived from other wavelengths, such as the model for the Crab Nebula [4, 5]. Gamma rays can also falsify physics theories such as Lorentz Invariance Violation [6, 7] or Dark Matter models [8, 9]. Additionally, gamma rays are also a crucial astrophysical messenger that together with gravitational waves [10] and neutrino measurements [11] provide a complete picture of high energetic astrophysical events [12].

This chapter is divided into three main sections. Section 2.2 describes the physical process for gamma-ray production from the interaction of high-energy CRs with the interstellar environment. Section 2.3 describes the instruments for gamma-ray detection, focusing on *Fermi*-LAT and H.E.S.S. experiments. Lastly, section 2.4 describes the Galactic Center region observed in gamma rays.

2.2 The Physical Processes for Gamma-ray Production

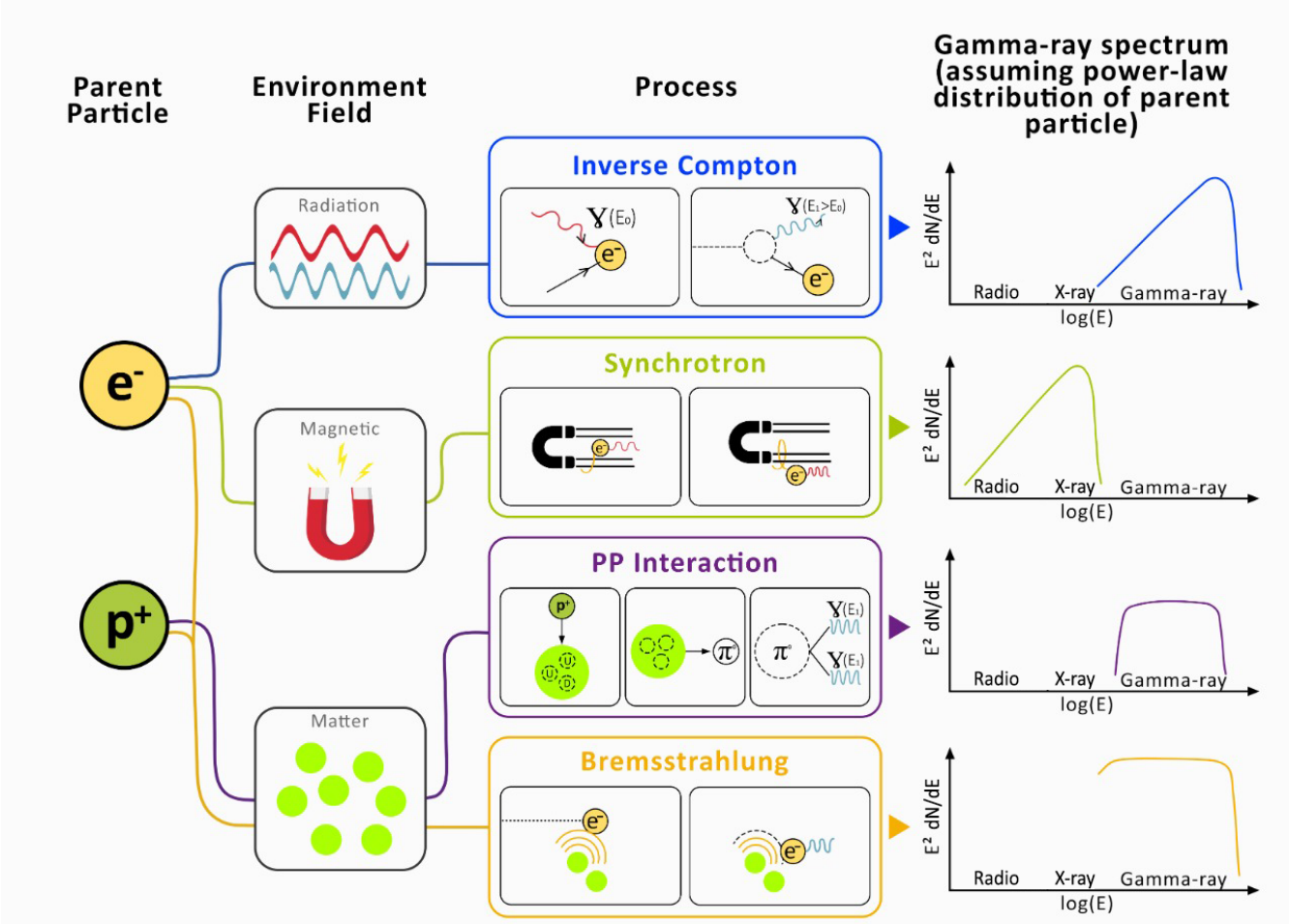

Figure 2.1: Overview of the physical processes for gamma-ray production. Courtesy from: Ayumi Nakashima.

The interaction of CR with ambient field causes a cooldown of these particles and as a byproduct, gamma rays are emitted.

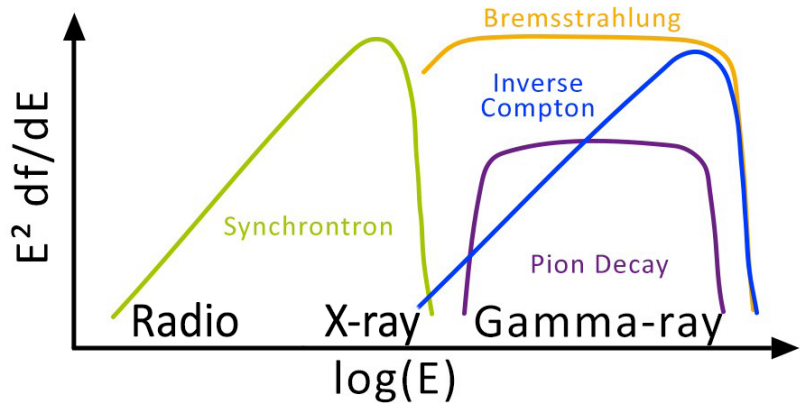

Figure 2.2: Compilation of electromagnetic spectra shape for each physical mechanism presented in figure 2.1.

The main ingredient for gamma-ray emission is protons and/or electrons. Thus, the physical models describing the measurements are, often, classified on the nature of the primary particle, namely leptonic and hadronic scenarios.

There are three main types of ambient fields with which the CR are usually interacting: radiation, magnetic, and matter fields. Although a different physical process is responsible for cooling in each field, they are subject to their respective energy loss equation, and is described following sections. From the energy loss equation, the emitted gamma-ray spectrum and the cooling time is derived — i.e. the time scale for the parent particle to lose $1/e$ of its initial energy — and indicate the efficiency of the process. Each of these variables, energy loss, cooling time, and emitted gamma-ray spectrum, is unique for each type of cooling mechanism, which is tightly dependent on the interacting field features.

In a realistic astrophysical source, individual charged particle interacting with the ambient fields contributes to the final emitted gamma-ray spectrum. Thus, features of the measured spectrum resemble environmental conditions.

In a realistic astrophysical source, each particle, part of a distribution of accelerated particles, contributes to the final emitted gamma-ray spectrum. Thus, features of the measured spectrum resemble environmental conditions.

An illustration of all relevant processes for the gamma-ray production is shown in figure 2.1. The first column represents the type of parent particle, the second column the environment field, the third column shows an illustration of the physical cooling mechanism, and the last column shows the expected shape of the gamma-ray spectrum associated with this process when assuming a distribution of parent particles.

The features in the resulting gamma-ray spectrum are linked to the particular process. Figure 2.2 compares and puts into perspective the energy scale of the different spectra shown

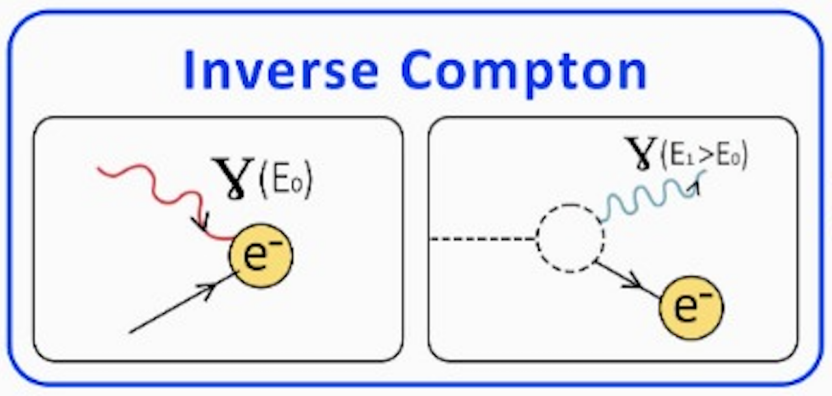

Figure 2.3: Overview of Inverse Compton mechanism. Courtesy of Ayumi Nakashima.

in figure 2.1. For instance, the low energy cutoff for p-p interaction is at well-defined energy, i.e. slightly above the neutral pion mass, and independent of the external features, thus, the absence of this cutoff in a measured spectrum could rule out the p-p model. Another interesting feature observed is the energy regime in which each mechanism is dominant. For instance, Inverse Compton is more relevant for higher energies while the Synchrotron process shines at lower energies, being also relevant for the X-rays range. Additionally, the high energy cutoff connects the maximum acceleration of the parent particle.

In a typical astrophysical scenario, different cooling mechanisms occur simultaneously and/or compete with each other. Hence, the measured gamma-ray spectrum is often a compilation of different processes. However, the correct disentanglement of each contribution is challenging, especially in crowded regions, as in the Galactic disk.

The processes described in figure 2.2 are treated in detail in the following sections. Unless clearly stated, the well-established physical knowledge is based on textbooks [13, 14, 15]. It is worth mentioning that, there are also alternative hypotheses for gamma-ray production, such as due to Primordial Black Holes [16] and Dark Matter annihilation [8], however, they are not in the scope of this work.

2.2.1 Process: Inverse Compton

Inverse Compton - Short Description
Scattering of a relativistic electron with a low energy photon, in which a fraction of the electron's energy is transferred to the photon. It is very efficient for the production of the highest energy photons. This process can be classified according to the energy of the interaction. In the Thomson regime, the exchanged energy is negligible compared

to the electron kinetic energy. In the Klein-Nishina (KN) regime, the amount of exchanged energy is comparable to the electron's kinetic energy. The electron cross-section for this interaction can be described by the KN formula and in the limit of low energies, it is reduced to the classical Thomson cross-section. The cross-section in the KN regime is dependent on the scattered angle and it is strongly suppressed at high energies. An illustration of the process is shown in figure 2.3.

The energy loss equation for the different regimes can be described as:

$$\left(-\frac{\mathrm{d}E_e}{\mathrm{d}t}\right)_{\mathrm{IC,Thomson}} = \frac{4}{3}\sigma_T c\omega_0 n_{\mathrm{ph}}\epsilon_e^2 = \sigma_T c u'_{\mathrm{rad}} \tag{2.1}$$

$$\left(-\frac{\mathrm{d}E_e}{\mathrm{d}t}\right)_{\mathrm{IC,KN}} = \frac{3}{8}\frac{\sigma_T c n_{\mathrm{ph}}}{\omega_0}(\ln(4\omega_0\epsilon_e) - 11/6) \tag{2.2}$$

where the terms are the classical Thomson cross-section, σ_T, the density of the photon field, n_{ph}, the incoming photon energy, ω_0, the electron's energy (in units of $m_e c$), ϵ_e, and the energy density of radiation field in the rest frame of the electron, u'_{rad}.

The two regimes behave completely differently, due to the different dependency of the energy loss equation with ϵ_e. The energy lost by the electron in the KN regime is discrete and comparable to electron kinetic energy, consequently, only a few collisions are enough to result in efficient cooling. On the other hand, in the Thomson regime, the electron loses a negligible fraction of its energy in each collision, therefore the cooling process requires several interactions. The cooling time for each regime is described by equations 2.3 and 2.4. For both equations, the cooling time depends on the electron's energy ϵ_e, however only in the Thomson regime there is a dependency on the density of the radiation field u'_{rad}, showing the necessity of several interactions to cool the electron down.

$$\tau_{\mathrm{IC,\ Thomson}} \propto \left(\frac{u'_{\mathrm{rad}}}{\mathrm{eV\ cm^{-3}}}\right)^{-1}\left(\frac{\epsilon_e}{\mathrm{GeV}}\right)^{-1}\ \mathrm{yr}. \tag{2.3}$$

$$\tau_{\mathrm{IC,KN}} \propto \frac{\epsilon_e}{\ln(\epsilon_e)}\ \mathrm{yr}. \tag{2.4}$$

The time evolution of an electron's energy has the shape represented in figure 2.4. The first interaction happens in the KN regime, in which the electron loses large amounts of energy, which causes the emission of the highest energy

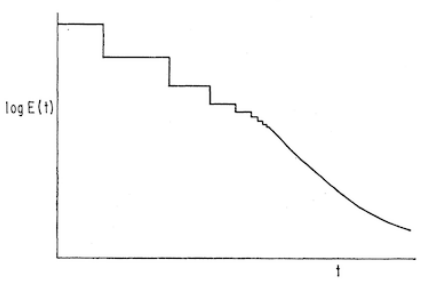

Figure 2.4: Electron energy in time for the IC cooling process. The image is taken from [14].

gamma rays. This mechanism is also responsible for the highest gamma-ray ever measured [1]. As the electron cools down, it behaves according to the Thomson regime and the cooling occurs via many interactions with small energy exchange.

When considering an initial distribution of parent particles as a power-law with index p, the emitted radiation spectrum behavior is shown in equations 2.5 and 2.6. An illustration of the shape of the expected gamma-ray spectrum is shown as the blue line in figure 2.2.

$$\frac{\mathrm{d}N_{\gamma,\mathrm{Thomson}}}{\mathrm{d}t\,\mathrm{d}\epsilon} \propto \epsilon^{-(p+1)/2}. \tag{2.5}$$

$$\frac{\mathrm{d}N_{\gamma,\mathrm{KN}}}{\mathrm{d}t\,\mathrm{d}\epsilon} \propto \epsilon^{-(p+1)}. \tag{2.6}$$

In the astrophysical context, photon fields are very common, mainly because of the ubiquitous isotropic Cosmic Microwave Background (CMB) radiation. Therefore, the interaction of an accelerated particle with radiation fields is unavoidable. At typical source sites, the IR, optical, and UV radiation fields can be very intense. As a counterpart to support the IC model of an astrophysical source, the same underlying electron parent particle spectrum could also emit lower energy photons, as X-rays; thus, the combined analysis of both energy ranges could be due to the same underlying electron parent particle distribution. One remarkable example of this is the modeling of the Crab spectrum, which can be well-described by one leptonic scenario in an agreement between the different wavelength measurements. The higher tail of the spectrum is described by IC emission.

It is important to mention that in IC the particle transferring energy to a photon is not exclusively an electron; however a proton, due to the higher mass, exchanges much less energy than the electrons, being of order $(m_e/m_p)^4 \sim 10^{-13}$ lower and negligible for the gamma-ray spectrum. Thus, IC is strongly related to leptonic scenarios.

2.2.2 Process: Synchrotron

Synchrotron - Short Description

An electron spiraling along magnetic field lines emits electromagnetic radiation. The emission depends on the pitch angle, α, however, an isotropic distribution is commonly assumed for α angles. The emitted radiation is a continuum distribution with a sharp peak at a critical frequency, ν_c, which depends on the electron energy and the strength

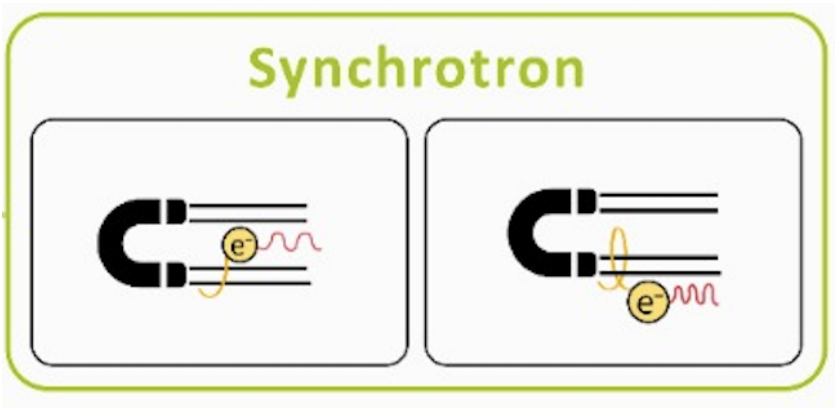

Figure 2.5: Overview of synchrotron mechanism. Courtesy of Ayumi Nakashima.

of the magnetic field. When considering a distribution of parent particles, all individual contributions usually result in a smooth radio-to-X-ray emission. In case of extreme events, for instance, gamma-ray bursts, gamma-rays can be produced via synchrotron. This interaction can be described similarly to IC in the Thomson regime, assuming an electron interacting with a virtual photon from the electromagnetic field. An illustration of the process is shown in figure 2.5.

The energy loss equation for this mechanism is described as the following equation:

$$\left(-\frac{\mathrm{d}E_e}{\mathrm{d}t}\right)_{\mathrm{SYN}} = \frac{4}{3}\sigma_T c \left(\frac{E}{m_e c^2}\right)^2 \frac{B^2}{2\mu_0}. \tag{2.7}$$

This equation has similarities to the equation 2.1 from IC for Thomson regime: the parameters σ_T, c, $m_e c^2$, E (for electron's energy) are the same, and the radiation field parameters are replaced by the strength of the magnetic field, B and the vacuum permeability constant, μ_0. Especially because the dependency of the energy loss equation with the electron's energy is the same in the IC Thomson regime and for synchrotron, the cooling time equations are also very similar, in which the features of the radiation field are again replaced by the magnetic field B, as described in [17]:

$$\tau_{\mathrm{syn}} = 2.5 \cdot 10^9 \left(\frac{1}{\mu_0}\frac{B}{\mathrm{G}}\right)^{-2} \left(\frac{E_e}{\mathrm{GeV}}\right)^{-1} \mathrm{yr}. \tag{2.8}$$

For an electron distribution following a power-law spectrum with index p, the emitted electromagnetic radiation, in function of the photon frequency ν, has the shape:

$$J(\nu) \propto B^{(p+1)/2} \nu^{-(p-1)/2}. \tag{2.9}$$

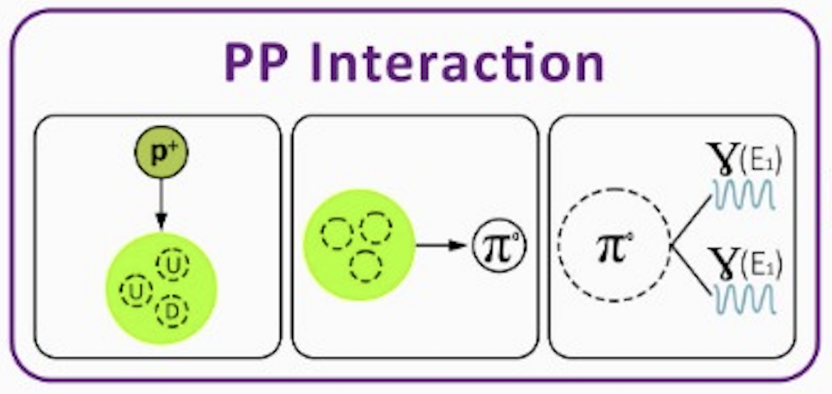

Figure 2.6: Overview of p-p mechanism. Courtesy of: Ayumi Nakashima.

Figure 2.2 shows as a green line an illustration of the shape expected electromagnetic spectrum due to the synchrotron mechanism. The shape of the spectrum is similar to the IC but shifted to lower energies.

In the astrophysical context, magnetic fields are very common, for instance, produced by pulsars. The X-ray and radio emission produced via the synchrotron mechanism requires a high-energy electron population, that when in a photon field can also emit gamma rays through the IC mechanism. Thus, often the X-ray and gamma-ray bands of a pulsar are derived from the same underlying model, considering a unique electron population [4]. Additionally, due to the synchrotron mechanism, an estimation of the strength of the magnetic field can be derived.

2.2.3 Process: p-p Interaction

p-p Interaction - Short Description

Inelastic scattering of a relativistic proton with a low energy proton/neutron in a matter field. During the interaction, due to the strong force, mesons are created[a] – mainly pions due to the light mass. The three flavors of pions are created with the same probability, however, only neural pions are relevant for this process. The neutral pion decays into 2γ with a branching ratio of $\sim 98\%$ [18]. The emitted gamma-ray spectrum has a distinct shape, known as pion bump, with a cutoff in low and high energies. The low energy cutoff, at 67.5 MeV, is derived from the pion mass and it is independent of the environmental conditions, and therefore this process shines only in the gamma-ray energy range. The high energy cutoff is a consequence of the maximum energy of the proton energy. An illustration

of the process is shown in figure 2.6.

[a] a Feynman diagram for it is shown in figure 2.7

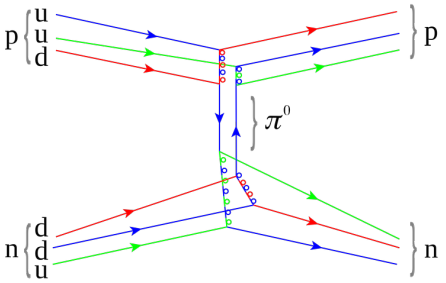

Figure 2.7: Feynman diagram for proton and neutron interaction involving a neutral pion.

In contrast to the previous mechanisms, in which only electromagnetic force is involved, in the p-p interaction, the strong force is also involved. The interaction between the two hadrons occurs via the strong force and the subsequent decay of the neutral pion occurs due to the electromagnetic force[†] and the Feynman diagram for it is shown in the figure 2.8.

The interaction between the two hadrons is more probable to result in fewer created particles (one or two) with high energy than several particles with low energy [13]. As a consequence, the newly created pions carry a considerable amount of energy from the primary proton, and its decay results in the production of high-energy photons.

Due to energy conservation, to produce a neutral pion, the proton must have an energy higher than the threshold, $E_{\text{th}} = 2m_{\pi^0}c^2(1 + m_{\pi^0}/4m_p) \sim 280\,\text{MeV}$, in which m_{π^0} and m_p are the neutral pion and proton masses. Yet, due to energy conservation the emitted photon also has a low energy threshold defined as $E_\gamma = m_{\pi^0}c^2/2 = 67.5$ MeV (in the pion rest frame). This constraint, which is independent of the environmental conditions, is responsible for the low energy cutoff in the final gamma-ray spectrum.

The gamma-ray emission is dependent on m_{π^0}, m_p, the proton cross-section, $\sigma_{\text{pp}}(E_p)$ (derived from collider experiments), the fraction of transferred kinetic energy from the proton to the created pion, κ_π, and the density of the matter field, n_0. A good approximation done by [13] for the cooling time is:

$$\tau_{\text{pp}} \sim 5.3 \cdot 10^7 \left(\frac{n_0}{\text{cm}^3}\right)^{-1} \text{yr}. \tag{2.10}$$

The cooling time is independent of the energy of the proton; consequently, the shape of the radiated gamma-ray spectrum

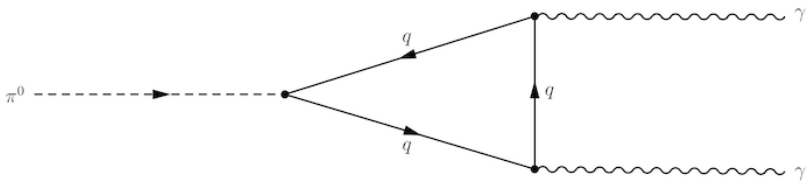

Figure 2.8: Feynman diagram for π^0 decay into two photons

[†] Unlike the charged pions, which decay due to the weak force, the neutral pion decay is due to the electromagnetic force. In classical electrodynamics, this decay is forbidden because it does not conserve partially conserved axial current (PCAC). However, Adler and Bell-Jackiw demonstrated that when considering chiral anomaly in quantum mechanics this decay is allowed [19, 20].

Figure 2.9: Overview of hadronic mechanism. Courtesy of: Ayumi Nakashima.

mirrors the spectrum shape of parent particles[‡].

Thus the final emitted radiation spectrum has a low energy boundary at 67.5 MeV, due to the m_{π^0}, and rises steeply up to 400 MeV; at high energy, the boundary is defined by the cutoff of the parent particle spectrum [21, 17]. Figure 2.2 shows as a purple line an illustration of the expected spectrum shape for this configuration.

Because this process is the only one with a cutoff at low energy that is independent of the environment, this feature is a strong advocate in favor or against hadronic scenarios [22, 23]. Additionally to the shape of the gamma-ray spectrum, the hadronic model is strongly supported by neutrino measurements, since it is the only process that could also result in neutrinos. Thus, the spatial and time coincidence detection of gamma rays and neutrinos strongly favors the hadronic scenario.

In the astrophysical context, the matter fields are common in star-forming regions, Nebulas, and molecular clouds as in the GC. It is worth noting that this mechanism only produces gamma rays at the matter field's location. For instance, the proton acceleration site can be at a spatially different site from a molecular cloud, and the parent particles can diffuse and occasionally reach the matter field.

In addition to gamma-ray production, the p-p interaction is also relevant to gamma-ray detection. The cosmic proton when interacting with the Earth's atmosphere due to p-p interaction produces a signal similar to the one produced by gamma rays, and it accounts for the overwhelming background in ground-based gamma-ray observations.

2.2.4 Process: Bremsstrahlung

Bremsstrahlung - Short Description
The emitted radiation when an electron is bent by a

[‡] It is only valid under the assumption that the density profile, n_0 is independent of energy.

coulomb field of another charged particle. The radiation emitted depends especially on the species composing the matter field, since it influences the strength of the Coulomb field. Examples of matter fields are electron gas, the Earth's atmosphere, or ionized gas. This process produces radiation as high as gamma rays and X-rays and also in the non-relativistic regime of the parent particle. An illustration of the process is shown in figure 2.9.

The energy loss equation for Bremsstrahlung for the relativistic electrons is:

$$\left(-\frac{\mathrm{d}E_e}{\mathrm{d}t}\right)_{\text{brem, rel}} \propto Z^2 N E \ln\left(\frac{192}{Z^{1/3}}\right), \tag{2.11}$$

which depends on the electron 's energy E, atomic number of the matter field, Z, and number density of nuclei in the laboratory frame, N. The linear dependency of the energy loss equation with energy results in a time-independent cooling time, which is defined as:

$$\tau_{\text{Br}} = 4 \cdot 10^7 \left(\frac{N}{\text{cm}^{-3}}\right)^{-1} \text{yr}. \tag{2.12}$$

Due to dependency only on the environmental features, this cooling process does not influence the parent particle spectrum, and therefore the radiation spectrum mirrors the shape of the initial parent spectrum. Figure 2.2 shows the yellow line as an illustration of the expected radiation shape from the Bremsstrahlung process. This mechanism has no constraint on the electron energy, thus it shines in a broad range of wavelengths, including gamma rays.

The field of interaction for Bremsstrahlung in an astrophysical context is very hot plasmas, $T \sim 10^6$ K, in which N is obtained from radio, microwave, and optical measurements. However, N is usually not high enough to be the dominant cooling mechanism producing gamma rays. For instance, in an environment such as the Galactic Center, with a matter density of $n = 1000/\text{cm}^3$, the cooling time is expected to be 1000 years.

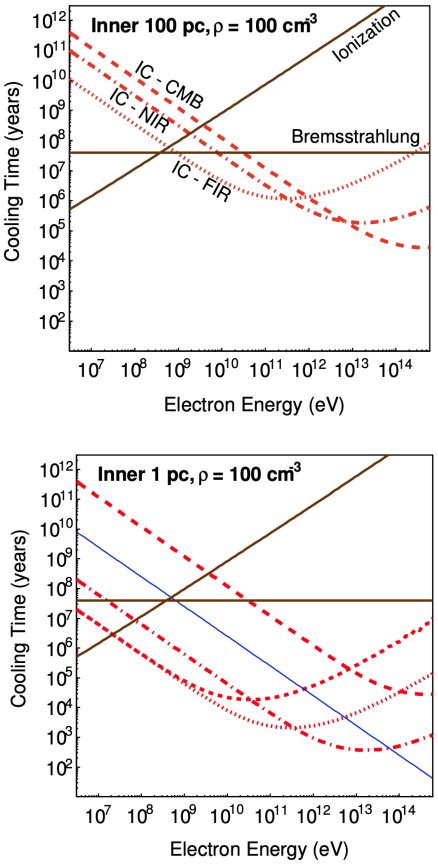

Figure 2.10: Cooling time for the different cooling mechanisms in the leptonic scenario. The upper plot considers environmental conditions as the inner 100 pc and the bottom plot, 1 pc of the Galaxy. Different matter density is assumed for the different regions. Image is taken from [17], in which further details about the plot can be found.

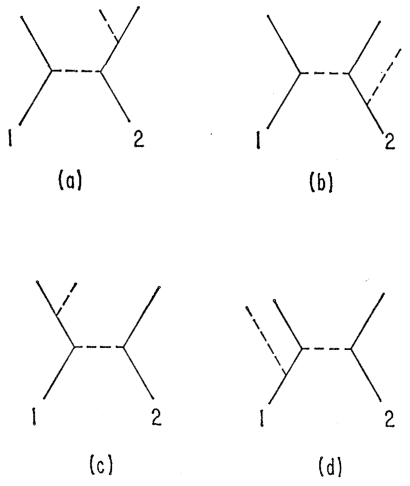

Figure 2.11: Feynman diagram for Bremmstrahlung and pair-production, taken from [14]

2.2.5 Summary and Comparison of Different Physical Processes

The physical models behind the gamma-ray emission are often classified according to the nature of the parent particle, leptonic or hadronic. Figure 2.12 shows in energy scale the gamma-ray emission due to different cooling mechanisms given an injection of accelerated protons, in the upper plot, and accelerated electrons, in the lower plot.

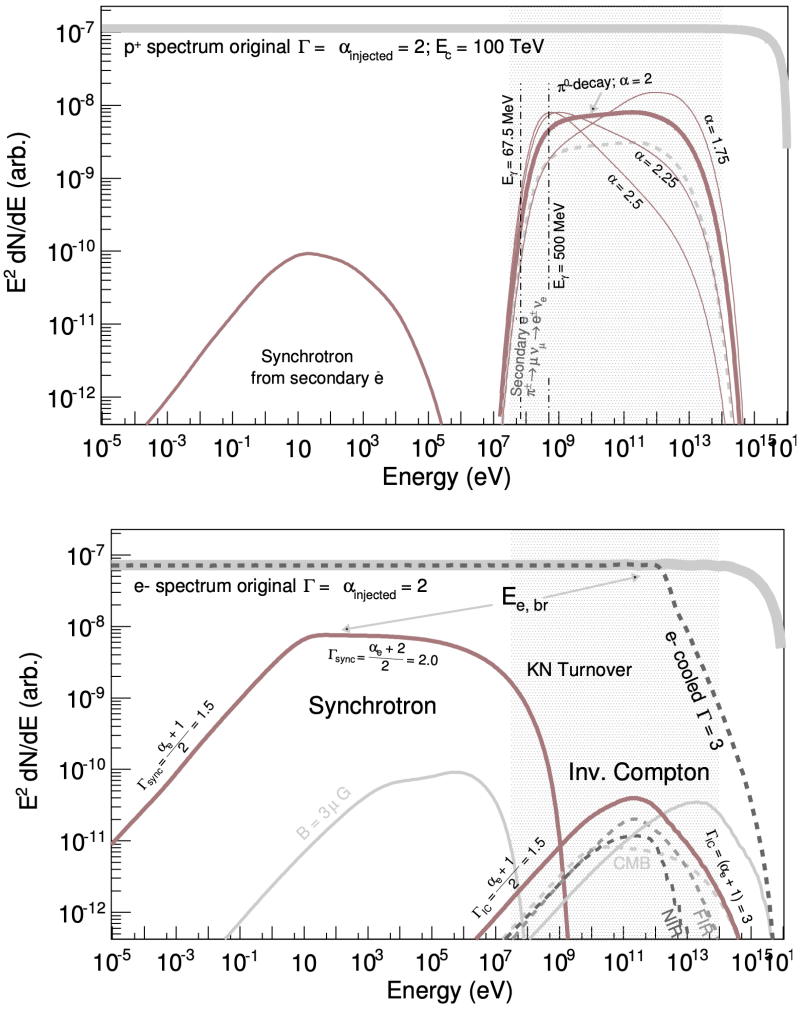

Figure 2.12: Gamma-ray emission due to different physical processes for the given parent particle spectrum scenario. The proton spectrum follows an exponential cutoff power law, with index $\alpha = 2$ and cutoff energy at 100 TeV. For the synchrotron emission of the upper plot, a magnetic field of $B = 30\mu$G and a source age of 1000 years is assumed. The electron spectrum for the bottom plot has a power-law injection with $\alpha = 2$, with environmental conditions as the inner 100 pc of the Galaxy, considering a source age of 1000 years. The images are taken from [17].

In the hadronic scenario from figure 2.12, two different emissions are observed, at high energy due to p-p interaction and at low energies due to synchrotron emission. The high energy emission, the pion bump, shows its characteristic cutoff in low energies at ~ 67.5 MeV, and a cutoff in high energies. The p-p process has among its subproducts electrons, which also radiate, at lower energies, due to the synchrotron mechanism.

In the leptonic scenario from figure 2.12, the emission at high energies is due to IC mechanism, which considers the contribution of different radiation fields, CMB, NIR, and FIR. At low energies the synchrotron mechanism is dominant. It highlights again the efficiency of IC mechanism for cooling the highest energy electron, producing higher energy radiation, and the synchrotron process being efficient in the lower range.

The correlation between the radiation in different energy

ranges, due to different cooling mechanisms but with the same injection of accelerated particles is often used in analysis to provide a whole picture of the source and its environment.

The comparison of the cooling time from different mechanisms considering a leptonic scenario is shown in figure 2.10, considering ambient conditions as the inner 100 pc (upper plot) and inner 1 pc (bottom plot) region of the Galactic Centre. The additional blue line in the bottom plot shows the cooling time for synchrotron emission. The cooling time is relevant to indicate the efficiency of the cooling mechanism. It is observed that except for the Bremsstrahlung mechanism, all processes have an energy-dependent cooling time. The IC has a turnover point which is due to the suppression of KN regime. Nevertheless, IC is the most efficient process for TeV electrons. In the inner 1 pc, the cooling time for TeV electrons is as short as 100 years for NIR radiation field.

Finally, it is worth noting that each production mechanism also has a counterpart absorption mechanism, due to the symmetry of the Feynman diagram. For instance, the rotated Feynman diagram from Bremsstrahlung emission in an electron field ($e^- + \gamma \rightarrow e^- + \gamma$) provides the diagram for pair-production ($\gamma + \gamma \rightarrow e^+e^-$), as shown in figure 2.11. At an astrophysical source, the radiation produced can also be absorbed and re-emitted. The measured radiation is the net radiation, which escaped the interaction radius of the astrophysical source and can travel freely into space.

2.3 Instruments for Gamma-Ray Detection

Gamma rays cover a broad range in the energy spectrum and to enclose this range different detection techniques are required. Figure 2.13 presents an illustration of three different detection techniques in function of energy and altitude. The Earth's atmosphere is opaque to gamma rays; therefore, they are either directly measured in space, using satellites or indirectly measured on the ground.

The abundance of gamma rays decreases with energy. Since gamma rays become rarer as the energy increases, larger collection areas are required to increase the chances of detection. However, due to practical limitations, such as being costly, instruments have a limited collection area. The size of the collection area of each instrument dictates its threshold at high energy. As a consequence, when one technique or instrument reaches its limits, another technique with a bigger collection area can cover the following part of the energy spectrum. Thus, the lack of statistics in high energies, caused by the limited collection area, is the main reason for the necessity of different detection techniques at different energy ranges [17].

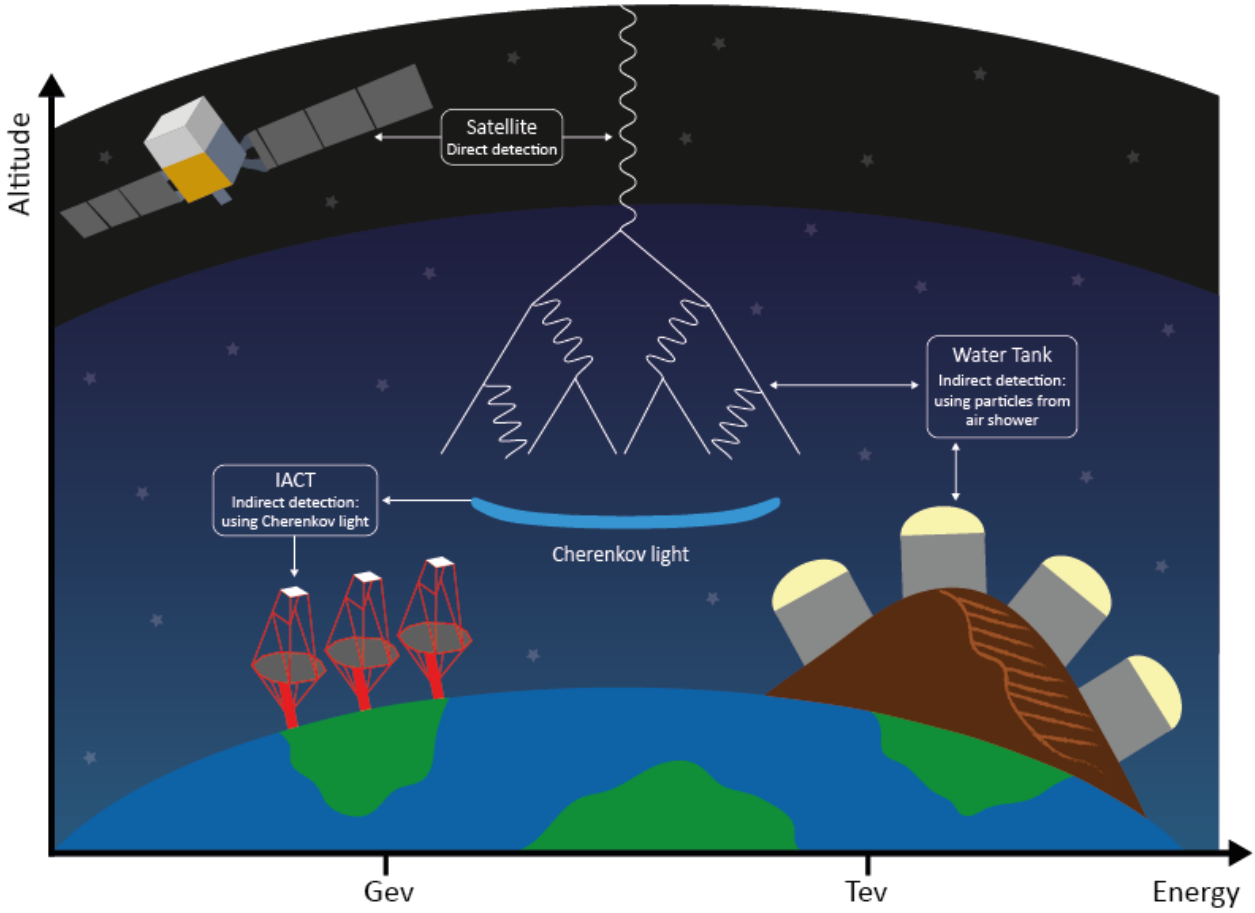

Figure 2.13: Illustration of different instruments for gamma-ray detection as a function of energy. Courtesy of Ayumi Nakashima.

Gamma rays can only be directly measured by satellites. They are survey experiments, scanning the entire sky with a duty cycle of ~ 99%. This technique allows the detection of photons in the energy range of ~ 100 MeV up to ~ 500 GeV. Among the current operational gamma-ray satellite, there is the *Fermi*-LAT, launched by NASA in 2008 [3].

The Imaging Atmospheric Cherenkov Telescopes (IACTs) are the most suitable instruments for the range of ~ 300 GeV up to ~ 100 TeV. When entering the atmosphere, the gamma-ray dissipates its energy by creating an air-shower[§]. The Cherenkov light is one of the final products of this interaction [24], and it can be detected by IACTs [25]. The Cherenkov radiation peaks at the range of the UV light; thus, its detection can only be performed during dark nights [26]. This restriction drastically decreases the duty cycle of IACTs compared to survey experiments. The IACT is a pointing instrument with the most accurate space resolution, at its best performance, among the gamma-ray instruments, allowing detailed morphology analysis of the observed source. Currently, the three major IACTs observatories are H.E.S.S. in Namibia [27], VERITAS in the USA [28], and MAGIC in

[§] More details of air-shower will be given in section 2.3.2

the Canary Islands [29].

The highest part of the electromagnetic spectrum, from ~ 1 TeV, is covered by water tank instruments. Similarly to the IACTs, the water tank instruments also detect air showers; however, instead of the Cherenkov radiation created in the atmosphere, this technique detects the Cherenkov light produced by the particles within the water tanks. Hence, the water tank observatories must be located at high altitudes, closer to the air shower core. This detection is independent of the ambient light, and therefore, they have almost 100% of duty cycle, being also a survey experiment. Examples of current water tank observatories are HAWC [30] and LHAASO [5].

From now on, the focus will be on the observatories *Fermi*-LAT and the H.E.S.S..

2.3.1 The *Fermi* Large Area Telescope

Figure 2.14: *Fermi* Gamma-Ray Space Telescope. Credit: NASA / Aurore Simonnet, Sonoma State University. Photo-illustration: Sandbox Studio

The Large Area Telescope (LAT) [3] is an imaging gamma-ray detector on board the *Fermi* Gamma-Ray Space Telescope spacecraft. It was launched on June 11th, 2008 by NASA. It has an orbit of 535 km above sea level, completing one full turn around the Earth every 96 minutes. The FoV of 2.4 sr enables *Fermi* to scan the whole sky in approximately three hours. With a collection area of 1 m^2, the telescope detects gamma rays from ~ 20 MeV to more than 300 GeV.

Detection Technique and Instrument Description

The detection of a gamma ray in LAT occurs via pair production. The photon, when traveling through matter, interacts with the Coulomb field of the atoms, which triggers the conversion into e^+e^- pair. These pairs leave an ionized path in the semiconductor layers of the tracker. This path is used to reconstruct the incoming direction of the photon.

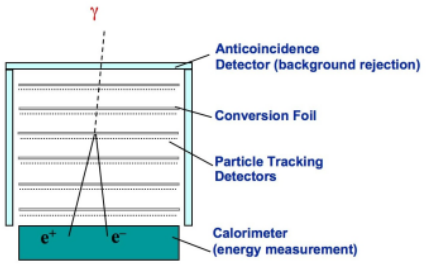

Figure 2.15: Illustration of LAT parts and detection technique. Image taken from the website

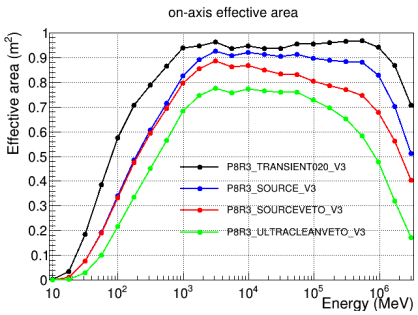

Figure 2.16: LAT's effective area. Image taken from the website

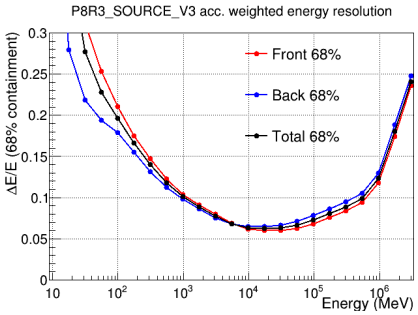

Figure 2.17: LAT's energy dispersion. Image taken from the website

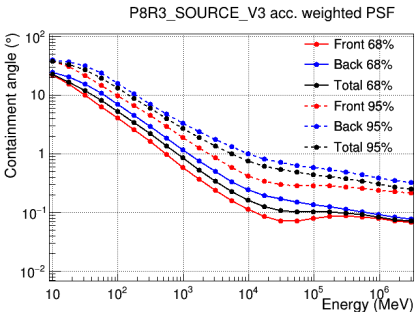

Figure 2.18: LAT's PSF. Image taken from the website

To achieve this, the instrument needs (I) conversion foils, that stimulate the pair production, (II) a particle tracker, for tracing the trajectory of the particles, (III) a calorimeter for measuring the energy, and (IV) an anti-coincidence shield, that avoid CR background contamination [3]. The schematic principle of detection can be better visualized from the figure 2.15 and a detailed description of each part is given in the following.

(I) The conversion foils offer suitable conditions for photon-matter interaction to occur. The higher the atomic number of the foil material the higher the probability of the pair conversion. The thickness of the foils must be such that it is thick enough for the conversion to happen. The LAT's configuration is 16 foils made of Tungsten (atomic number $Z = 74$), which is optimized for LAT's energy range.

(II) The particle tracker is composed of stripes located between the foils and it detects the position of the electron-positron pair. Thus, whenever an electron-positron pair is created in the foils, the tracker detects them. For LAT, there are 18 layers of trackers made of silicon. By tracing back the trajectory of the charged particles, the incoming direction of the photon is reconstructed.

(III) For LAT, the calorimeter is composed of 8 layers made of Cesium Iodide stacked, located in the bottom part of the experiment.

(IV) The anti-coincidence shield distinguishes cosmic and gamma rays based on the electrical charge. When a charged particle hits the shield, a flash is produced, while the photon passes through the shield unnoticed. With this method, LAT rejects 99.97% of CR.

The components described in (I), (II) and (III) are stacked in a shape of a tower, and LAT is composed of an array of 4x4 of these towers. The whole instrument is surrounded by the anti-coincident shield and by a blanket, providing thermal insulation and protection from micrometeoroids. The final size of LAT is 0.72 m deep and 1.8 m^2, with a mass of 2789 kg, and consumes 650 W of electric power. The satellite is pointing in the opposite direction from Earth, thus our planet does not shade in the view nor contribute as background.

The LAT's Instrument Response Function (IRF) is parameterized as energy resolution, effective area, and Point Spread Function (PSF), shown in figures 2.16, 2.17 and 2.18. The most recent version of the IRFs is the Pass 8 Release 3 version 3. [31]

The background in LAT analysis is mainly due to gamma rays from other sources, the diffuse emission of the Galactic Plane, and the isotropic gamma-ray emission. The LAT collaboration provides templates for diffuse and isotropic background emission. Additionally, there are LAT catalogs, the newest catalog [32] is based on 12 years of observation. The provided

template maps and the 4FGL are used in the analysis of this work.

Analysis Technique

The data collected by LAT is a list of detected photons. Each of them is characterized by four main parameters: two spatial coordinates, energy, and time. The quality of the data, which is given by the reliability of reconstructing the photon parameters, is classified in LAT by the so-called 'event classes'.

Each event class relies on a specific set of IRFs to derive the gamma-ray characteristics. However, the higher the required photon quality, the lower the amount of available data. Hence, the quality of the analysis is enhanced by the cost of lowering statistics. The event class is useful for different analysis goals. Within each event class, the quality of the events can be classified by their so-called 'event type'. Each event type prioritizes one specific IRF to reconstruct the event, to achieve better quality for a specific characteristic. The different event types are based on: PSF - improving the direction of the photon, Energy Dispersion - improving the energy of the photon, and which section of the tracker (front or back) the event is reconstructed - improving the angular resolution.

The final selected data is a list of photons from a certain event class and event type. The analysis method follows the maximum likelihood method. This scheme follows a bayesian approach, which considers an a priori model and a given statistical distribution, Poisson for this case. Based on the model, the probability of the data to match input model is calculated. The maximum probability is reached by a certain set of parameter values of the input model, known as best fit values.

The drawback is that it must be assumed a model beforehand, and it is highly bounded to it, thus any features in the data might be hidden or wrongly described by the incorrect assumption of the input model.

For the input model besides the source of interest and the sources in the FoV, one must also consider the gamma-ray diffuse emission and isotropic emission. To increase the statistics and to be computationally efficient, binning analysis in space, energy, and time is adopted. Thus, the analysis is performed by fitting the binned cube. For each bin i, there is the detected number of gamma-ray events, n_i, and the expected signal for this bin, m_i, which is defined from the convolution of the input source model with the instrument capabilities (IRFs). The probability, p_i, of getting the detected signal, n_i, expecting a signal, m_i, is calculated for each bin and the combination of all of them gives the total probability of the assumed model, m, to match the observed data, n. Finally,

the best-fit parameters of the model are found by maximizing the likelihood $\mathcal{L}$, described in the equation 2.13.

$$\mathcal{L} = \prod_i p_i = \prod_i \frac{m_i^{n_i} e^{-m_i}}{n_i!} \tag{2.13}$$

This method allows the analysis of multiple spatially overlapping models in the same FoV.

2.3.2 The H.E.S.S. Experiment

The High Energy Spectroscopy System (H.E.S.S.) [27] is a ground-based gamma-ray observatory located in the Khomas highlands in Namibia, near the Gaumsberg mountain, at 1800 meters above sea level. It observes photons from 30 GeV up to 100 TeV. It officially started its operations in 2004, initially with 4 IACTs, and in 2012 one more IACT was included to observe lower energy photons. It is currently the only IACT observatory located in the Southern Hemisphere, which allows a privileged view of the GC region.

Figure 2.19: Picture of the H.E.S.S. observatory. Credit Vikas Chander

Detection Technique of IACT Observatories

The detection technique of an IACT consists in using the atmosphere as a calorimeter to dissipate the energy of the incoming gamma ray. The gamma ray interacts with the atmosphere and an electron-positron pair is created. Each newly created particle undergoes Compton scattering producing new photons. The new photons, when energetic enough, produces a new electron-positron pair. In each step of this cycle—in which new particles are being created—the energy of the parent particle is divided. Thus, it results in a cascade of particles with low energies. The cascade stops growing when the particles lack enough energy to create new particles. Subsequently, the energy loss happens depending on the

energy of the particle, through Bremsstrahlung (≥ 84 MeV) and ionization (≤ 84 MeV) processes.

The interaction of charged particles with the medium results in Cherenkov radiation when their speed is higher than the speed of light in the medium. Thereby, the high energy particles in the cascade traveling through the atmosphere emit Cherenkov radiation and it occurs at an altitude of ∼ 10 km above sea level [13]. The cascade of particles and the radiation emitted is named air shower.

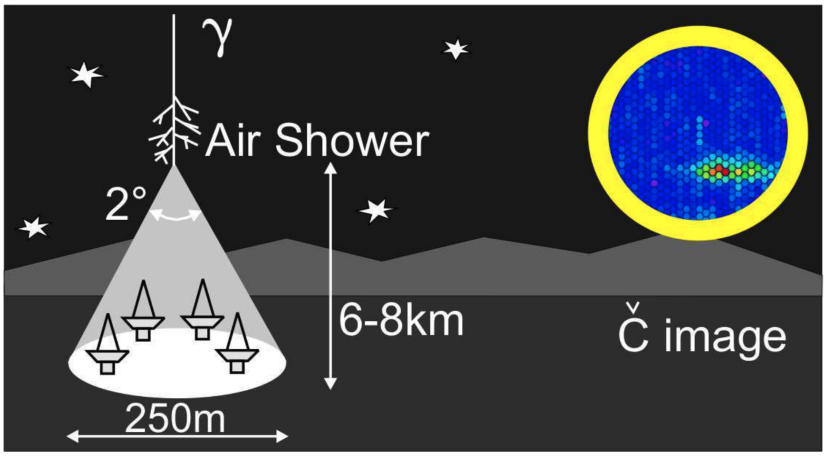

Figure 2.20: Illustration of the air shower and the light pool created by it reaching the ground. Also on the top right is shown how the camera in on telescope observes the Cherenkov light signal. The image is taken from [13].

The sum of all Cherenkov radiation in the air shower forms a light pool traveling toward the ground. On the ground, the IACTs detect it as a faint flash of ∼ 10 ns in an area of radius of ∼ 100 m, with a wavelength between 300-350 nm. For instance, a gamma ray of 1 TeV produces a light pool of about 100 photons/m^2 at the ground level.

To detect this faint flash, the IACT must have a collection area and a fast camera system. The large collection area is achieved by a large dish, covered by mirrors that reflect all the collected photons onto an array of photomultiplier tubes (PMTs), the front part of the IACT camera. Figure 2.20 shows a cartoonist overview of the process including on the top right the resulting view on the camera.

The signal detected by the cameras is an image of an elongated ellipse, with the major axis corresponding to the major axis of the air shower development. From the ellipse properties, namely Hillas parameters [33], the primary photon's physical information is derived from Monte Carlo (MC) simulations.

The detection's accuracy is improved by increasing the number of telescopes detecting the same air shower; this technique is known as the stereoscopic technique. The optimal distance between the telescopes in the stereoscopic technique depends on the size of the light pool on the ground.

CRs are of the order of 1000 times more abundant than gamma rays and they also create air showers when enter-

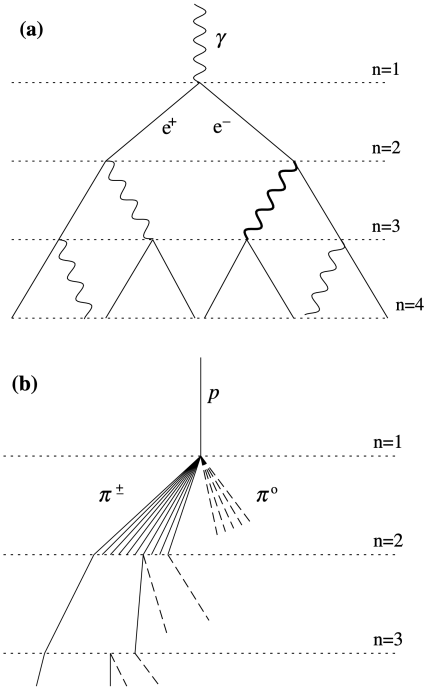

Figure 2.21: Air shower sketch for (a) electronic and (b) hadronic. The image is taken from [34]

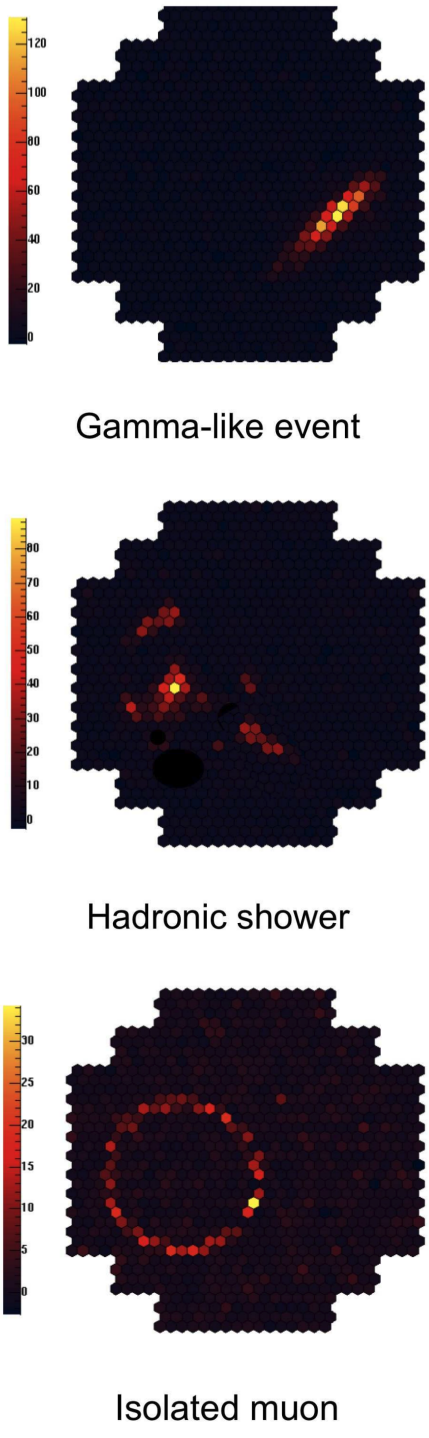

Figure 2.22: The different patterns observed on the camera are due to different particles. The image is taken from [37]

ing the atmosphere. The air shower initiated by a hadron, namely hadronic air shower, is composed of photons, electrons, hadrons, and muons. On the other hand, the air shower initiated by a photon or an electron, an electronic air shower, is composed of photons and electrons only.

The particles in an air shower, as shown in figure 2.21, define the air shower shape. As a consequence, electronic and hadronic showers are distinguishable on the camera by the different footprint patterns observed. While the electronic air shower presents an ellipse shape, the hadronic air shower presents a non-uniform, scattered signal. Additionally, muons also leave a very characteristic ring on the camera, which is further used as calibration of the instrument [35, 36]. Figure 2.22 presents the different patterns observed by the cameras in an IACT.

This distinct footprint on the camera is used to suppress the overwhelming CR background, reducing the ratio of CR to gamma-ray from 1000:1 to 1:1 for the example source Crab Nebula [13]. The remaining background, namely photon-like events, must be accounted for in an analysis.

The atmosphere column in which a particle travels through to reach the telescope change with a zenith angle. For instance, particles coming with a low zenith angle travel a shorter path than particles coming from a high zenith angle distance. The longer the path, the more the Cherenkov photons are absorbed by the atmosphere, and fewer photons are available for detection. Thereupon, the effective area and the threshold at low energy present a dependency on zenith angles. Figure 2.23 presents the increase in the energy threshold with zenith angle for H.E.S.S. for different data selection cuts.

External conditions strongly impact the detection of an event and consequently, the physical parameters extracted. Some relevant parameters are the Night Sky Background (NSB), the atmospheric conditions, and the instrument aging. The NSB indicates the level of luminous pollution present and the higher the NSB the fewer low-energy gamma rays can be detected. The atmospheric conditions include the presence of clouds or aerosols that scatter more Cherenkov photons, leading to fewer Cherenkov photons arriving in the cameras [38]. The aging of the instrument includes, among others, dust on the mirrors decreasing its reflection power resulting also in fewer Cherenkov photons detected by the camera. All these effects are evaluated and included in the Monte Carlo (MC) estimation of the acceptance/IRF of the instrument.

The current generation is in duty for ~ 15 years and led to tremendous scientific advancement, and the next generation is currently under construction, the CTA (Cherenkov Telescope Array) [39].

Description of the Instrument

The H.E.S.S. telescope array is composed of four identical IACTs with a dish diameter of 12 m, namely CT1, CT2, CT3, and CT4, placed at the corners of a square of size 120 m, which is optimally chosen for detection of photons of energies 1 TeV. At the center of the square, CT5, with a dish diameter of 28 m, was added in 2010. The bigger dish size allows a larger collection of light, enabling the detection of lower-energy gamma rays.

The telescopes have a Davies-Cotton layout with alt-azimuth mounting. For CT1-4/CT5, the camera is composed of 960/2048 photo-multiplier tubes (PMTs), equipped with Winston cones to enhance the light collection. Each tube corresponds to a pixel size of 0.16/0.067 ° in diameter, arranged in a hexagonal shape, resulting in an FoV of 5/3.2 ° on the sky. The PMTs period to sample the signal is of the order of 1 ns, which is optimized for the short duration of the Cherenkov flash.

The H.E.S.S. telescopes are spread such that it covers a total collection area of 107 m^2 [40, 41] and its pointing precision of RMS error 2.5”, is capable to distinguish sources within arcsec scales [42].

The timeline of H.E.S.S. is divided into so-called eras, corresponding to different phases of the experiment. The H.E.S.S. I era refers to the period in which only CT1-4 was in operation, from 2003-2012. The H.E.S.S. II era covers the period with the addition of CT5, from 2012-2015. Finally, the current era is H.E.S.S. 1U, which started in 2015, due to CT1-4 cameras update to improve performance and reduce dead time related to aging.

The effective Area is a combination of the detection efficiency of the instrument with the observable area. Its limitation occurs due to the absorption of the Cherenkov photons by the atmosphere when the air shower is away from the array center. The high-energy events produce more Cherenkov light and consequently can be detected at larger distances than events of low energies. Thus, the Effective Area curve increases as the energy increases and it has a low energy cutoff.

Additionally, the Effective Area is strongly dependent on the zenith angle. The higher the zenith angle, the larger the atmospheric column the photon must travel to reach the telescope. Due to the larger travel path, fewer Cherenkov photons reach the detectors caused by the absorption in the atmosphere. Thus, the detection of low energy gamma rays at high zenith angles is limited due to a larger layer of the calorimeter (atmosphere) of the instrument. As a consequence, the Effective Area curve presents different cut-off energies at low energies for different zenith angles, as exemplified in figure 2.24.

The energy bias is the relationship between the photon’s true energy and the energy of the reconstructed event. The

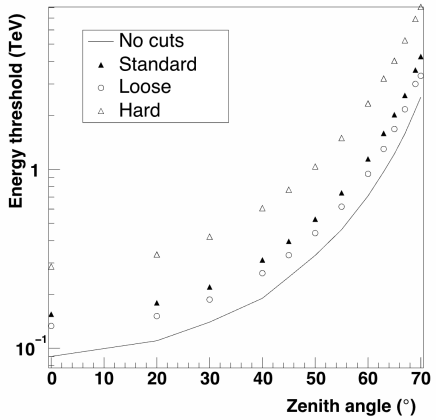

Figure 2.23: Low energy thresholds in the function of zenith. The different curve lines present different cuts of gamma/hadron separation. Figure is taken from [27]

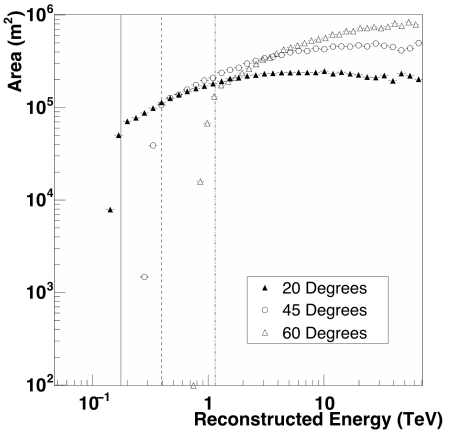

Figure 2.24: The Effective Area for H.E.S.S. for different zenith angles. Image taken from [27]

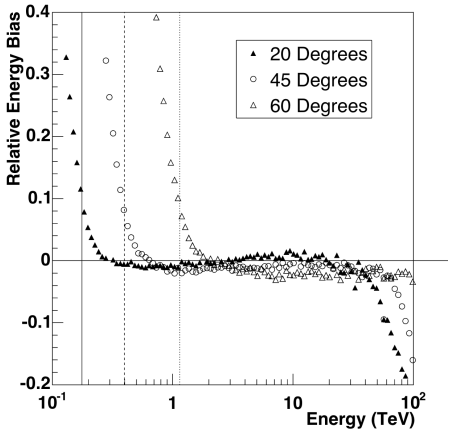

Figure 2.25: H.E.S.S. energy dispersion. Image taken from [27]

reconstructed energy of the event presents deviation from the true value especially at the lowest and highest energies, due to higher systematic errors. At low energies, it happens since the reconstruction of an event is more challenging with fewer detected Cherenkov photons. At the highest energies, the bias occurs because the events produce very long ellipses that might not be fully contained within the cameras, therefore biasing the reconstruction procedure. Figure 2.25 exemplifies the energy dispersion for different zenith angles.

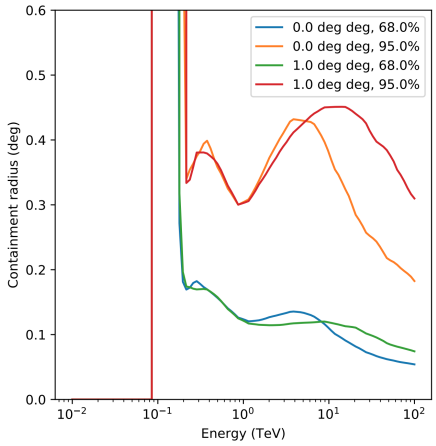

Figure 2.26: H.E.S.S. Point Spread Function example. Image taken from [43]

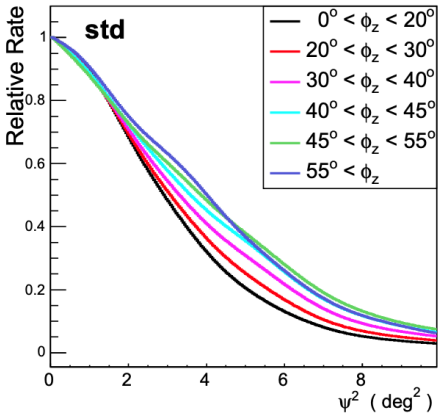

Figure 2.27: H.E.S.S. radially acceptance for different zenith bins. Taken from [44]

The PSF, shown in figure 2.26, refers to the instrument's capability to indicate the correct direction of the incoming event. It is crucial for characterizing the morphology of the gamma-ray source. The PSF is characterized by a gaussian distribution indicating the spatial probability of the event direction; thus, the PSF is often indicated at the sigma levels of the gaussian containment. Additionally, the PSF also varies along the camera FoV, being more accurate at the center.

H.E.S.S. operates with observation runs of 28 minutes. During a run, a fixed RA/DEC position in the sky is observed, in which the pointing direction is guided using the bright stars present in the FoV. An event is measured when at least two telescopes trigger by the presence of an air shower. The measured Hillas parameters, with individual run parameters, such as atmosphere quality, NSB, zenith direction, etc, are used to reconstruct the characteristics of the incoming photon.

H.E.S.S. uses different methods to calibrate the instrument. One relevant calibration parameter for this present work, namely muoneff, is based on the Cherenkov light in a ring shape produced by muons when interacting in the atmosphere as shown in figure 2.22. There is a well-known correlation of the light intensity of the muon ring with its radius. Thus, by measuring the radius of the ring, it is known the expected amount of light for this signal.

However, the light detected by the instrument is not necessarily the total amount of light produced in the muon interaction, due to external atmospheric and instrument conditions. Thus the ratio of the expected and measured light of the muon ring signal provides information about the detection conditions [36]. This parameter is measured for each run and for each telescope. As a first order approximation, the average value in each run of the muoneff for the telescopes is considered. In the next chapter, the effects of this parameter in one analysis are presented.

H.E.S.S. conducted and finalized in 2018 a Galactic Plane survey, constructing the very high energy gamma-rays source catalog, HGPS [45]. The H.E.S.S. data is currently also available in the convention of FITS format [43]. This format allows the data to be used in open-source tools for analysis, such as gammapy [46], demonstrating the development and maturity of the field.

Analysis Technique

The analysis in H.E.S.S. consists of deriving the physical properties of astrophysical information from the measured ellipse parameters from an air shower. The analysis chain can be separated into low and high-level analyses. The low-level analysis covers the reconstruction of the physical properties of the event and the classification of an event as CR background or gamma ray. The output of the low-level analysis provides a list of measured events and their physical properties. The high-level analysis consists of deriving physical properties of astrophysical sources from this event list.

The physical properties of the event are derived from the Hillas parameters using lookup tables. Based on the reconstructed energy and the Hillas parameters, each event is classified as signal or background using Boost Decision Trees (BDTs) [47]. This method has an accuracy of 1% at the most sensitive part of the energy range, however, the limitation at low energies, around ~ 300 GeV, the miss-classification can reach up to 10%. The misclassified events are named gamma-like events and they compose the irreducible background which must be taken into account in the high-level analysis.

The high-level analysis consists of deriving physical information about astrophysical sources from the events detected. Due to the presence of gamma-like events, an accurate estimation of the background must be included in the analysis. Different methods for the background evaluation were developed, each of them optimized for different analysis goals. The estimation is based on OFF regions, which are regions with similar conditions as the region containing the source of interest, the ON region. Among the different methods, two classical ones are the ring background method with a focus on morphology analysis, and the reflected background method optimized for energy spectrum analysis [44]. A new method for background estimation was developed in 2019 [48], which consists of the same background estimation independent of the analysis goal. Further details about the ring, reflected and the 3D template background model is described in the following.

In the classical framework, for an accurate estimation of the background, the OFF region must be taken with the most similar conditions as the ON region. However, the acceptance to detect events is different across the FoV and usually assumed to be radially symmetric, which is the first order and is a good approximation. Figure 2.27 shows the acceptance in the function of the camera center distance for different zenith angles.

For the reflected background method, the OFF regions are chosen such that all the regions have the same acceptance as the ON region, thus at the same distance from the camera center. In the ring background method, OFF regions are

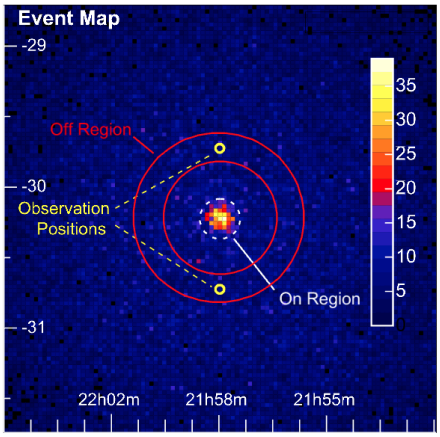

Figure 2.28: Description of the OFF region in the ring background method. The image is taken from [44]

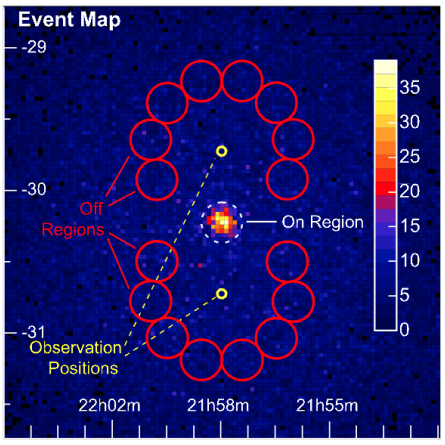

Figure 2.29: Description of the OFF region in the reflected background method. The image is taken from [44]

defined at different radial distances from the camera center such that the variation in the acceptance is taken into account. It is important to notice that these two methods rely on the assumption that the variation in the FoV is radially symmetric. In these two methods, the OFF region is derived from the same run as the ON region, therefore all regions have the same external features such as atmosphere, instrument conditions, and NSB level [44].

The ring and reflected methods are just two examples of the different types of background estimation. Some common limitations shared among the different methods are (I) lack of statistics - in which only morphology or spectrum can be analyzed per time, (II) extended sources - in which the definition of a source-free region as OFF region is not certain and (III) overlapping sources - challenging to disentangle the contribution of each source [44]. One alternative to compensate for the above mention issues is estimating the background with the 3D template background model [48].

A 3D template background model is a novel method in the IACT era. It consists of a template model providing the expected background from gamma-like events, based on averaging all source-free regions from many observations taken during the lifetime of the experiment. The model is built in three dimensions: two in space coordinates and one in energy, providing sky maps, with expected background events for a given sky direction and energy. Since the acceptance changes drastically accordingly to different instrument configurations, the model template is binned in the most critical parameters: zenith angles, azimuth angles, and energy. On top of that, further correction based on atmospheric conditions, zenith pointing direction within the zenith bin, and optical efficiency of the mirrors are applied.

To build a robust 3D template model, high statistics are required, meaning many source-free regions cover all the possible configurations, such as zenith angle, atmospheric conditions, etc. Due to this strong necessity for a high amount of data, this type of model was only possible to be developed recently, covering almost 15 years of accumulated data in H.E.S.S.. This model is independent of the radially symmetric assumption of the FoV, as the opposite of the ring and reflected method. Since the model is constructed by averaging many runs, the particular features of each run due to external conditions are vanished, causing some systematic effects in the model as discussed in the section **??**.

The 3D background model is available in FITs format, which can be handled by open-source tools, such as gammapy [46] and/or ctools [49]. The usage of this model supports the analysis using the maximum likelihood method, the same method used in the *Fermi*-LAT analysis, as described in the section 2.3.1. As in *Fermi*-LAT analysis, the data is binned into a cube whose axes are two spatial coordinates on the sky and one in energy. Assuming a specific statistical distribution for

the data and an a priori model. Then, the probability of the input model yielding the measured data is calculated for each bin in the cube. By varying the values of the parameters from the input model, the likelihood function is maximized and provides the best-fit values of the model of the astrophysical source.

2.4 The Galactic Center in Gamma Rays

Figure 2.30: Picture of H.E.S.S. telescope overlaid with gamma rays data observed from the galactic plane survey performed by HESS.

The center of our Galaxy provides a unique laboratory to understand the physics in a galactic nucleus. The region is detected across 18 decades in the electromagnetic spectrum, reaching up to gamma rays. However, it is opaque in the optical light, since a dust torus in the region absorbs the optical photons.

Each wavelength adds valuable insights about the region. From radio measurements, thermal and non-thermal processes are investigated, IR waveband traces star formation regions, and non-thermal X-rays and gamma-rays provide insights into particle acceleration and its interplay with the surrounding environment.

Contrary to the other wavebands, the origin of gamma rays emitted from the Galactic Center is still an open question. The complexity of the environment provides suitable conditions for different physical mechanisms to ignite gamma-ray emission. Moreover, the capabilities of the current gamma-ray instruments are insufficient to disentangle the dense abundance of sources leading to different source candidates responsible for the gamma-ray emission.

Thus, it is crucial for the astrophysical interpretation of gamma-ray emission a deep understanding of the radia-

tion mechanisms and the region components, such as the environment fields and local astrophysical sources.

This section is divided into three main parts. The first one focuses on the characterization of the region, introducing the available ingredients for the gamma-ray emission. The second part characterizes the gamma-ray emission from the central source of our Galaxy, focused on LAT and H.E.S.S. measurements. Finally, the third part discusses possible astrophysical models to explain the emission.

2.4.1 Characterization of the Region

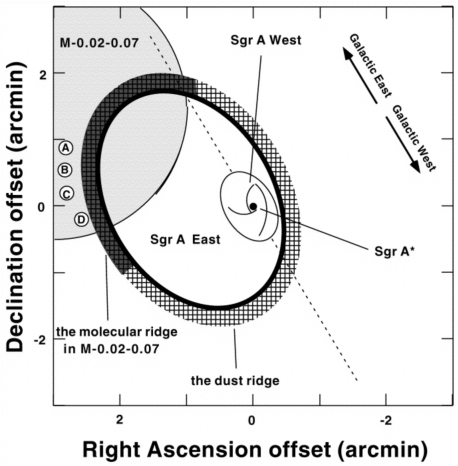

Figure 2.31: Illustration of the Galactic Centre region composed by Sgr A*, Sgr East, Circum Nuclear Disk, and Sgr West. Image is taken from [50].

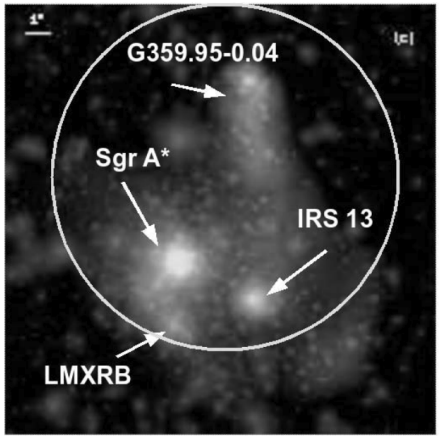

Figure 2.32: X-ray measured by Chandra and NIR measured by NACO composing the skymap. The outer white circle delimits the H.E.S.S. angular precision of 6″. Image is taken from [51].

The central 50 pc region is composed of (I) the compact radio source Sagittarius A* (Sgr A*), a Super Massive Black Hole (SMBH), (II) a three-arm spiral made of ionized hydrogen rotating around Sgr A*, named Sgr A West, (III) a Circum Nuclear Disk, torus-like molecular gas around Sgr A West, and (IV) an SNR enclosing all the previously mentioned regions, Sgr A East, which is interacting with a dense molecular cloud on the east side [52]. An illustration of these four components is shown in figure 2.31. Additionally, at a projected distance of 0.3 pc away from Sgr A* is located G359.95–0.04, a Pulsar Wind Nebula (PWN) [53].

Within the angular resolution of H.E.S.S., the most prominent astrophysical candidates responsible for the highest electromagnetic emission from the Galactic Center are Sgr A* and G359.95–0.04. Figure 2.32 shows a sky map with the position of G359.95–0.04 and Sgr A* enclosed in the white circle, which display the spatial gamma-ray emission from the central source detected by H.E.S.S.. Further details about these two sources are introduced in the following.

Sagittarius A* The SMBH Sgr A* is nested at the dynamic center of the Galaxy [55, 56], located at a distance of 8.2 kpc [57] from the solar system, with a mass of $\sim 4 \times 10^6\ M_\odot$ [58]. Since its first detection, in the radio band in 1974 [59], the description of the source has developed exponentially [60, 61], culminating in an image of the shadow of Sgr A* in 2022 (figure 2.33) made by Event Horizon Telescope in radio frequency [54].

Surprisingly, Sgr A* has an unexpectedly low bolometric luminosity $\leq 10^{-8}\ L_{Edd}$. The low luminosity allows the region to be transparent to gamma rays, otherwise, they would strongly interact with the dense low-energy photons igniting e^+e^- pair production. The overall electromagnetic emission is characterized by a steady state and a flaring state.

The steady emission is well explained by a thermal population of relativistic electrons emitting radiation due to the Synchrotron process. Figure 2.34 presents the spectrum in the steady state covering 12 decades in energy. The gamma-ray

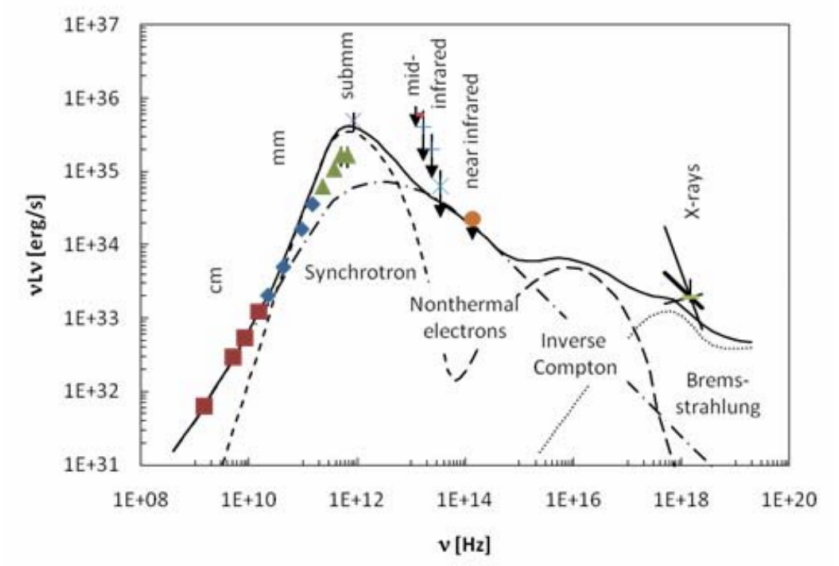

Figure 2.34: Multi-wavelengths Sgr A* Spectral Energy Distribution, as colored data points, and possible underlying model. For a full description consult figure 7.1.1 from ref. [62].

data is not shown since the resolution of the instrument does not firmly confirm the emission from Sgr A*.

On top of the steady emission, flares are observed in IR and X-rays a few times per day lasting ~ 100 minutes. These phenomena could be created to due transiently heated electrons, although it is still under debate [62].

PWNe G359–0.04 The PWN G359–0.04 was discovered in 2016 in the X-ray band by the Chandra satellite. Located at an 8.7″ projected distance from Sgr A*, it overlaps Sgr A* within the H.E.S.S. angular resolution. Its luminosity of 10^{34} erg/s in the energy range of 2–10 keV is four times brighter than the Sgr A* in its quiescent state [53].

Its emission is only visible in X-rays and requires a non-thermal electron population cooling down via the Synchrotron mechanism. This implies a lower limit of the magnetic field of the order of 10^{-4} G [63]. The presence of non-thermal electrons in the unavoidable intense GC radiation fields naturally results in gamma-ray production, making G359–0.04 a strong candidate responsible for the gamma-ray emission.

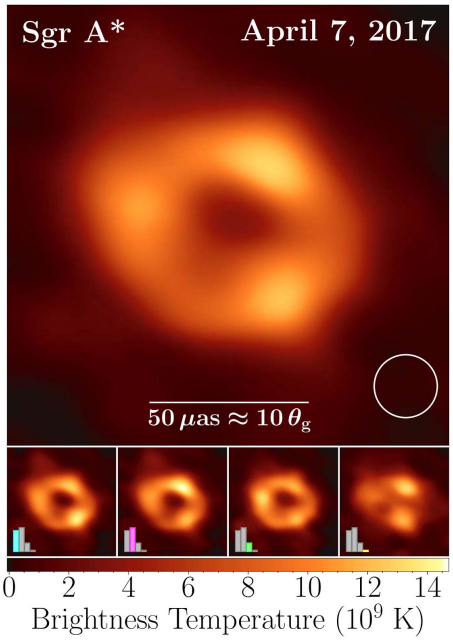

Figure 2.33: First image taken of Sagittarius A*, the SMBH at the center of our Galaxy. Image taken from [54]

Environment Fields

Dense matter and radiation fields are pervading the region and embedding the astrophysical sources. The accretion disk around Sgr A* presents dense matter fields, ~ 10^3 particles/cm^3. The UV and NIR radiation fields ~ 5000 eV/cm^3 are ~100 times higher than at 10 pc distance. The magnetic field of ~ 50μG is on average one order of magnitude higher than the rest of the Galaxy [62].

The rich environment provides suitable conditions for radiation production, including gamma rays. The combined analysis with different instruments provides access to the different radiation mechanisms, enriching the knowledge about the region. A good example is the constraint on the magnetic field from X-ray measurements of G359–0.04 [53].

Transitory Visitors

Visiting objects in the region might also assist in the description of the region. For instance, analysis of individual star tracks [64, 65, 66] and relativistic redshift from stars [67] traveling through the region confirmed Sgr A* as an SMBH. Passage of stars could in principle decrease the gamma-ray detected flux due to the interaction of gamma rays with lower energy photons, resulting in the production of e^-e^+ pairs. However, as demonstrated in [51] the current instruments are not sensitive enough to detect such flux variation for the studied star sample.

Another interesting visiting object is the G2 cloud [68, 69], detected in 2012, whose periastron occurred in 2013 [70]. Strong flares were speculated due to its passage since the infalling material of the cloud was expected to be of the order of the accretion rate of Sgr A* [71]. However, no significant increase in activity was detected in IR, X-rays [72, 73] nor in the gamma-ray band [74, 75].

2.4.2 The Gamma-Ray Spectrum from the Galactic Center

The gamma-ray measurements from the GC with IACTs started in 2004, by Whipple and Cangaroo II observatories [76, 77]. As the current generation of IACT came online, H.E.S.S., MAGIC, and VERITAS, also reported a detection, describing the spectral emission as a power-law function with a spectral index of 2.2 [78, 79, 80].

With the maturity of the field and the analysis, the description of the source emission evolved to an exponential cutoff power law with a spectral index of 2.10 and cutoff energy at 14.70 TeV, with no time variability [81, 75]. This result is confirmed by all the current generation of IACT observatories [81, 82, 83].

The signal is observed up to dozens of TeV, with a flux of order of 10^{-12} TeV^{-1}cm^{-2}s^{-1} for energies above 1 TeV. Towards lower energies, the spectrum is measured by LAT, with a log-parabola shape. The high energy end of the spectrum measured by LAT is in agreement with the low energy end of IACT data. The low energy end of the LAT spectrum is characterized by an increase towards low energies from 100 MeV.

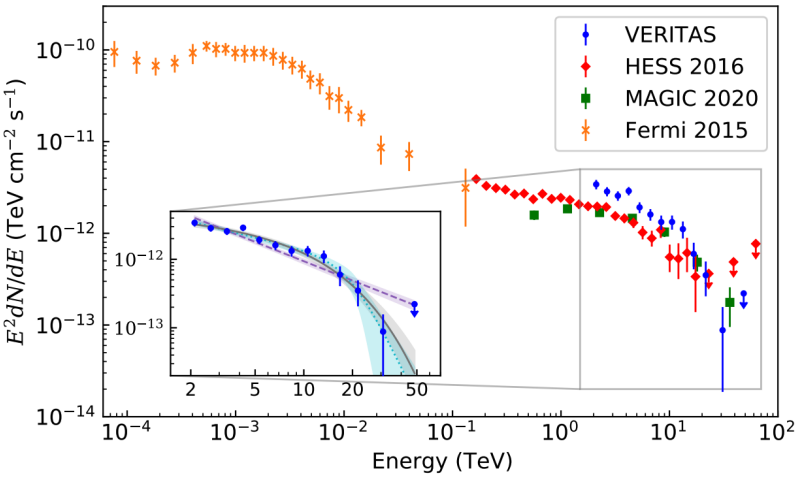

Figure 2.35: Compilation of flux points from *Fermi*-LAT and IACT data obtained individually by each observatory. Image taken from [82], further information is presented in figure 3.

The combined spectrum, from 100 MeV to 100 TeV, presents two distinct components: a log-parabola for the LAT observations, shown as orange data points in figure 2.35, and an exponential cut-off power-law for IACT range, shown by the red (H.E.S.S.), green (MAGIC) and blue (VERITAS) data points in the same figure.

It is worth noting that the resolution of the gamma-ray instruments is the limiting factor to firmly distinguish the source origin of the emission. Thus, it is also possible that the GeV and the TeV emission have different origins that are spatially overlapping within the spatial resolution of the current instruments.

Overlayed with the point-like astrophysical sources, the diffuse emission from the Galactic Plane hampers the description of the central source. The Galactic Plane diffuse emission in Very High Energy (VHE) gamma rays extends to ~ 200 pc from the Galactic Center and its emission is a result of the interaction of accelerated protons with the extended molecular clouds in the Galactic Plane [84]. The absence of a cut-off in the diffuse emission spectrum leads to the claim of a PeVatron source located at the center of the Galaxy responsible for the gamma-ray emission [85, 82]. However, there is no proven association between the PeVatron and gamma rays from the central source.

The signal coming from the GC region is associated to the source 4FGL J1745.6—2859 in the *Fermi*-LAT 4th catalog [32] and HESS J1745–290 in the H.E.S.S. catalog [45].

4FGL J1745.6–2859 The source is currently described using 14 years of LAT data and associated with previous catalog sources 2FGL J1745.6–2858 and 3FGL J1745.6–2859c. Its electromagnetic emission has a log parabola shape.

It is a point source located at (266.415°, -28.997°) in ICRS coordinates, and considering the *Fermi*-LAT PSF the source

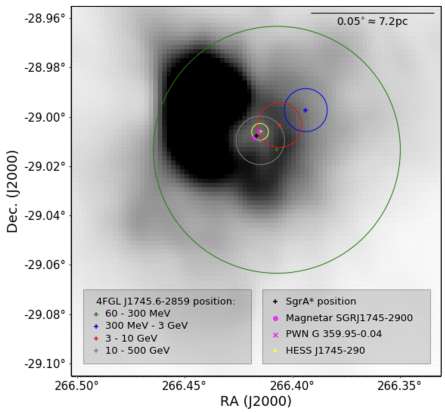

Figure 2.36: Best fit position of LAT emission from 4FGL J1745.6–2859. Image is taken from [86].

covers a region of 10–100 pc, considering 8.3 kpc distance from the GC. A detailed imaging analysis of the source position indicates that as the energy increases, the position of the emission gets closer to Sgr A* position, as shown in figure 2.36 [86].

HESS J1745–290 First detected in 2004, the source HESS J1745–290 has a gamma-ray luminosity of 10^{35} erg/s in the range 1–10 TeV. Its detection can reach energy as low as 165 GeV, due to H.E.S.S. privileged location, in the Southern Hemisphere, which allows observation at low zenith angles.

It is currently described as a steady emission, with the spectral shape of an exponential cutoff power law, with cutoff at $\sim$ 10 TeV. It is a point source located at (266.42 °, -29.01°) in ICRS coordinates, with a spatial resolution of order 6″ per axis, spanning a region of 10 pc [81, 87]. However, previous analysis had an initial resolution of 20″ including also Sgr A East as a possible candidate responsible for the gamma-ray emission [88].

2.4.3 The Astrophysical Models for the Gamma-Ray Spectrum

The gamma rays, being the most energetic tail of the electromagnetic spectrum, are a direct trace of the sites with high-energy CR. Additionally, features in the spectrum might shed light on the physical process in such rich environments. However, the astrophysical interpretation of the gamma-ray emission from the GC is still unidentified. Partially due to the lack of resolution of the experiments, but also due to the complexity of the region.

It is still unknown whether the two components describing the GeV-TeV gamma-ray spectrum have the same origin. Although there are examples of particular sources, such as Crab Nebula [4, 5], in which a simple model describes the whole spectrum, a connection between GeV-TeV populations is not mandatory [89]. Simple models can explain either GeV or TeV emission from the central source. However, the connection of the two components requires more complex models.

The models for the gamma-ray emission can be parametrized by: a source responsible for accelerating the parent particles, the nature of the parent particle (leptonic or hadronic), and the energy range of the emission. The nature of the particle in the model bounds the radiation mechanism, p-p interaction for hadronic, and IC for leptonic models.

The models differ among them by varying the underlying assumptions. Commonly these are: structure of the surrounding environment, transport and diffusion of the charged particle, and the type of injection (flare of continuous emission). The

multi-wavelengths and multi messages analysis advocate for certain models.

Some general features that assist the models are listed below.

- All hadronic models expect neutrino productions. No neutrinos coincident with GC was detected up to date [90, 91]. The absence of neutrino measurements can be explained by the insufficient sensitivity of the instruments to the low produced flux, and therefore this model can still explain the gamma-ray emission from the central source.
- The leptonic scenario produces easily a connection with X-rays and IR measurements since the emission for these wavebands is due to Synchrotron emission, which requires electron population. However, no increase in the H.E.S.S. flux in a time coincidence with X-ray flares was detected [92]. This could indicate different regions for the X-ray and gamma-ray emission.
- Assuming recurrent burst episodes for the injection of particles, if they occur with a time interval shorter than the cooling time of particles, the detected gamma-ray emission is likely to be seen as a steady emission.
- The diffusion of protons through the matter field depends on the energy. Higher energy protons interact less, having a longer free mean path, while lower energy protons, interact more and consequently have a shorter free mean path, as argued in [22, 93]. This could imply that the cooling of different energy protons happens in different regions.
- Although it is tempting to link the central source emission with the PeVatron responsible for the diffuse emission [85], there is no clear connection between them.

The overall collection of available models in the literature can be found in table 2.1. It is sorted by temporal order and it shows its main features: the astrophysical source responsible for the particle acceleration, the type of parent particle, the experiment that covers the emitted energy range, particularities of the model, further measurements endorsing the model, type of injection and finally in the last column measurable predictions by the model.

Among the proposed models, there are two possible models to be tested [23, 93] using the current amount of data (almost 20 years of HESS data and 14 years of *Fermi*-LAT data). They rely on the assumption of spectrum variation, due to the flaring origin of the parent particle. Given the efficient cooling of the high-energy particles, changes in the spectrum might be observable in the time scales of accumulated data. These two models are tested in this work and presented in chapter 4.

Considering only LAT data, there are also other hypotheses to explain the emission besides the acceleration of charged particles, such as Dark Matter and the population of unidentified point sources. However, the coverage of the other models is outside of the scope of this work.

The interpretation of the gamma-ray data is complex, reflecting the complexity of the region. A complete description of the region with the current instruments is challenging and the models here introduced are basic, having a high degeneracy among the parameter values of the models. Moreover, it is also feasible the emission is a combination of different processes and astrophysical sources.

The disentanglement of each component is challenging with the current instruments. However, the future IACT observatory CTA, with its improved sensitivity and resolution, will bring new insights into the region [94].

Table 2.1: Compilation of different astrophysical models available in the literature for the emission of the central source from either or both *Fermi*-LAT and H.E.S.S..

Model ref	Astrophysical source for acceleration	Parent particle	Experiment	Main model features	Further info supporting the model	Injection type	Prediction
Atoyan 2004 [95]	Sgr A*	e^-	H.E.S.S.	A process similar to pulsar-powered plerions, TeV emission is derived from the wind termination shocks, which shares the same origins as the quiescent radio and flaring NIR and X-ray emissions.	Radio and X-rays would share the same electron population although it is not expected time coincident between these bands and gamma rays.	Flare	Expected variation ~100 years.
Aharonian 2005 [96]	Sgr A*	p^+	LAT + H.E.S.S.	It is presented three different scenarios for emission with protons. From p-p process, secondary electrons are created, which for certain parameter values could emit at MeV/GeV energies and/or explain radio to IR bands emissions.	In this scenario, the secondary electrons would also result in IR-X-ray emissions.	Flare	Neutrinos production and strong X-ray-IR correlations.
Hinton 2007 [63]	G359.95–0.04	e^-	H.E.S.S.	Dense radiation fields in the central 1pc	SED based on X-ray measurements	Continuous	
Chernyakova 2011 [22]	Sgr A*	p^+	LAT + H.E.S.S.	An energy-dependent proton propagation, as being diffuse for low energy and rectilinear at high energies.		Continuous	Improved satellite spatial resolution would be able to support this model
Ballantyne 2011 [93]	Sgr A*	p^+	H.E.S.S.	Time and energy dependency of the proton transport, with rapid diffusion of high energy protons and flaring scenario. A burst of a few years long occurring ~10 years ago can explain TeV emission. The TeV emission is stable over the years when such bursts are frequent.		Flare	Shortest variability in timescales of ~5 years emission 10 TeV.
Linden 2012 [97]	Sgr A*	p^+	LAT + H.E.S.S.	The emission is dominantly ruled by gas morphology rather than proton transport. The emission spatial distribution decreases with energy, thus the GeV emission is expected to have larger radius than the TeV emission.		Continuous	CTA high angular precision might be able to support this model
Fatuzzo 2012 [98]	Sgr A*	p^+	LAT + H.E.S.S.	Two-phase environment: a molecular torus (inner radius 1.2 pc, thickness 1pc) and an interstellar medium from shocked stellar winds (inner parsecs).			
Kusunose 2012 [99]	Sgr A*	e^-	LAT	Flares with the same origin as the one causing NIR/X-ray flares. The electrons which scape the flare accumulate in a 10^{18} cm region, which interacts with the photon field emitting GeV through IC.		Flare	
Guo 2013 [100]	Sgr A*	$p^+ + e^-$	LAT + H.E.S.S.	The GeV emission is due to IC scatter of electrons with the photon field, while the TeV emission would originate from the interaction of protons with the matter field.			
Yusefzadeh 2013 [101]	Sgr A*	e^-	LAT + H.E.S.S.	GeV emission from bremsstrahlung interacting with neutral gas. TeV emission upported by bremsstrahlung and synchrotron emission from radio emission extrapolation of radio data to infer electron population			
Malyshev 2015 [23]	Sgr A*	e^-	LAT + H.E.S.S.	Combination of a flare occurring ~ 300 years ago, to explain the LAT data and a continuous particle injection to explain the TeV emission. The higher energy electrons cooled down faster and the current measured emission is from the remaining lower energy electrons, which requires longer cooling time.	Measurement in the MeV shows the absence of a cutoff, expected in the case of a pure hadronic scenario. This strongly advocates for a leptonic scenario.	Continuous + flare	5–10% flux decrease in the 1–10 GeV interval in the timescale of ~10 years.
Kistler 2015 [102]	Sgr A*	e^-	LAT + H.E.S.S.	Considers energy and angular dependence of the photon field. It maps the gamma-ray extinction	Diffuse hard X-rays		

Systematic Errors of 3D Background Model

3

Understanding the systematic error is crucial to ensure the robustness of the analysis. Systematic error is presented as a consistent shift of the result from the true result. It can arise from different origins, present different patterns, and might even cancel out through the process.

In the data the systematic error is entangled with the statistical error, resulting in an observed total error as:

$$\sigma^2_{total} = \sigma^2_{statistic} + \sigma^2_{systematic}. \tag{3.1}$$

As N, the number of data points goes to infinity, $\sigma_{statistic}$ converges to a normal distribution while $\sigma^2_{systematic}$ behaves as a consistent shift from the true value. Thus, deviations from a normal distribution of σ^2_{total} indicate the presence of systematic error. However, in a realistic frame with finite N, when the systematic errors are at the level of the available statistics $\sim 1/\sqrt{N}$, the separation of the errors is not readily possible.

Figure 3.1 illustrates the situation above described. For the accurate case, the left plot shows a precise measurement in which the fluctuation is within the expected, while the right plot shows the case with higher statistical fluctuation. The lower row shows the systematic error present as a constant shift from the true value. The bias results can also be precise, with fluctuation within the expected, or not precise with a large spread. As the spread increases, it is less reliable to define the systematic level based only on the mean value.

The estimation of systematic errors in the 3D template background model, since it is a novelty in IACT analysis, is crucial to assess its reliability. Some methods are proposed for the estimation of the systematic errors for a 3D background template [103, 104]. However, they are dependent on the data considered.

This work presents a method for quantitatively estimating the systematic errors for a 3D background template model. As a consequence, some origins of the systematic errors in the studied model version are exposed. In addition to the error estimation, corrections in the model are proposed through an alternative model version.

From the systematic error level estimation, lookup tables are built, which are further used to estimate the systematic error of any dataset for a 3D analysis. The systematic error, that is present in a dataset due to the background model estimated from the lookup tables, is further introduced in the analysis through a technique using nuisance parameters.

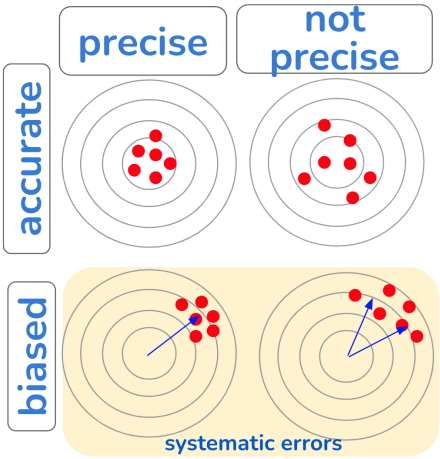

Figure 3.1: Explanatory illustration of statistical and systematic errors. The upper low presents the case of only statistical error present, while the lower row presents both systematic and statistical errors. The different columns show different levels of statistical errors, the first one being more precise, with fewer statistical errors compared to the second column, with higher statistical errors.

The final analysis provides a broadening of the energy range by adding data with proper treatment of systematic errors in the background model.

Thus, this chapter aims to investigate quantitatively and qualitatively the systematic errors of the 3D background model. To accomplish that, the chapter is structured as the following:

- 3.1.2 Introducing the analysis pipeline, in the context of the 3D background model.
- 3.2.1 Defining the key parameter for quantifying systematic errors.
- 3.2.2 Describing the influence of the analysis pipeline in reproducing the systematic errors as measurable outputs.
- 3.3 Identifying the most prominent causes of systematic errors.
- Quantifying the systematic error per run and building lookup tables.
- Establishing a method for quantification of systematic error for any dataset using the lookup tables.
- Evaluation of systematic error in a test dataset and the improvement of the corrections.
- Caveats, conclusions, and outlook for this method.

The method developed through this work is independent of the model version, as long as it is a 3D template background model. Also, since the model provides lookup tables, the method is suitable for any dataset considered for the analysis, in opposition to the current few used methods.

This work uses the 3D background model from H.E.S.S. [48], using the HAP-HD chain, with std_zeta_fullEnclosure configuration.

3.1 The 3D Background Model Context

The 3D background model for IACT data opens doors for the analysis of complex and crowded regions with modern analysis, using powerful statistical methods. Additionally, it converges the analysis techniques used for gamma-ray satellites and IACTs.

The following sections are dedicated to describing in detail the steps of the maximum likelihood analysis for the H.E.S.S. data. The following section is structured in (i) describing model features that are relevant for the understanding of the systematic errors, and (ii) the analysis pipeline using the 3D template model.

3.1.1 Detailed Description of the Model

The 3D template background model provides the expected number of background events from any sky direction, for

any energy in the IACT range. Its construction is based on averaging gamma-like events observed in source-free regions [48].

The gamma-like events are events that survived the criteria on the gamma-hadron separation. In H.E.S.S. it is done using Boosted Decision Trees (BDTs) [47]. This procedure is one step before the model construction and features inherited from BDT could potentially affect the analysis.

The model is constructed in bins of the axes presenting the highest variation: zenith, azimuth, and energy. The choice of the axes and their bin sizes is a compromise between available statistics and the precision of the model. Thus, each run is assigned to a specific model bin, according to the run's zenith and azimuth direction. Additionally, the assigned model passes through a fine adjustment to the run's features.

Interestingly, the model is spatial asymmetric in the FoV for low energies. This is controversial to the basic assumption of radial symmetry in the classical background estimation. The asymmetry in the model arises due to a gradient in the detection acceptance caused by the zenith gradient across the FoV [48]. As shown in figure 2.24, the effective area, which is dependent on the acceptance, presents different cutoff energies for different zenith angles. In a low-energy bin, this effect is observed as more photons are detected in the direction of the lower zenith direction. However, as the energy increases, the spatial model gradually becomes radially symmetric. For further details see figure 12 from [48].

The version of the 3D model is highly dependent on the configuration used. A compilation of the used parameters in the model construction which is used in this work is shown in table 3.1.

Table 3.1: Parameters in the 3D background model used in the construction useful for the systematic error investigation.

Parameter	Values
Zenith bins [deg]	[0, 15, 25, 35, 42.5, 47.5, 52.5, 60]
BDT edges [TeV]	[0.1, 0.3, 0.5, 1, 2, 5, 100]
Maximum zenith [deg]	60
Configuration	std_zeta_fullEnclosure

3.1.2 Analysis Chain in Gammapy for 3D Background Model:

This section aims to describe the analysis pipeline using the 3D background model. It is described using the gammapy software [46] version 1.0 [105] and its specific functions for each step. The procedure is similar to other tools, such as ctools [49].

The input of analysis is a list of runs that observed the region/-source of interest. The outcome depends on the analysis goal, however, it is common to obtain the spectrum and/or the morphology characteristics of the source. Additionally, flux

points, significance maps, and their distribution are common outputs to attest to the robustness of the analysis.

The analysis pipeline can be divided into two consecutive procedures. In the first part, namely here as 'setting the environment', the background model is adjusted on a run-wise basis and then they are combined into one stacked *MapDataset* object. This *MapDataset* is the input for the second part, namely here as 'source analysis', in which the common outputs, such as source spectrum and morphology, are derived. Furthermore, to inspect the reliability of the results, additional information, such as significance maps, can be extracted. Figure 3.2 presents a flowchart to illustrate the entire process.

Setting the Environment

The input of this part is a run list and the output is a stacked *MapDataset*, which condenses the information from the input runs. For convention, functions or objects used from gammapy, as *MapDataset*, is written in italic. Further information about the functions can be found on the gammapy webpage*.

The *MapDataset* is the base of the 3D analysis. It stores information into different 3D arrays—cubes binned in space and in energy. In *MapDataset* is stored, among others, a counts cube, with the number of detected events, and a background cube, with the expected number of gamma-like events derived from the background model. A *MapDataset* is created per each run and by summing them, the stacked *MapDataset* is obtained.

The goal of this part of the analysis chain is to adjust the background model to the data for each individual run. It is done by fitting a normalization and tilt of the background model spectrum to the data. To achieve it, the steps to be followed are set in bold.

Defining the geometries of *MapDataset*:
The geometry of the parameters space, in spatial and energy coordinates, must be predefined to build a *MapDataset*. For it, one must choose:

- FoV of the sky - it is set to 5 deg, based on the FoV of the telescopes used CT1-4.
- Spatial bins - 0.02 deg/bin, canonical value.
- Geometry's center - often set as the source position. For systematic studies, the center of the geometry is set as the run's pointing direction.
- Energy range - [0.1-100] TeV, which is the energy range of IACTs.
- Energy bins - 8 bins/decade, canonical value in IACT analysis.

It is worth noting that this analysis assumes canonical values, however, they are not universal and can be modified according

* gammapy webpage

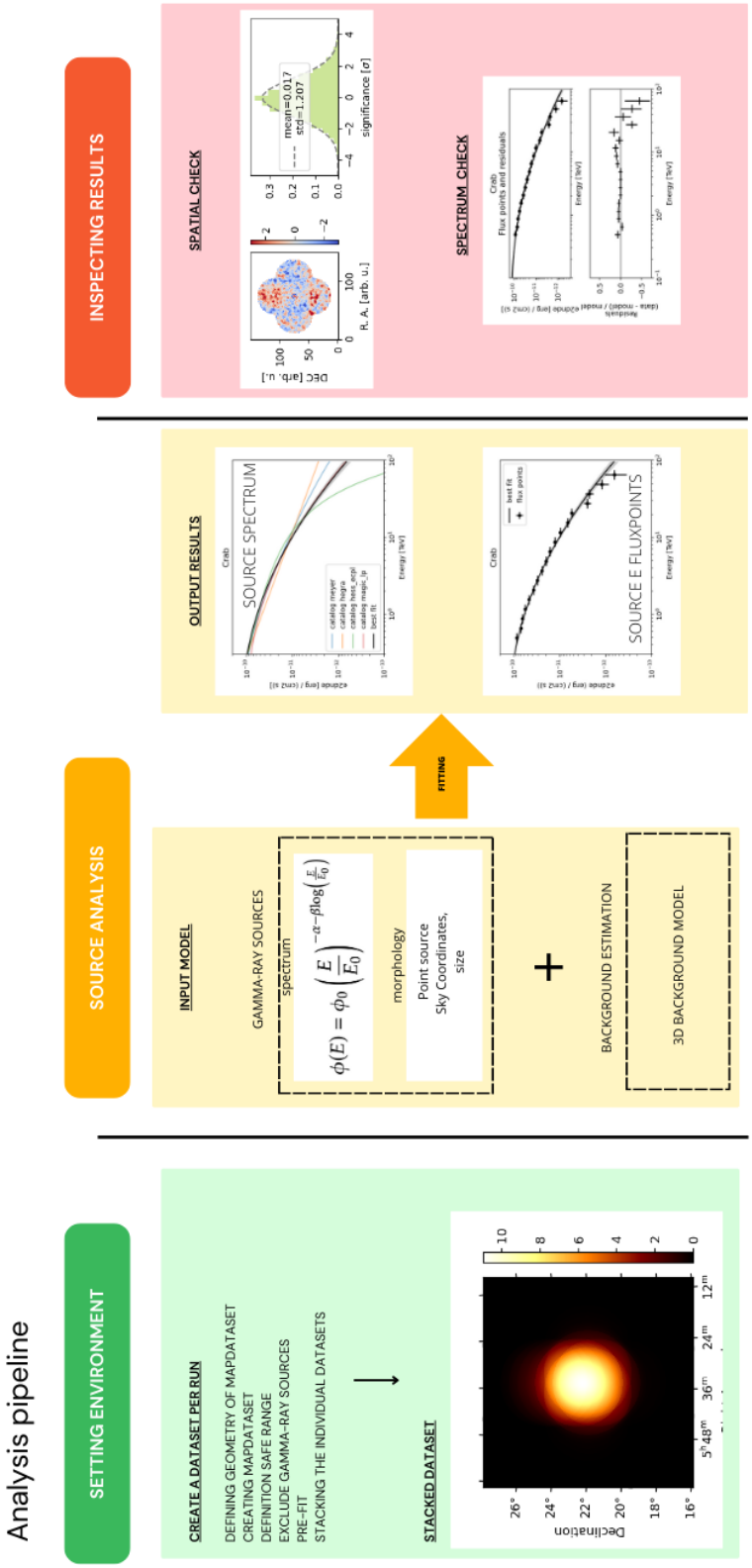

Figure 3.2: Fluxgram for the 3D analysis.

to the needs of the analysis. Moreover, the definition of the energy bins in this step defines the energy bins in the estimation of systematic errors.

Creating the *MapDataset*:
For each run from the input run list, an individual *MapDataset* with the geometry above described is created with *MapDatasetMaker*.

Definition of safe range - mask_safe:
The energy and spatial ranges are restricted in gammapy with *safe_mask_maker*. The usage of the incorrect range leads to non-convergence or unrealistic best-fit values in the maximum-likelihood analysis. Thus, the regions which provide an inaccurate description of the data must be masked.

In energy:
This mask is especially important at low energies, where the data presents higher systematic errors, as it will be presented later in this section. The definition of the low energy threshold depends on the analysis goal. In gammapy, the *safe_mask_maker* allows three different method for defining it: *aeff-default*, based on effective area, *edisp*, based on energy dispersion or *bkg-peak*, based on the background model.
aeff-default: This is generally the lowest value for the low energy threshold. The effective area has a rapid increase at low energies, as seen in figure 2.24. This approach defines the low energy threshold as the energy in which the effective area has a variation less or equal to a certain value, commonly used as 10%.
edisp: This procedure is similar to aeff-default, by defining the low energy threshold at the energy in which the variation of the IRF energy dispersion is less or equal than a certain value, again commonly used as 10%.
bkg-peak: This procedure defines the low energy threshold at the energy at which the peak of the background spectrum occurs. Note that this is the only method relying on the background model and not on the IRFs.
On top of that, the most conservative approach provides the highest value of the low energy threshold by combining the three methods. The most liberal approach provides the lowest value of the low energy threshold, and it is defined by *aeff-default* method.

In space:
This mask is relevant because the further from the FoV center, the poorer the model, due to less available statistics at large distances from the FoV center. Thus, it is commonly used as a spatial mask of radius 2.5°, corresponding to the size of CT1-4 camera FoV. It can be done by using the method 'offset-max' in *safe_mask_maker*.

Exclude gamma-ray sources - mask_fit
To adjust only the background model to the data, the gamma-ray sources must be ignored, but not totally excluded from the data. This is done in gammapy with *MapDataset.mask_fit*. The

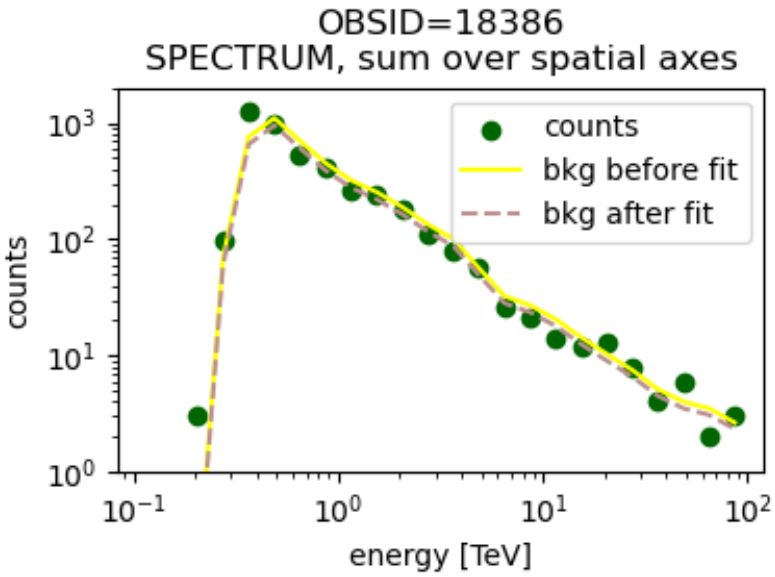

Figure 3.3: The spectrum for data, green dots, and background before, yellow curve, and after the pre-fit process, dashed salmon curve, for observation run 18386.

gamma-ray sources' location and their respective morphology (size) can be taken from catalogs.

Pre-fit
This step is named pre-fit because it fits only the background model spectral shape is fitted in the source-free data. The free parameters for this step are a normalization and tilt in energy and the best-fit values are found through the maximum likelihood method.
In gammapy, the procedure is created by the function *FoVBackgroundMaker*. In case the background model describes perfectly the data, the best-fit normalization and tilt must be 1 and 0, respectively. Small variation from these values is acceptable; however, large variations indicate problems in the run and/or the model.
Figure 3.3 shows a comparison of the background before and after the pre-fit procedure. There is no big difference between the spectrum before and after the fit, as expected, for normalization ~ 1 and tilt ~ 0, and they agree with the measured data. Nevertheless, this step is one more possibility to improve further the description of the data.

Stacking the individual datasets
Once the background is adjusted for each run, each individual *MapDataset* is merged into one *MapDataset*. The final *MapDataset* mergers the individual runs and its respective characteristics as the adjusted background and the IRFs. It is worth noting that the stacking procedure considers only the run's data in the safe range, defined by *MapDataset.mask_safe*. Thus, the range in which the data is poorly described is excluded from the stacked *MapDataset*. On the contrary, the data masked by *MapDataset.mask_fit* is included in the stacked *MapDataset.mask_safe* since it is used only for the background

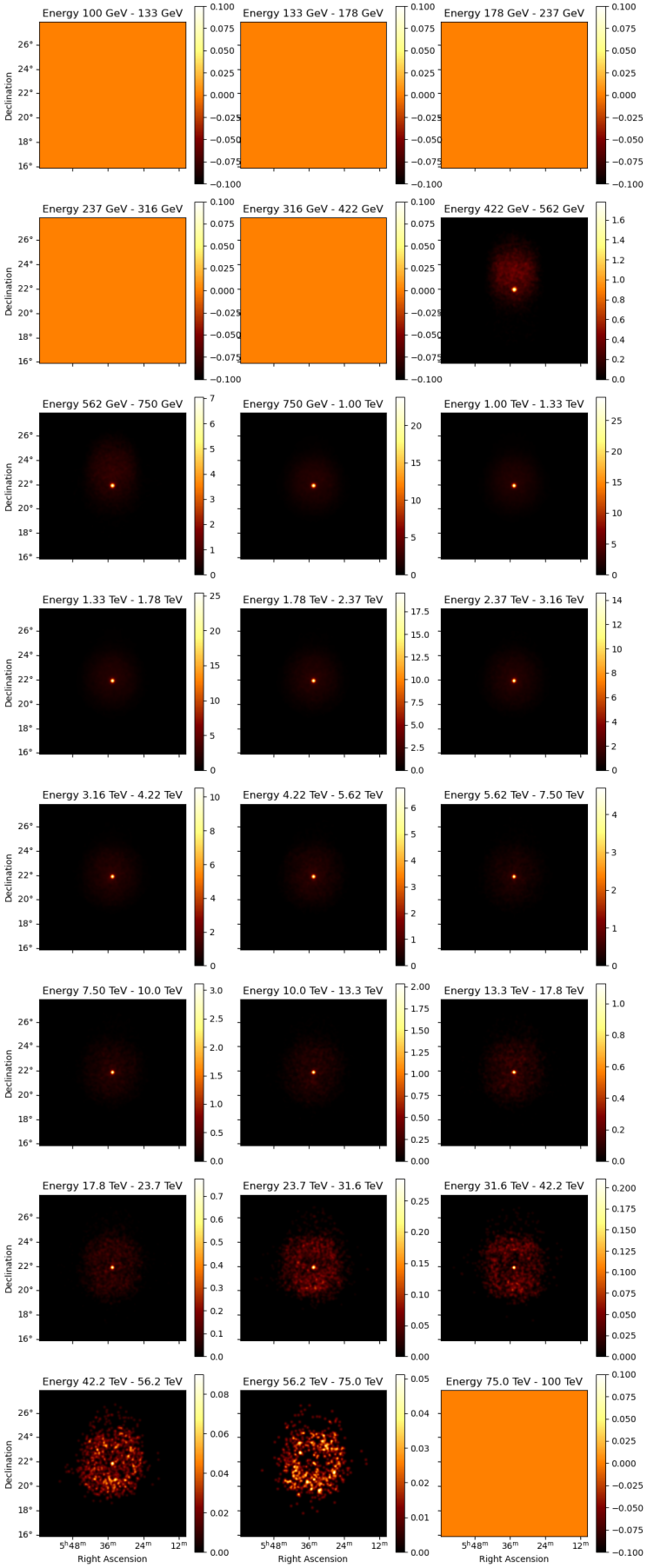

Figure 3.4: The counts cube from the stacked *MapDataset* for a source example, Crab. For each energy bin, there is a skymap containing the sum of events measured from all runs. The orange-colored skymaps indicate the energy bins excluded by *MapDataset.mask_safe*. The skymaps have the same geometry and are centered at the source position.

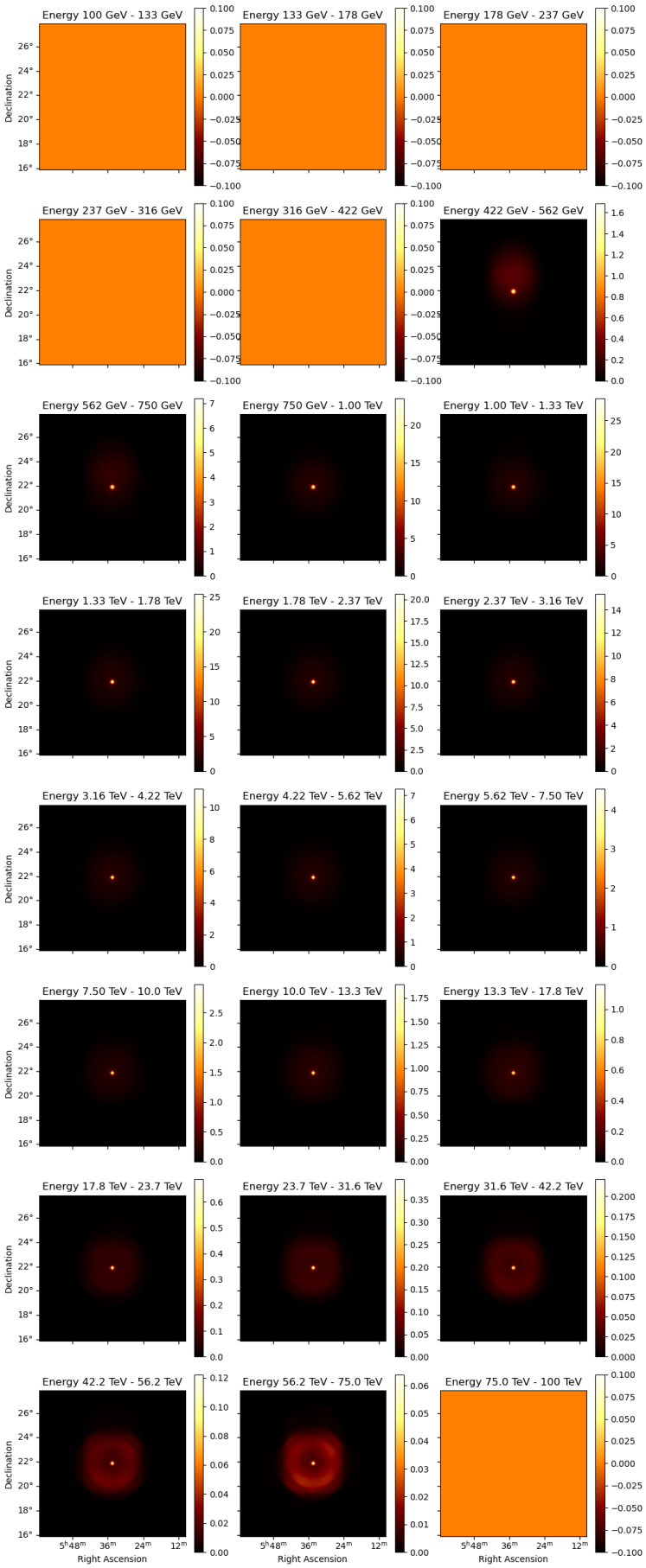

Figure 3.5: Cube of *MapDataset.npred()*. The concept is similar to figure 3.4, but the events displayed are expected events given the input models.

pre-fit.

The output: stacked *MapDataset*
Figure 3.4 shows the stacked *MapDataset* for the measured data. At the center of the sky maps, it is observed a bright point where more events are detected, revealing a gamma-ray signal coincident with the source position. The color scale is different for each energy bin, caused by variations of the source signal in the energy. In addition to the color scale, the spatial distribution of the events also varies with energy. Since there is no other known gamma-ray source in the FoV, the events not coming from the center of the FoV are due to background. The different patterns in the sky maps show the different ratios of signal/background present in this dataset.

A compilation of the stacked *MapDataset* is shown in figure 3.6.

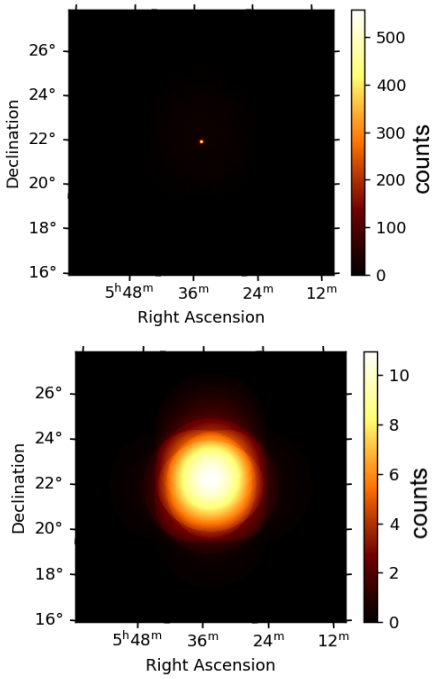

Figure 3.6: Stacked *MapDataset* for Crab example, integrated in energy. The upper plot shows the skymap of the measured events while the bottom plot shows the background event expectation, both in units of counts.

The Source Analysis

The analysis based on the maximum likelihood fit requires an input model which predicts all the data measured, source, and background. This approach supports complex input models and even spatially overlapping sources, which is not the case in classical IACT analysis. As a consequence, this technique allows a more precise investigation of crowded and complex regions.

In gammapy, the source model is described by the object *SkyModel*, which includes information about the source's morphology and spectrum. For the analysis, the input models are convolved with the exposure time and IRFs stored in the stacked *MapDataset*. The object *MapDataset.npred()* provides the expected number of events, from the input source models, for this stacked *MapDataset*.

For the Crab stacked *MapDataset* example, there are two different contributions of gamma rays. The Crab source and the background. The background model is built in the stacked *MapDataset* through the pre-fit procedure. The Crab model is described as a point source with a log-parabola spectrum shape, as defined in the equation below:

$$\phi(E) = \phi_0 \left(\frac{E}{E_0}\right)^{-\alpha-\beta\log\left(\frac{E}{E_0}\right)} . \tag{3.2}$$

Figure 3.5 shows the cube of *MapDataset.npred()*. The similarities in the patterns observed in both figures, such as the spatial distribution of the background in the first and last energy bin, are a good indication of a reasonable input model.

The probability of each bin in *MapDataset.counts* be due to *MapDataset.npred()* is calculated and summed up, providing the total probability. By varying the values of the input

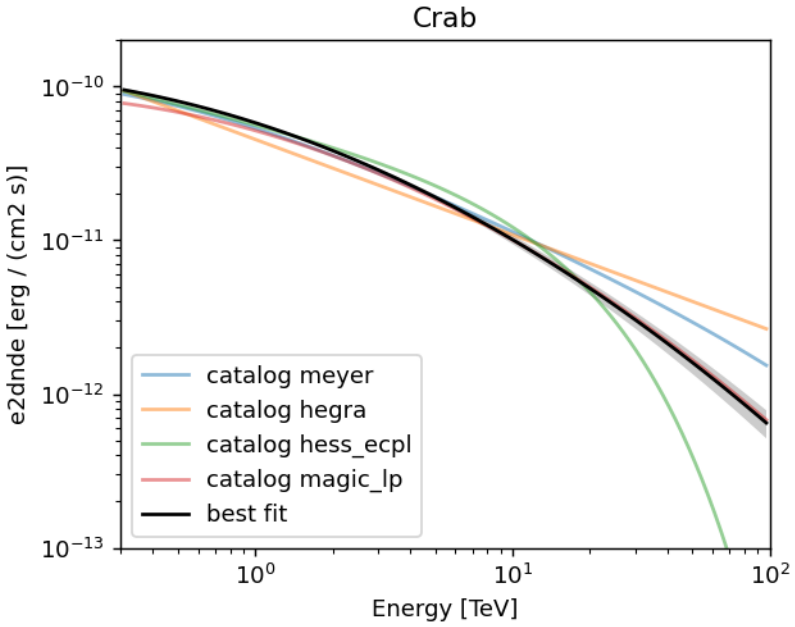

Figure 3.7: Spectrum models for the Crab source available in the literature. The name in the legend refers to the method used in gammapy with *create_crab_spectral_model*: 'meyer' from [4], 'hegra' from [106], 'hess_ecpl' from [27] and 'magic_lp' from [29]. The best-fit spectrum considering a log-parabola spectral model is displayed as a black curve, with 1 sigma statistical uncertainty as the gray band.

Table 3.2: The Crab spectrum parameter values for the input model and the best fit.

spectral model (log parabola)	input value	best fit value
$\phi_0 \times 10^{-11}$ / (cm2 s TeV)	3.84	3.63 +/- 0.029
α	2.5	2.534 +/- 0.02
β	0.105	0.098 +/- 0.01

model parameters, for instance, ϕ_0, α, β, the total probability also varies. The parameter values that maximize the total probability are defined as best-fit values and it is the model values that best describe the data.

Table 3.2 shows the input values and the best-fit values for the spectrum parameters of Crab source analysis.

Figure 3.7 shows different possible spectrum models for Crab [4, 106, 27, 29] and the comparison of the best-fit model. Any of these models could be used as an input model; although, the higher the number of free parameters, the more computationally expensive. In case the model is not compatible to fit the data, the fit does not converge or leads to unreasonable values. Another important point is that the method optimizes the best-fit values for the provided input model; however, other model shapes might describe the data better.

Another important outcome in the analysis is the flux points, further description about it can be found in [45, 107]. The flux points consist of the expected energy flux for individual energy bins, while the best-fit spectrum comprises the description of the source in the function's parameters. Since the flux points afford a higher degree of freedom, with more parameters, it can reveal features in the data, that are hidden when considering only the best-fit spectrum for a given model.

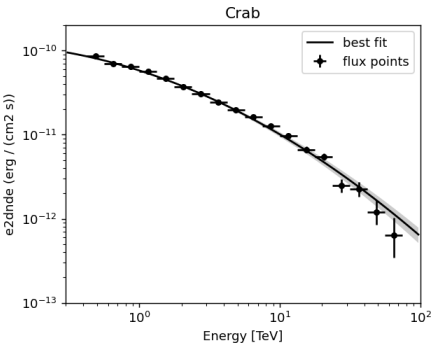

Figure 3.8: Flux points and the best-fit spectrum for the Crab dataset.

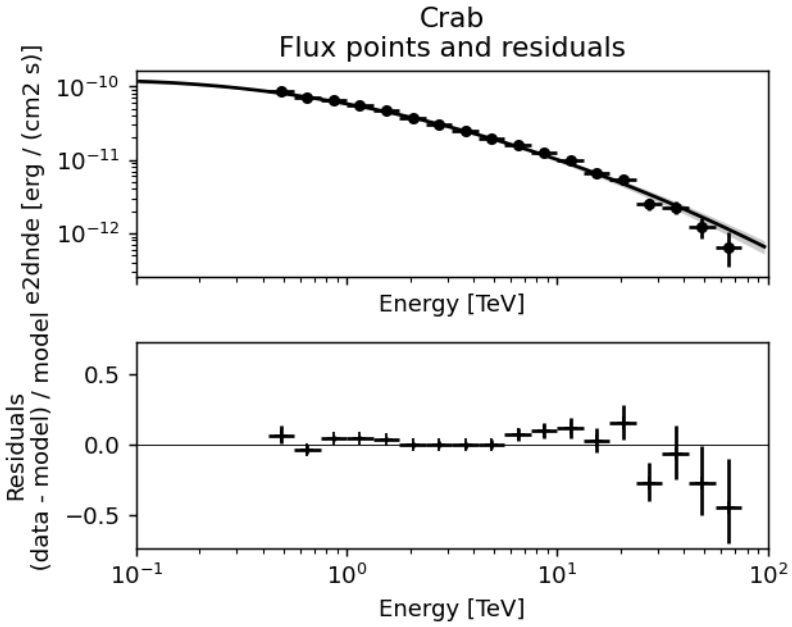

Figure 3.10: Flux points and the residuals for the best-fit Crab spectrum.

Figure 3.8 shows the flux points obtained for the stacked Crab dataset.

Inspecting the Results

A common check of the analysis quality is the significance map, especially for morphology analysis. It consists of the significance values of the mismatch between the data and the model within a circle centered at each pixel displayed in a sky map. In case of a good description, the expected skymap is a normal distribution of significances, in units of σ. Variations from the normal distribution indicate miss modeling of the data. An example of significance sky map for a Crab analysis is shown in figure 3.9.

The quality control of a spectrum analysis can be carried by the residuals from the flux points, which is the difference between the flux points and the best fit. The example of residuals from the flux points for the Crab dataset is shown in figure 3.10.

Besides these tests, the confidence contours are also useful to understand the correlation of the fitted parameters. The confidence contours highlight the range of values in the parameter space that could also describe the data, at a given statistical level. Figure 3.11 shows an example of confidence contours for ϕ_0, α and β parameters from the Crab analysis. The best-fit value is marked as a black cross and the contours represent the statistical 1, 2, and 3 σ levels.

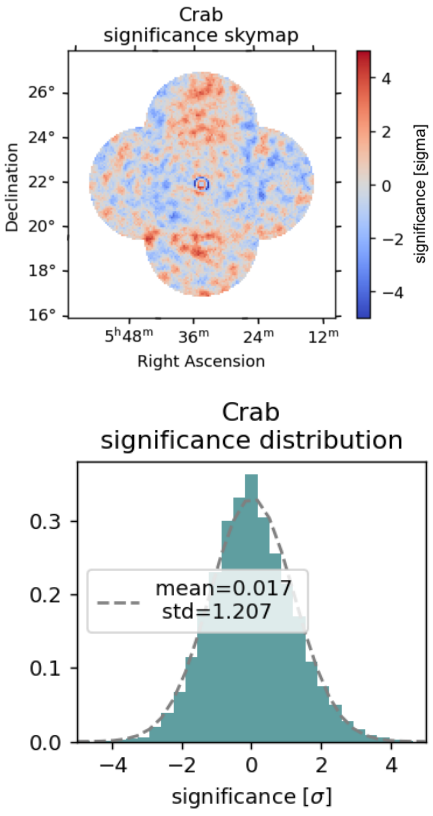

Figure 3.9: Significance sky map for the example Crab stacked dataset is shown in the upper plot. The distribution of the significance values from the skymap is shown in the bottom plot together with a normal distribution fit, the expected in the case of a perfect model.

Table 3.3: The axes and the bin edges define the systematic error bins for this analysis.

axis	bin values
zenith [deg]	[0, 15, 25, 35, 42.5, 47.5, 52.5, 60]
energy	8 bins/decade
HESS eras	H.E.S.S. I and H.E.S.S. II
per run	–

3.2 Systematic Errors

There is no unique recipe for estimating systematic errors and one of the big challenges in estimating systematic errors is the disentanglement from the statistical errors. While statistical errors are natural and random deviations in the data, systematic errors present a consistent trend. However, the separation between these two is challenging.

The method developed in this work uses the main parameter 'error curves', which is calculated from the parameter 'deviation curve'. The goal of this section is to introduce both parameters and the external features which influence them. The error curves contain the information for the lookup tables, which are the output of this method.

3.2.1 Definition of Error Curve

Defining the Systematic Bins

The systematic errors are calculated in different bins. The choice of bins is a compromise between available statistics and the main goals of the method. To be applicable to any dataset, the systematic error is done on a run-wise basis. It is binned in energy, assuming the canonical value for a common IACT analysis, 8 bins/decade, suitable for analysis on a run-wise basis.

Additionally, the estimation is also done in zenith bins, the same as the model construction, and it is motivated by the rapid change in the IRFs with zenith, as described in section 2.3.2.

In summary, the systematic error bins are described in table 3.3, assuming that the systematic error has the same behavior within one systematic error bin.

It is worth noting that these bin edges are not exclusive and they can be adapted according to different versions of the template model and/or different goals.

From now on, the systematic bin is defined based on zenith and H.E.S.S. era axes, one example is H.E.S.S.I, zenith angle between 47.5-52.5°.

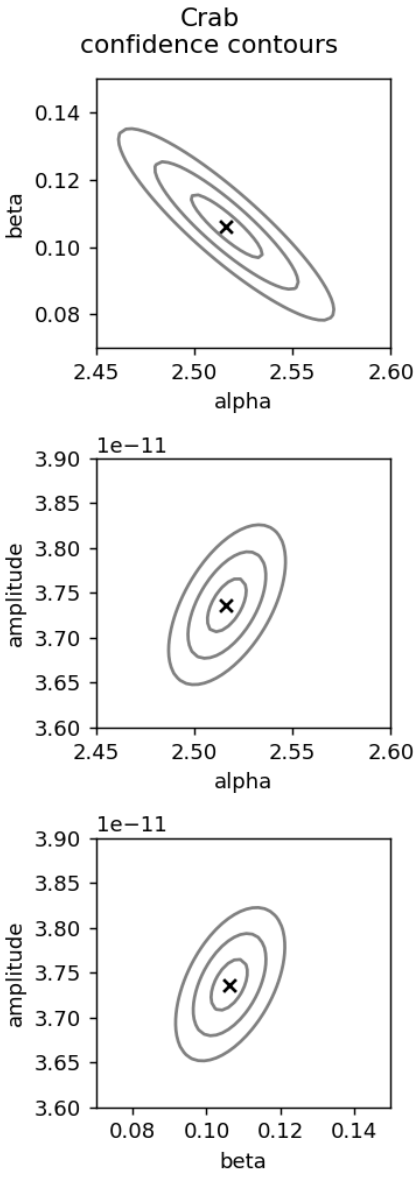

Figure 3.11: Confidence contour for the Crab stacked dataset. The curves from the smallest to the biggest represent the 1,2 and 3 statistical σ levels. The upper plot shows the confidence contours for α and $beta$, the middle plot for α and ϕ_0 and the bottom plot presents for β and ϕ_0. The best-fit value is marked as a black cross.

Table 3.4: Selection criteria of runs used in the systematic error studies

parameter	value
number of telescopes	4
zenith pointing	$\leq 60°$
event counts	1500
galactic latitude	|galactic latitude| >5 deg
galactic longitude	|galactic longitude| >60 deg

Data Selection

A summary of the run selection cuts is described in table 3.4.

The number of telescopes and the zenith angle restrictions are defined based on the 3D background model, which is constructed for runs with four telescopes and zenith angles below 60 deg. The event counts limitation arises due to bad fitting of runs with fewer counts due to the lack of statistics. The restriction of the galactic latitude and longitude is motivated due to contamination of the galactic plane.

Each run follows the analysis pipeline described in the previous section, with the last step being the pre-fit of the background.

Definition of Deviation Curve

The parameter deviation curve is defined per run, per energy bin i. For convenience, two different units are considered: units of statistical standard deviation, [std], and units of % of background events, [% of bkg]. While the first one is less sensitive to the available statistics and therefore better for understanding the systematic errors on a run-wise basis, the second one is practical for the estimation of the error in a dataset.

The deviation curves for these two units are defined as the following:

$$\text{deviation}_i\ [\text{std}] = \frac{\text{data}_i - \text{model}_i}{\sqrt{\text{model}_i}} \tag{3.3}$$

$$\text{deviation}_i[\ \%\ \text{of bkg}] = \frac{\text{data}_i - \text{model}_i}{\text{model}_i} \tag{3.4}$$

where data_i is the total number of events in the bin i and model_i is the total number of expected events due to background (after the pre-fit procedure), both integrated over source-free regions.

Figure 3.12 shows a compilation of the procedure for a dataset of an example run. It shows from the background pre-fit, the derivation of the deviation curve. The deviation curve comprises the deviation of data and the model of a run-in energy axis in source-free regions. It includes systematic and statistical errors.

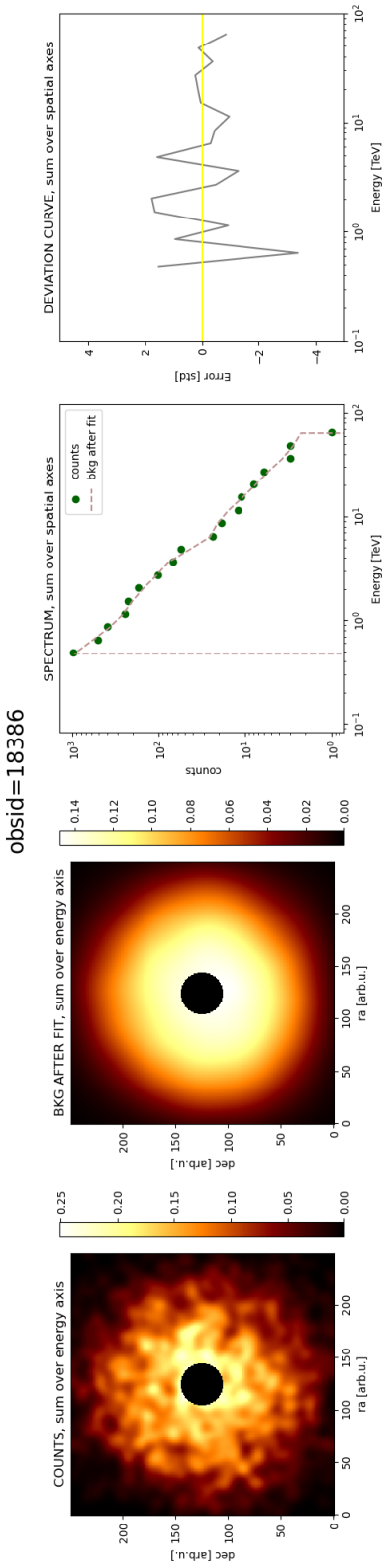

Figure 3.12: Dataset for the example run, obs_id: 80170. From left to right, the first two plots show skymaps, integrated over the energy axis, and the black disc masks the gamma-ray source. The skymap on the left presents the measured events while the one on the right presents the expected background events after the pre-fit procedure. The third and fourth plots present the data in function of energy, integrated over the source-free region. The third plot shows the measured events as green dots and the background estimation as a dashed salmon curve. Finally, the fourth plot shows the deviation curve, calculated following equation 3.3.

From Deviation Curve to Error curve

In one deviation curve, statistical and systematic errors are both present. To isolate the systematic errors, the number of deviation curves, N, must be increased. The averaging of the deviation curves from one systematic bin (defined in 3.2.1) results in the error curve.

While the deviation curve is the deviation per run, which also includes the statistical fluctuation, the error curve is defined per systematic bin as the average of the deviation curves, emphasizing the systematic errors.

Figure 3.13 shows the example of one deviation curve, on the left plot, and on the right plot the combination of several deviation curves for the same systematic bin. The black curve is the error curve, the average of deviation curves. In both plots, the yellow line is set at zero as a reference.

Considering the same energy bin, the distribution of values from different deviation curves must follow a normal distribution, in case of only statistical fluctuations. A shift of the mean from zero, the expected from a normal distribution, is defined in this work as the level of the systematic error in units of std.

Figure 3.14 illustrates the above-described situation for the deviation curves presented on the right-hand side of figure 3.13. The different colors identify specific energy bins, in which the distribution is shown in the lower row plots. The distribution in each energy bin is unique. The number of runs in each energy bin is constant, except for the first one. In this case, it indicates that for this systematic bin, the runs have different low energy thresholds.

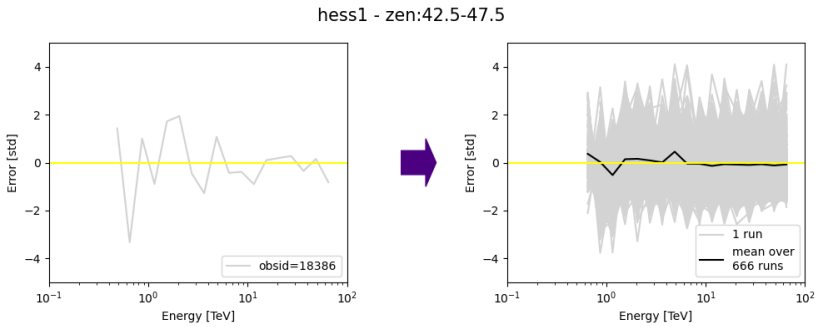

Figure 3.13: On the left plot it is shown the deviation curve of the example run 18386. On the right plot, it is shown all the deviation curves for this systematic (H.E.S.S. I and zenith bin 42.5-47.5°) bin and the average of them, is shown as the black curve, the error curve.

For this method, the systematic error level is characterized by a signal, positive or negative, and the strength is defined by the mean of the distribution. For instance, for the energy bin 1-1.33 TeV is systematic error level is -0.52 std, while for the energy bin of 4.22-5.62 TeV it is 0.46 std. For energies higher than 5 TeV, the systematic error decreases.

Besides the level of the systematic error, defined as the mean of the distribution, its spread is also relevant to indicate

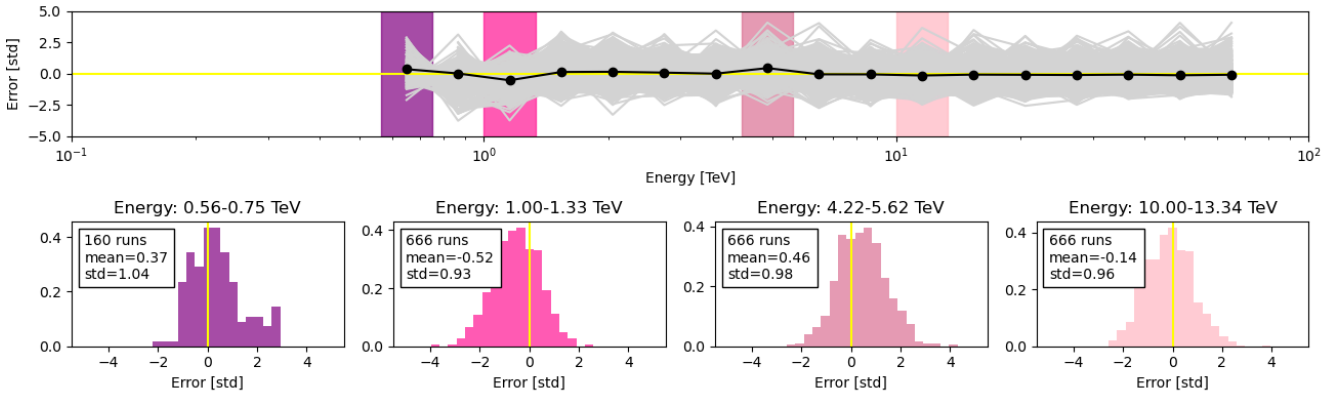

Figure 3.14: This figure shows the distribution of the deviation per energy bin for the systematic bin H.E.S.S. I, zenith bin [47.5-52.5]°. The upper plot shows the deviation and the error curve for this systematic bin. The colors identify specific energy bins, and for these, the distribution of the deviation is shown in the lower plots.

the reliability of the level estimation. A large spread would indicate the case introduced in the bottom right plot on figure 3.1. Thus, although the error curves are defined from the mean, the estimation is more precise and reliable when the spread is smaller.

The estimated level of systematic error still contains a small fraction of statistical fluctuations, due to the limitation of a finite number of runs. However, since the statistical error follows Poisson statistics, the expected uncertainty is known, $\sqrt{N}$.

For systematic bins with less than 10 runs available for estimation, the separation of systematic and statistical errors is challenging due to the lack of statistics. Thus, if the systematic error value for these cases is within 3 σ statistical fluctuations, the systematic error is defined as 0.

In the case of a few runs in a systematic bin, if the level of systematic error is within 3 σ statistical fluctuation, the systematic error is defined as 0, due to the impossibility to separate the different errors.

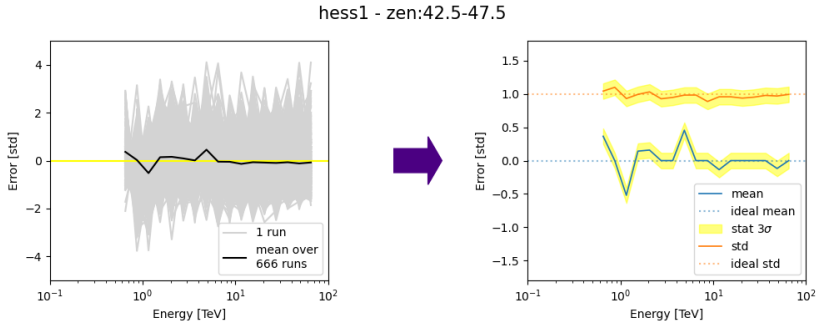

Figure 3.15: Transition from deviation curves to error curves. The average of the deviation curves presented in black on the left-hand plot is the blue curve on the right-hand plot. The 3 σ statistical fluctuation, expected from the finite number of runs, is shown as the yellow bands, and the spread of the deviation is shown as the orange curve on the right-hand plot. This example considers the systematic bin H.E.S.S. I zenith bin [47.5-52.5]°.

Figure 3.15 presents the transition of the deviation curves to the final error curve. The main output is the error curve, shown in blue. The spread of the distribution, shown as an

orange curve, indicates the robustness of the error curve. The 3 σ statistical fluctuation due to the available number of runs in the systematic bin is shown as yellow bands. This plot compiles the systematic error level for one systematic bin.

The systematic errors for all systematic bins from H.E.S.S. I phase is shown in figure 3.16. The similarities and differences in the behavior across different systematic bins assist in tracking the origin of these errors.

The visible trends observed are: (i) the majority of the systematic bins present higher amplitude in the low energy range, (ii) in the low energy range, the low zenith bins present higher amplitude, with the first and second energy bins presenting opposite signs, (iii) in all zenith bins, there is a consistent bump at 5 TeV. Additionally, the high amplitude of the orange curves points to different behaviors of the error level across runs within the same bin. Interpretation of these patterns is discussed in the section 3.3.

Up to this point, the method of estimating the systematic error in each systematic bin is introduced. In this procedure, the statistical limitation is dealt with by averaging the deviation curves, and therefore the error curves highlight only the systematic errors.

3.2.2 The Role of the Analysis Method in the Context of Systematic Errors

The analysis method translates the causes of systematic errors into observable features in the analysis. In this process, the systematic error can potentially be spread to energies/bins where initially no systematic error is expected.

This section aims to explain how the pre-fit of the background model and the choice of the low energy threshold bear the systematic errors in the analysis.

Pre-fit of the background model The pre-fit procedure is a step to adjust the background model to the data. It parameterizes the model in normalization and tilt of a power-law spectrum. These two free parameters cover the entire energy range and correlate the energy bins. In case of no systematic errors, the expected values for normalization and tilt are 1 and 0, respectively.

In case of systematic errors present in the data, the pre-fit procedure attempts to compensate for the mismatch caused by the systematic errors with the free parameters, normalization and tilt.

For instance, consider the case where there is systematic error only in the energy bin i, the measured data in this bin is d_i, background model m_i, and A as the free parameter normalization of the fitting.

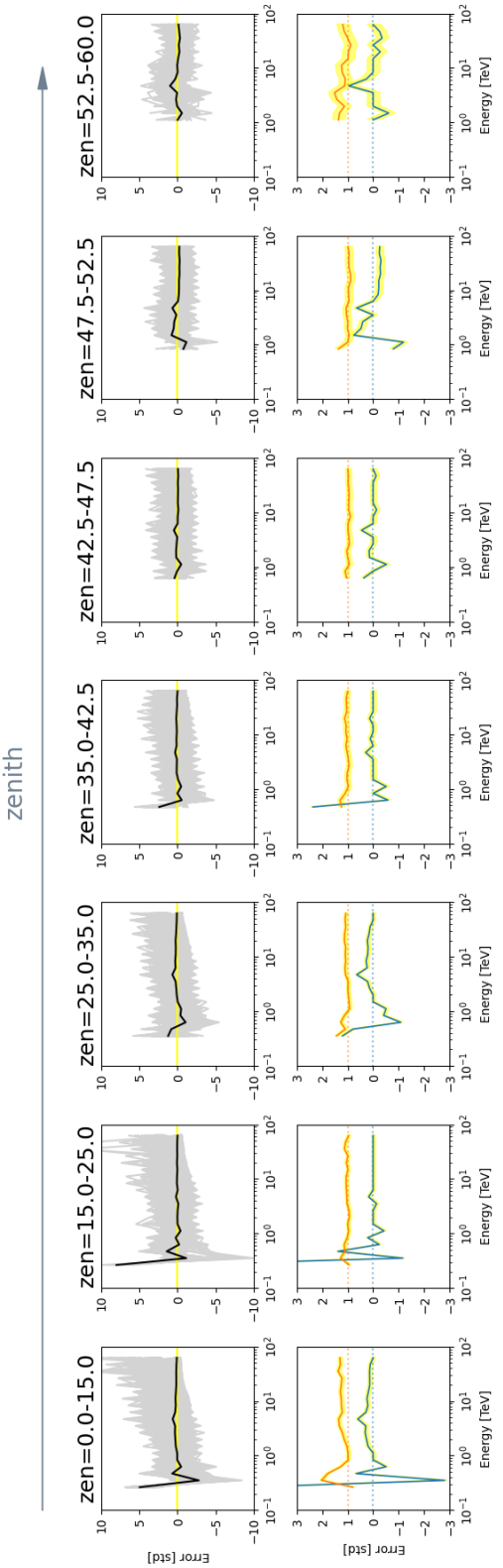

Figure 3.16: The systematic error estimation for all zenith bins in H.E.S.S. 1 phase. The upper row shows in gray lines all deviation curves used in the estimation and in black the average of them. Note that the density of the curves is not visible in the plot, thus curves with larger spread are observed as the same intensity as many overlapping curves. The bottom row shows the error curves, as blue lines, and their respective spread, as orange lines. The statistical fluctuation due to the number of runs in the bin is shown as the yellow band. Each column corresponds to one zenith bin. The plots are in units of error [std] and in function of energy.

$$d_i = A \cdot (m_i + \sigma_{\text{sys}}) \tag{3.5}$$

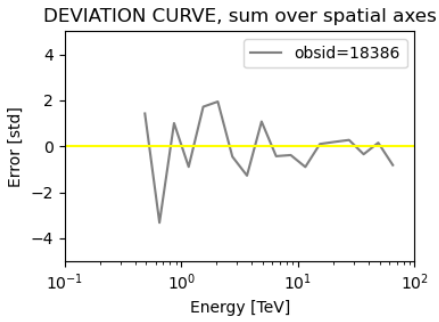

Figure 3.17: Deviation curve of the example run 18386. The first and the second energy bin presents opposite signs of deviation.

$$d_{i+1} = A \cdot (m_{i+1}) \tag{3.6}$$

The normalization A attempts to compensate for σ_{sys} in the bin i, resulting in an erroneous value of A. Since A is the same for the entire energy range, it biases the energy bin $i+1$, resulting in an opposite sign in the deviation.

Consequently, the systematic error that was initially only present in one bin i is now propagated to $i+1$. The most visible effect is in the neighboring bin, resulting in a deviation with the opposite sign. It means that in the deviation curve, if the first energy bin presents a positive deviation, the second bin presents an opposite sign deviation, as shown in the example run 18386 in figure 3.17.

A basic assumption in this work is that within a systematic bin, the shift caused by the systematic error is the same. Thus within the same systematic bin, the deviation curves shift in the same direction. This effect is indeed observed in figure 3.16, especially for the low zenith bins, where the deviation in the low energy range is more prominent. The deviation curves present the same direction of the shift for the first energy bin, positive, and opposite sign for the second energy bin. While in higher zenith bins, these features vanished, confirming also the different nature of the systematic error per zenith bin.

Low energy threshold From figure 3.16, it is observed that the higher systematic error occurs at low energies, and therefore the correct selection of the low energy threshold is crucial in the control of the systematic errors.

By selecting a very low energy threshold, which includes systematic errors, the error is propagated to other energy bins due to the pre-fit procedure, as explained in the previous section. However, an extremely high threshold leads to statistics reduction and loss of information in the overlapping energy range with satellite instruments.

There are different approaches to define the energy threshold for the analysis, as described in the definition of safe range in section 3.1.2. This work defines as conservative scenario as the highest threshold from the different approaches; and the liberal scenario, as the lowest energy threshold, which is defined by the effective area.

Figure 3.18 shows the spectrum of an example run considering different low-energy thresholds and their respective values of chi2/dof. The conservative threshold presents a chi2/dof value of 13,588/16 while the liberal, which includes more statistics, presents a chi2/dof of 26.64/dof.

It is worth highlighting that the aim of this work is to introduce the consequences of the systematic error, rather than provide a universal decision of low energy threshold definition.

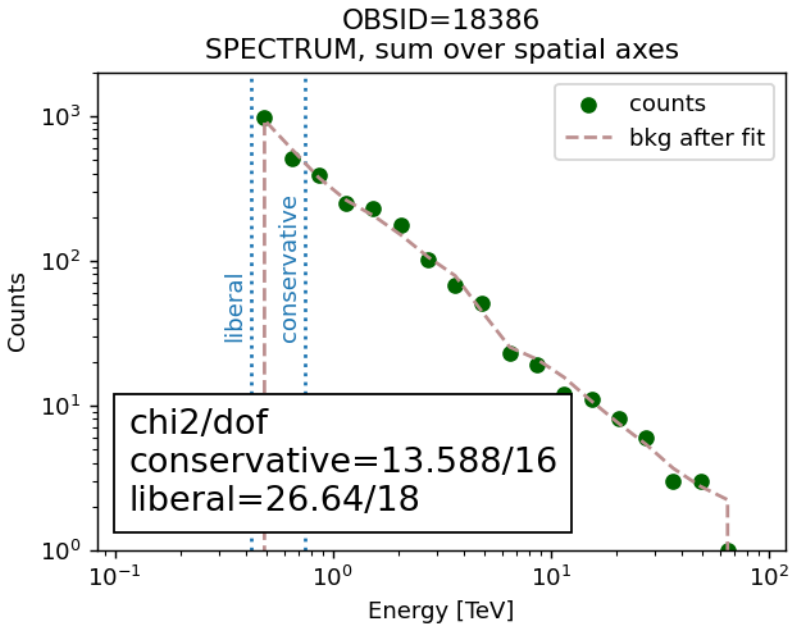

Figure 3.18: Spectrum of counts for example run 18386 shown as green points, and the background model, dashes salmon curve, after pre-fit, assuming two different definitions of low energy threshold: the conservative and liberal scenarios.

3.3 Systematic Error - Causes

In this section, the causes of the systematic errors using the background model version v_05 are presented. The first one, here denominated as 'muon efficiency', is responsible for the high deviation in the low energy in the error curves. The second one, named here as 'BDT edges', is responsible for the high systematic at 5 TeV. While the first one is a systematic error arising from the template model construction, the second is regarding steps before the model construction, which still influences the 3D analysis.

It is worth noting that these two different origins are the most visible ones in the error curves. However, other causes for systematic error at a lower level, are also feasible, although not addressed in this work.

3.3.1 The Muon Efficiency Parameter

The muon efficiency parameter condenses the conditions of the atmosphere and the instrument. Each run has a value of muon efficiency which is defined as the average of the muon efficiency of each telescope. The value of this parameter is defined based on the light detected from the muon ring patterns[†]. Since the light and the radius of the muon ring are correlated, by measuring the size of the ring, the expected light from this signal can be compared to the light measured.

[†] As shown in figure 2.22.

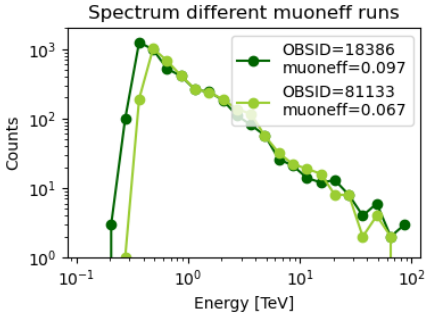

Figure 3.19: The spectrum of two runs (OBSIDs=20699 and 40132) with different muon efficiency values, 0.097 and 0.067, but with similar external conditions, such as zenith pointing direction and observed source.

This ratio of measured and expected light is the base for the value of the muon efficiency parameter.

The muon efficiency parameter directly influences the effective area of a run at the low energies. The high value of muon efficiency indicates a high capability to detect faint signals, meaning events of lower energies, which consequently increases the effective area at low energies. This change in the effective area has consequences in the spectral and spatial distribution of the measured data.

Figure 3.19 shows the spectrum comparison in the spectrum for two runs with different muon efficiency values. One striking difference is that the rapid increase of the spectrum occurs at different energies: lower energy for the run with a higher muon efficiency value. One consequence of the different effective areas for these runs is that at 0.4 TeV, while run 18386 reaches the peak of the spectrum, run 81133 presents a considerably lower event detection. As the energy increases, the two runs tend to converge to a similar behavior.

Figure 3.20 shows a comparison of the spatial distribution for different energy bins of two runs and the background model. From the first column, the lowest energy, it is noticeable that the run with high muon efficiency (upper left plot) presents a more radially symmetric distribution than the run with low muon efficiency (lower left plot). Additionally, the intensity of both plots is different, observed by the different scales. This effect is also a consequence of the differences in the effective area of these runs. Despite such differences, the two runs are described by the same background model, shown in the middle plot of the first column.

For the following energy bins the spatial distribution of both runs tends to a radial distribution, converging to the same behavior.

While each run presents spatial asymmetry at a specific energy, which depends on the muon efficiency, in the template model the asymmetry occurs at the energy, at which this asymmetric behavior occurs for the majority of runs. As consequence, runs with outlier values of muon efficiency are not well represented by the 3D background model.

The issue in the asymmetry results in a spatial pattern in the residuals as shown in figure 3.21. For this energy bin, while the data presents a radial symmetry the model presents an asymmetric distribution, leading to the patterns in the residual skymap.

In summary, runs with high muon efficiency have a modified effective area, compared to the average, which leads to the detection of more events at lower energies, shifting the spectrum and the asymmetric spatial distribution to lower energies. As a consequence, the model poorly describes these runs since it is constructed by averaging and does not consider the muon efficiency parameter in the model construction. This

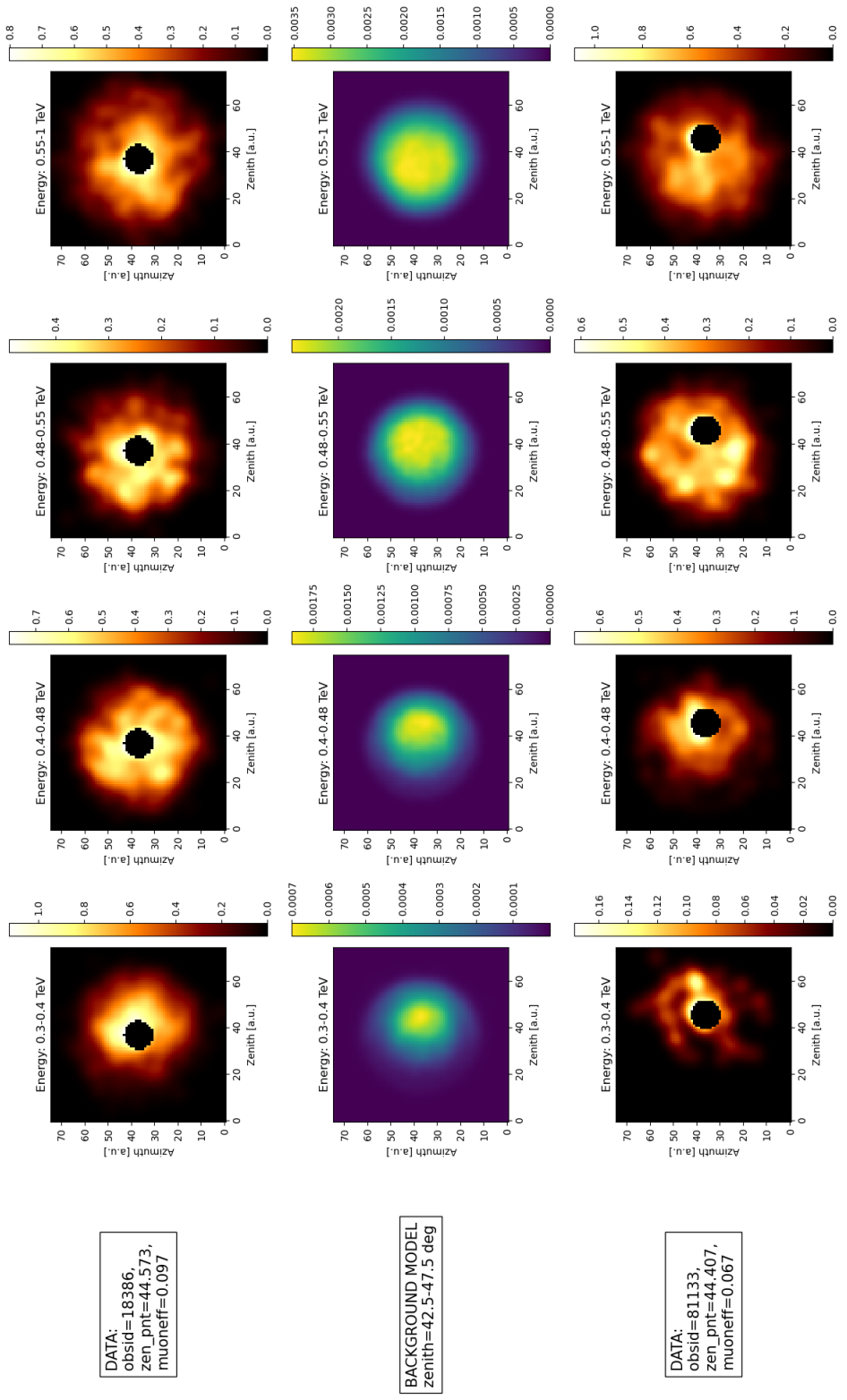

Figure 3.20: Spatial distribution in skymaps of the run's measured data (upper and bottom rows), and in the middle row is the spatial distribution of the background model. Each column presents different energy bins.

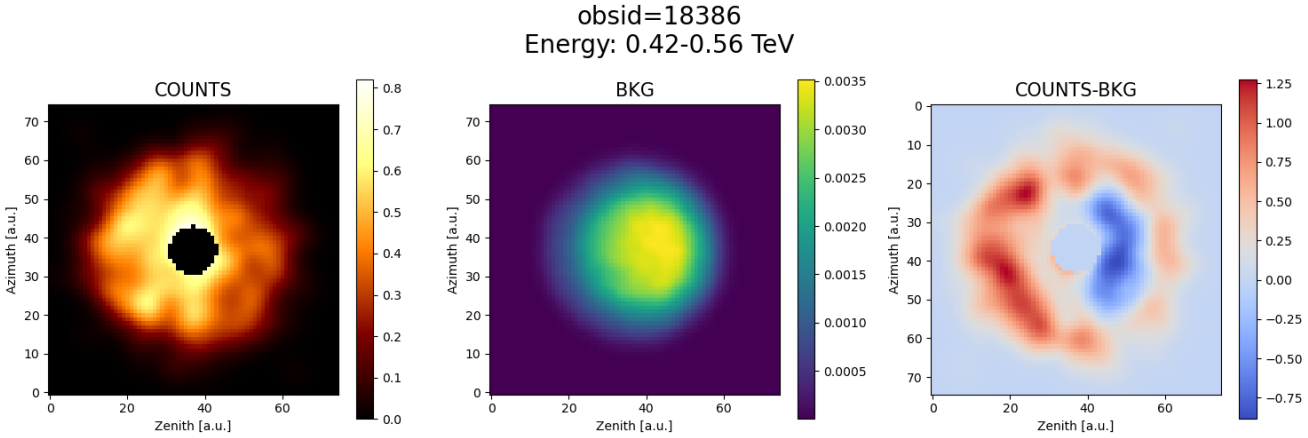

Figure 3.21: For the run example 18386, in the energy bin of 0.42-0.56 TeV, it is shown sky maps for the observed data, left plot, the background expectation, middle plot, and the difference between them, on the right plot. All the plots are in units of counts.

error is propagated to the neighboring bins due to the pre-fit procedure described in the previous section.

The Alternative Model

The problem of asymmetry is only present in the low energy range. Thus, by increasing the low energy threshold of the analysis, systematic errors are excluded and the model describes the data well, at the cost of excluding the low energy range. The key point of an alternative model is to correctly describe the low energy range to include data previously excluded in the analysis.

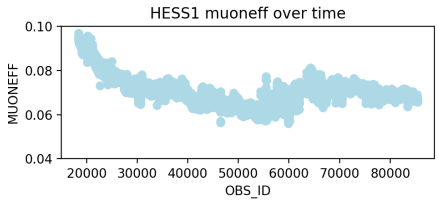

Figure 3.22: Muon efficiency value with time for runs in H.E.S.S. I.

To properly describe the runs with high muon efficiency, an alternative version of the model is built by including bins in the muon efficiency parameter. The distribution of muon efficiency for H.E.S.S. I era is shown in figure 3.22 in function of observation ID, which is equivalent to time. The highest values of muon efficiency, ~ 0.09, occur at the beginning of the H.E.S.S. lifetime, when the reflectivity of the mirrors was high, leading to detection of fainter events.

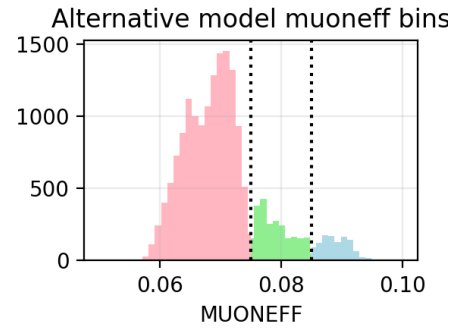

Figure 3.23: Muon efficiency distribution for H.E.S.S. I, the different colors indicates the different muon efficiency bin.

The binning of this parameter, in a similar manner as the other axes, is a compromise between available statistics, runs, and a good description of the features. The bin edges of the muon efficiency axis are presented in table 3.5. The selection of the bin edges considers a minimum of 20 hours for exposure for the most popular zenith bins (ranging from 35°-52.5°). Figure 3.23 shows the histogram of muon efficiency with each color corresponding to a different muon efficiency bin.

Table 3.5: Bins edges for muon efficiency parameter.

model	muon efficiency
muon efficiency_hi	muon efficiency ≥ 0.085
muon efficiency_med	$0.075 \leq$ muon efficiency ≤ 0.085
muon efficiency_low	muon efficiency ≤ 0.075

Figure 3.24 compares the official and the alternative model for the high muon efficiency bin for the energy range of 0.42-0.5 TeV. The first two skymaps have the same color scale. For this energy bin, while the official model still presents asymmetric distribution, the alternative model is radially symmetric; this feature is evidenced in the third plot, which shows the difference between the previous two skymaps. The last plot shows that the correction of the alternative model is clear in the low energy range, as it is built to be; as the energy increases the behavior of the two models converges.

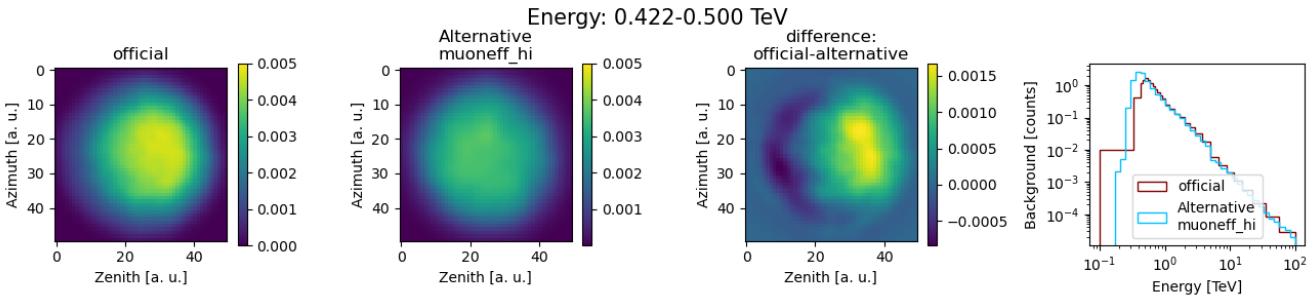

Figure 3.24: From left to right, the first three plots show skymaps in az-alt coordinates for a comparison between the official and the alternative model for the high muon efficiency bin for the energy range of 0.42-0.5 TeV[a]. The first plot the expected background events from the official model, the second plot, the expected background events from the alternative model, and the third plot shows the difference between the two previous plots. The last plot, on the extreme right, presents the spectrum of the model, in the energy bins of the model construction.

[a] This energy bin chosen to outstand the difference between the official and the alternative model for this systematic bin

The alternative model does not influence the runs similar to the average runs, but rather the outlier runs with different values of muon efficiency. For these runs, the deviation curves are presented in figure 3.25 considering different model versions (official/alternative) and different low energy thresholds (conservative/liberal).

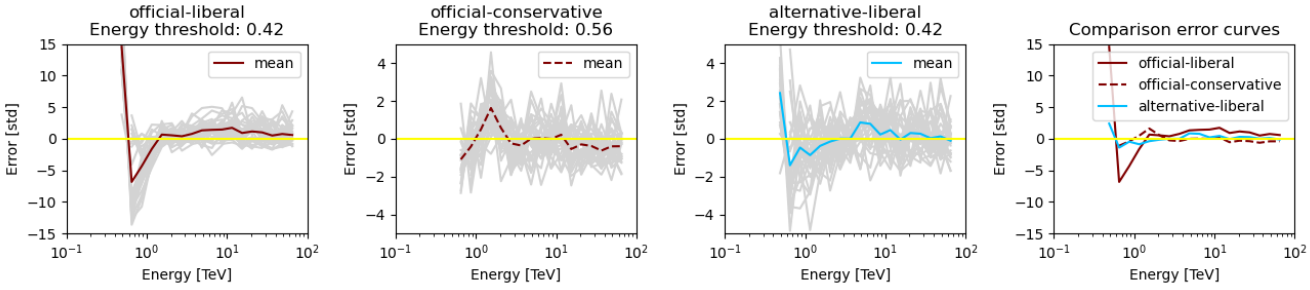

Figure 3.25: The first plot is the official model considering a liberal low energy threshold, the second plot is the official model considering a conservative low energy threshold and the third plot considers the alternative model with the liberal threshold. Note the first plot has a different scale than the following two plots. The gray lines represent the deviation curve of each outlier run and the colored line is the average of the deviation curves. The yellow line is set to zero for reference. The fourth plot is a combination of the average deviation curves of the previous cases.

From the first case, considering the liberal energy threshold, the official model does not represent well the data, showing significant levels of error curve (the mean curve) at low energies, higher than 10 [std]. The mean is strongly influenced by the fewer curves presenting a larger deviation. One alternative to this problem is to increase the low energy threshold, which is shown in the second case, considering a conservative low energy threshold. For the second plot, the level of the error curve is much smaller showing the goodness of the

official model in at the low energies. The third plot considers the liberal energy threshold and the error curve is at a similar level to the official model with a conservative threshold. The widening of the energy range with lower levels of the error curve demonstrates the improvement of the alternative model.

3.3.2 Boosted Decision Trees Edges

The BDT method is used in H.E.S.S. for the classification of events as hadrons or gamma rays. This step occurs at the very beginning of the analysis chain, and the events that survive the BDT selection are the so-called gamma-like events. The gamma-like events are the input for the background model construction.

The BDT procedure is performed in energy bins and it presents a discontinuity in the gamma-like spectrum at the bin edges, due to the inherent features of the procedure as described in [104]. As a consequence, issues arise also for the background model as described and corrected in [104].

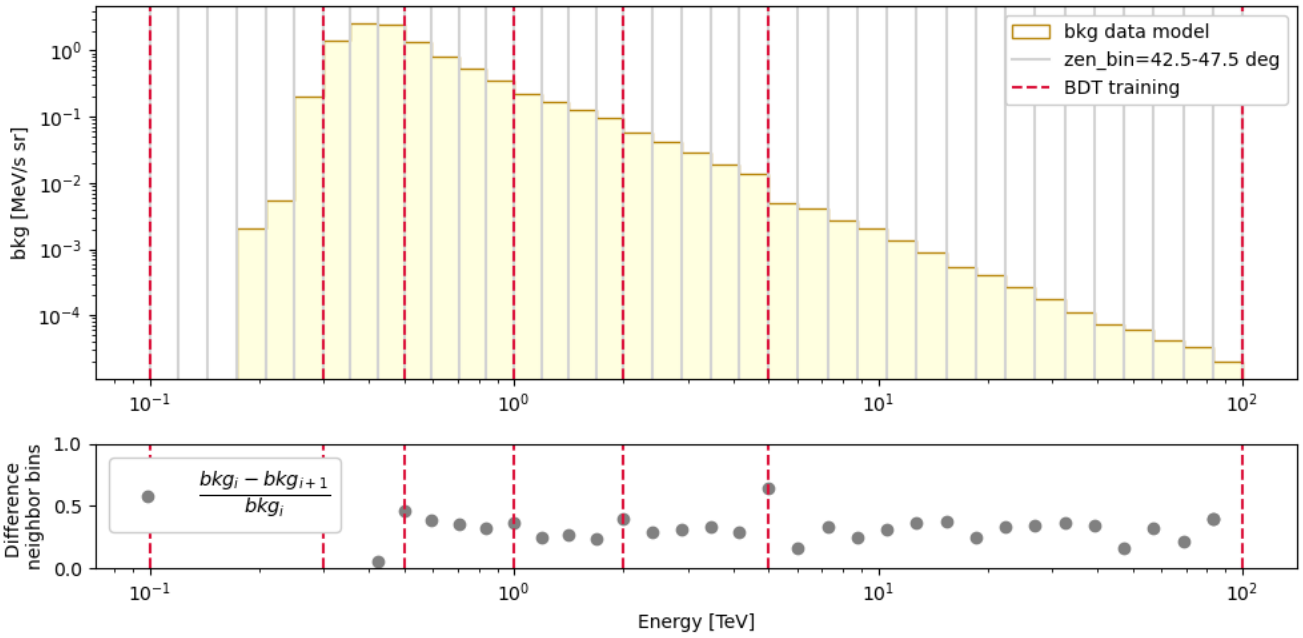

Figure 3.26: For the model bin 42.5-47.5 deg, the background flux is shown in yellow, with energy bins of the model construction, gray vertical lines. The BDT edges are marked as dashed red lines. The bottom plot shows the relative difference in the background flux between the current and the next energy bin.

Figure 3.26 shows the discontinuity in the background model at BDT edges, as high values of the relative difference of the background flux between neighboring bins. The discontinuity in the background flux at the BDT edges is a heritage from the discontinuity in the gamma-like spectrum from the BDT method. Although this problem is corrected in the background model construction, when the model is applied in the framework of the 3D analysis, due to the different energy bins used, this issue arises again as a systematic error.

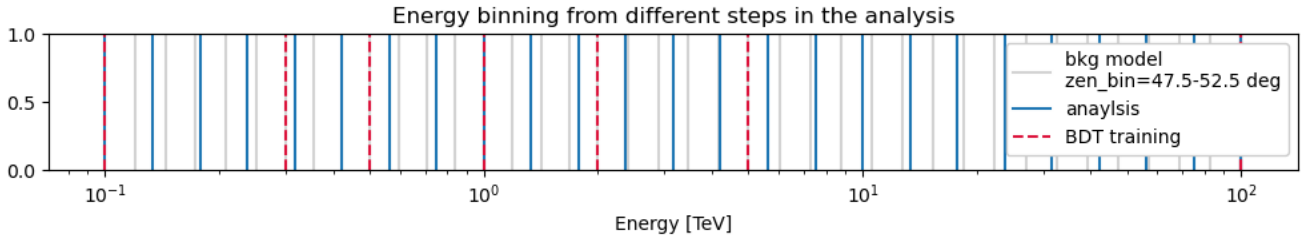

Figure 3.27: The different types of energy bins relevant for the analysis: BDT edges, dashed red lines, from the model construction, solid gray line, and from the analysis, solid blue line.

The origin of this systematic error involves three different types of energy bins, illustrated in figure 3.27. The bin edges from the BDT method are shown in table 3.1 and it is the largest among the three types. The bin edges for the model construction are described in [104], it is the smallest among the three types and some coincide with the BDT edges. The energy bins for analysis are described in table 3.3.

Within gammapy, the estimation of the background within an analysis bin is done by interpolating the values of the model bins. This approach works perfectly within one BDT bin since the model spectrum is continuous. However, at analysis bins enclosing a BDT edge, which translates into a gap in the mode spectrum, the interpolation method is insufficient to describe properly the complexity of the model.

This limitation causes systematic errors observed at BDT edges. For energies below 5 TeV, the gap in the spectrum is not as significant; however, it stands out at 5 TeV, being observed as a consistent bump at this energy in all systematic bins.

Generally, this systematic error does not influence the spectrum of the source of interest since the fitting procedure considers the whole energy spectrum, vanishing small contributions such as this issue. However, effects might be observed in the flux points, since it is done per energy bin.

It is also important to highlight that this is a specific feature of the configuration std_zeta_fullEnclosure in H.E.S.S. and not observed in other configurations that do not use the BDT method. Nevertheless, this example shows that steps before the model construction and analysis can appear as systematic errors.

3.4 Quantitative Estimation of Systematic Error

This section summarizes the systematic error calculated previously, highlighting the features together with its causes. From the error estimation, lookup tables are built and the method of using them to estimate the systematic error of a stacked dataset is presented.

All the material, such as scripts and files with the systematic level, are available online on github[‡] and ready to be used.

3.4.1 Estimated Error per Run

Figure 3.28 shows the compilation of the systematic error curves for the alternative background model, for each systematic bin in H.E.S.S. I phase. In the following, the features observed in figure 3.28 is described, along with it's cause:

- Overall higher level of systematic error is present at low energies caused by the radial asymmetry in spatial distribution at low energies.
- A trend of higher level systematic error for high muoneff bins. The counts spectrum of runs with high muoneff varies substantially in low energies, which is challenging for the model to correctly describe it; nevertheless, that is the best description so far.
- Bump at 5 TeV, caused by the BDT edges.
- For low muoneff bins the systematic error is lower, indicating the runs are more similar to the average, equivalent to the model.
- Overall the low zenith bins present higher systematic errors than the other bins since low zenith observations allow lower energies detection.
- For the high zenith bins, the spread (orange curve) is higher in the low energy range compared to the low zenith bins. The large spread indicates the systematic error behaves differently for the runs within this bin and cannot be parametrized as one single cause.
- Wiggles at the beginning of the energy range, showing opposite signs pattern. This is a consequence of the propagation of systematic errors into neighboring bins.
- The available statistics for the estimation must also be considered, represented by the yellow bar. The zenith bin 42.5-47.5° concentrates more runs, shown by the smallest yellow band, and therefore the estimation is the most precise, while the zenith bin 0-15 for the high muoneff bin the least number of runs is available, shown as the largest yellow band, and therefore less accurate.

The level of the systematic error estimation indicated as the blue curves are the entry values for the lookup tables. One example of the lookup table is shown in figure 3.29, for the systematic bin: H.E.S.S. I, low muoneff bin (lowest row from figure 3.28). The error curve values are shown in blue in figure 3.28 are presented in the lookup table in the color scale, for each zenith and energy bin. The orange curves from figure 3.28), which indicates the goodness of the error curves, are not included in the lookup tables. The last energy bin is not defined, since there are not enough events measured in this bin. The lookup tables for other configurations are presented in appendix A.

[‡] github for HESS systematic errors

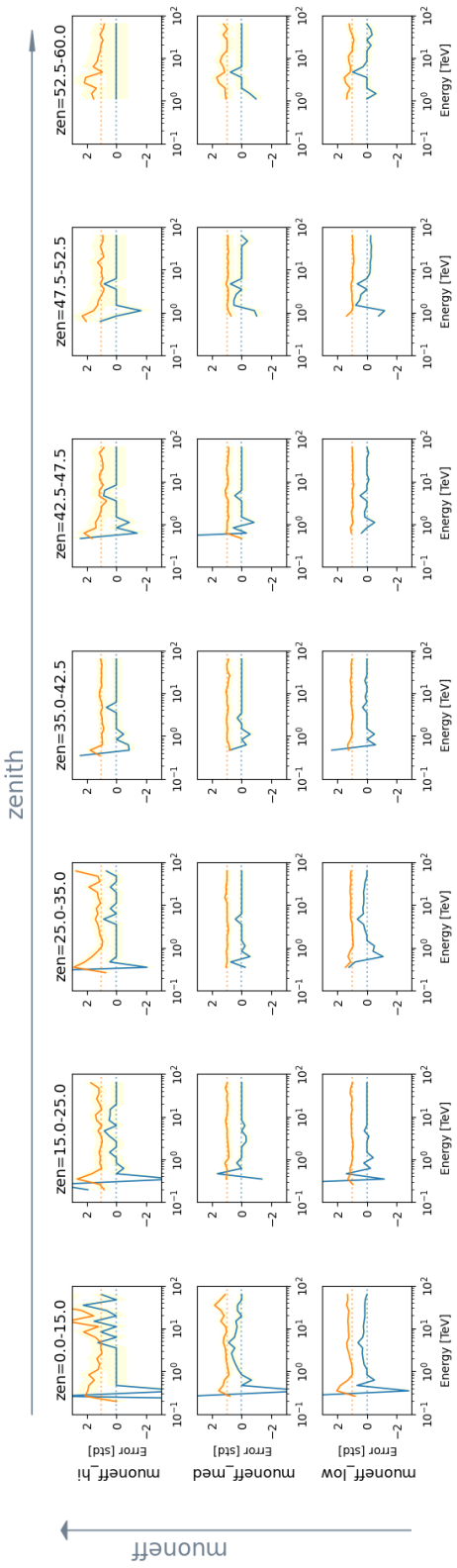

Figure 3.28: Systematic error for the alternative 3D background model for H.E.S.S. I phase. The columns indicate different zenith bins while the lines indicate different muoneff bins. The blue curve shows the level of systematic error and the orange curve shows the reliability of the estimation. The yellow band condenses information about the statistical error, based on the number of runs available for estimation. The error estimation shown here is in units of std.

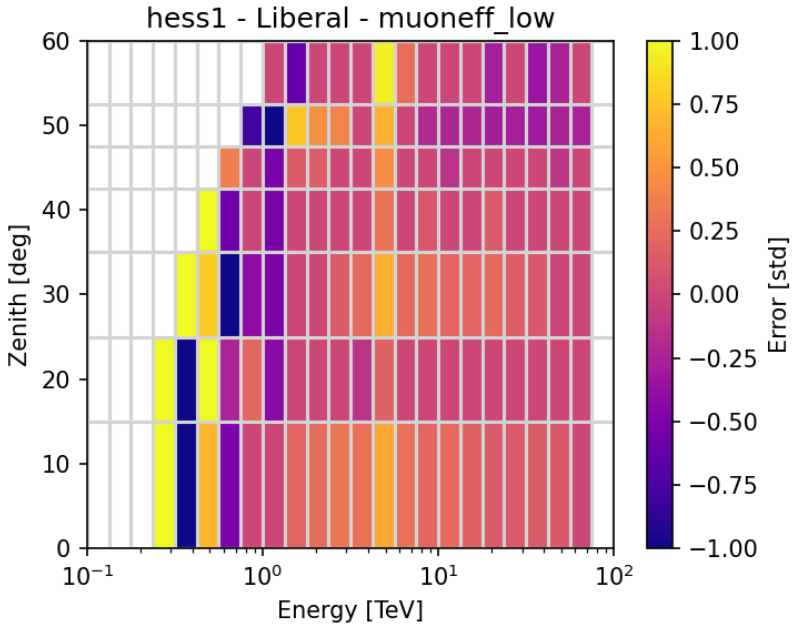

Figure 3.29: Lookup table for the systematic bin: H.E.S.S. I, low muoneff, considering liberal low energy threshold. The values are in units of std.

3.4.2 Estimated Error per Dataset

The stacked dataset is composed of several runs, and therefore the systematic error in each of the runs is also consequently added up. The contributions of the systematic error of each run can be correlated in the stacked dataset, thus a proper sum of the errors must be done.

This chapter describes a method to estimate the systematic error of a stacked dataset by using the lookup tables described previously. The output is the total background systematic error level in the analysis energy bin.

For this procedure, the error in the unit [% of background] is used. It is worth noting that when considering this unit, two different normalizations must be carefully considered: in the context of a single run dataset, $\text{model}_{\text{run},\,i}$, and for the stacked dataset $\text{model}_{\text{stacked},\,i}$; where the model is the number of background events expected, in the energy bin i. They are correlated as:

$$\text{model}_{\text{stacked},\,i} = \sum_{\text{runs}} \text{model}_{\text{run},\,i}. \tag{3.7}$$

In an energy bin i, each systematic bin k contributes proportionally to the number of runs in the bin k composing the stacked dataset. This contribution is introduced via weight $w_{k,i}$, defined as:

$$w_{k,i} = N_{k,\,\text{runs}} \cdot \frac{\text{model}_{k,\,\text{run}}}{\text{model}_{\text{stacked},i}}, \tag{3.8}$$

where $N_{k,\,\mathrm{runs}}$ is the number of runs in the systematic bin k in the stacked dataset.

Thus, the final error per energy bin is given by:

$$\sigma_{\mathrm{stacked},i}\ [\%\ \mathrm{of\ bkg}] = \sum_{\mathrm{sys\_bin}=k} w_{k,i} \cdot \sigma_{k,i}\ [\%\ \mathrm{of\ bkg}]. \quad (3.9)$$

This section uses Crab source as an example of a stacked dataset. Table 3.6 shows an overview of the number of runs in each systematic bin contributing to the stacked dataset.

Table 3.6: Overview of the number of runs for the example Crab dataset in each systematic bin

H.E.S.S. era	zenith bin	muoneff bin	N_{runs}
I	42.5°-47.5°	hi	10
		med	28
		low	47
I	47.5°-52.5°	hi	6
		med	20
		low	23
I	52.5°-60°	hi	0
		med	7
		low	7
II	42.5°-47.5°	low	35
II	47.5°-52.5°	low	22
II	52.5°-60°	low	10

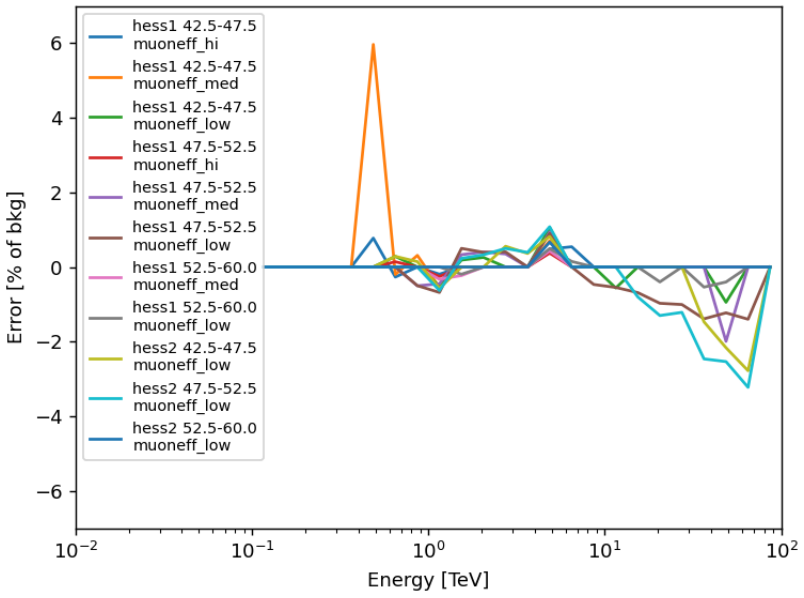

Figure 3.30: Contribution of each systematic bin, weighted by the number of runs of the Crab dataset.

Figure 3.30 shows the error contribution of each systematic bin correctly weighted by the number of runs in the stacked dataset. The first energy bin, ~ 0.6 TeV, presents an error caused by the systematic bins: H.E.S.S. I, zenith bin 42.5-47-5°, for muoneff_hi bins (blue curve) and H.E.S.S. I, zenith bin 42.5-47-5°, for muoneff_med bins (orange curve). In fact, only these two systematic bins afford a model within the safe range where the systematic error is under control.

The bump at 5 TeV is visible for all bins. The error estimation

increases (with a negative sign) towards the highest energies.

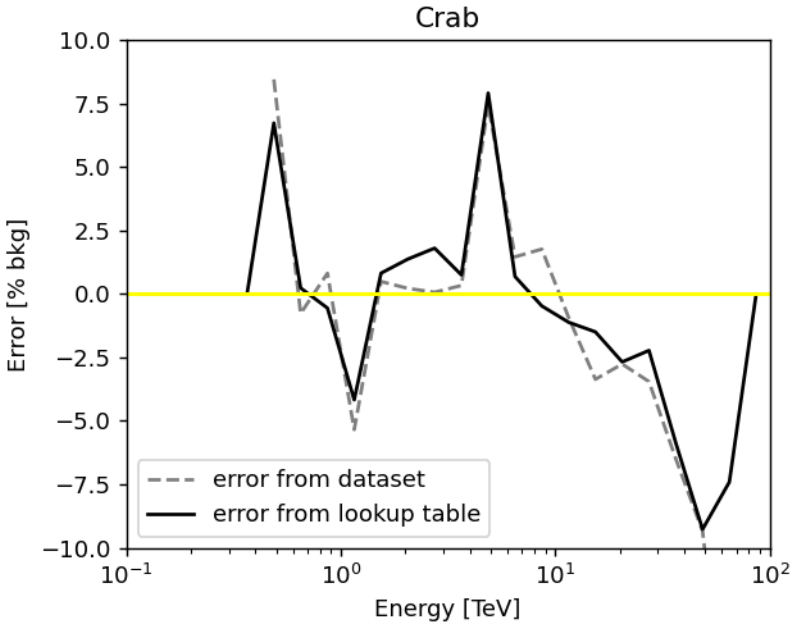

Figure 3.31: Final estimation of the systematic error for Crab stacked dataset. The error is presented per analysis energy bin, in units of % of the background events of the dataset. The solid black curve is the estimation following the method described in this work, using the built lookup tables. The dashed gray curve provides a comparison of the error using the stacked dataset itself, following equation 3.4

The sum of each weighted contribution, considering its proper sign, results in the systematic error of the stacked dataset, as shown in figure 3.31. The solid black curve presents the systematic error estimated from the procedure described above and the dashed gray curve provides a comparison of the error using the stacked dataset itself, following equation 3.4. The agreement between the two curves validates the systematic error estimation method.

It is worth noting that the estimation of the error derived from the dataset itself, the dashed gray curve, considers the systematic and statistical error in the calculation. The statistical error goes with the number of runs composing the dataset. The estimation of the error using the lookup table considers mainly systematic errors, with statistical errors being the number of runs in the entire archival data for the systematic bin k. For ranges where systematic and statistical errors cannot be disentangled, due to lack of statistics, the systematic error is defined as zero[§].

Additionally, the method using lookup tables, solid black, is independent of any feature of the stacked dataset (except the run list), while the dashed gray curve is entirely based on the stacked dataset. The independency of the error estimation on the dataset allows its applicability in a wide range of cases.

Thus, for this Crab stacked dataset, the error due to the systematics from the background model indicates that the

[§] The definition of zero value for the cases where the systematic error cannot be defined is a technical decision, since for the correction of the systematic errors, a value must be given as input.

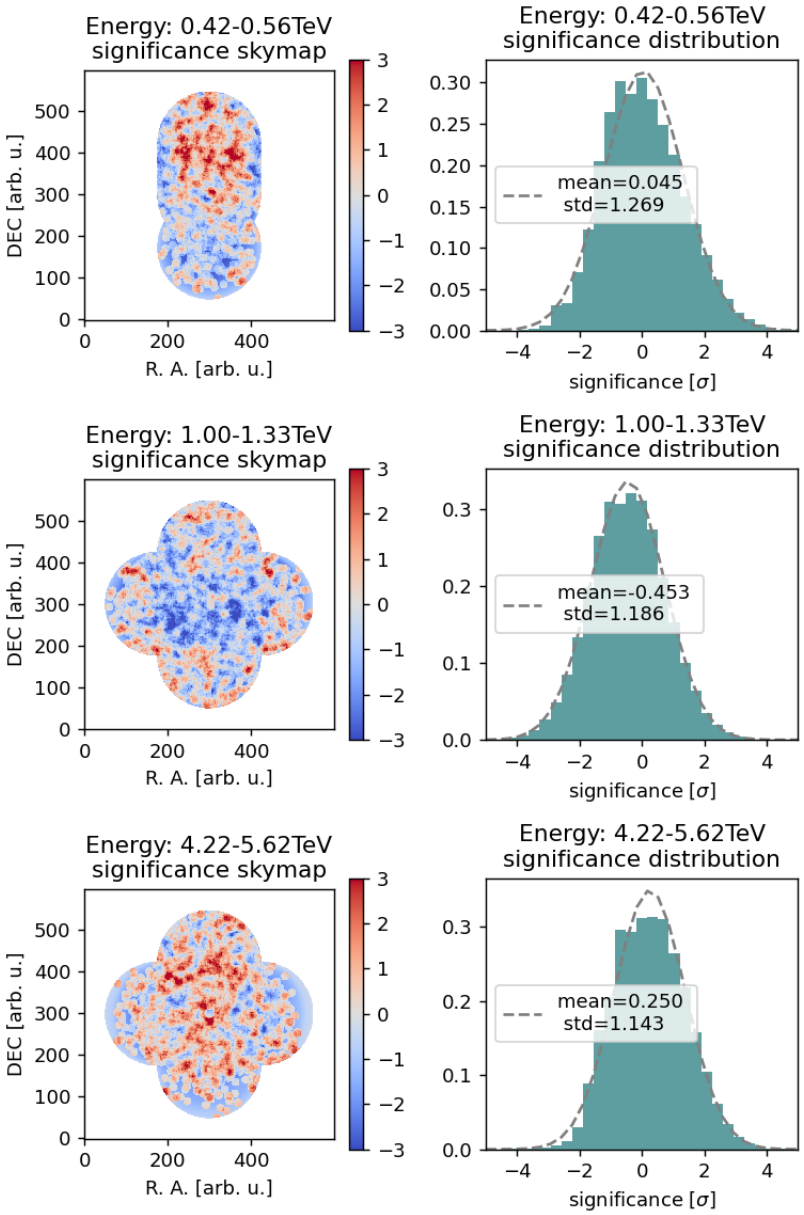

Figure 3.32: Significance skymap and its distribution for the stacked dataset. Each row presents a different energy bin.

model presents ∼ 7% fewer events than the data in the first energy bin. While at 1 TeV the model predicts ∼ 5% more events than the data and ∼ 7.5% fewer events at 5 TeV. At the end of the energy range, the error smoothly indicates an overestimation of the background; however, it is worth mentioning that this range has poorer statistics.

Thus, for this Crab stacked dataset, the error due to the systematics from the background model provides an underestimation of ∼ 7% of the total background events in the first energy bins, followed by an overestimation of the background of ∼ 5% at 1 TeV and underestimation of ∼ 7.5% at 5 TeV. At the end of the energy range, the error smoothly indicates an overestimation of the background; however, it is worth mentioning that this range has poorer statistics.

For completeness, for the energy bins with the highest error contribution, figure 3.32 shows the effect of the systematic error in the significance sky maps and its distribution on the right-hand plot.

The first energy bin has a contribution of fewer runs and therefore, the skymap covers less area of the sky. The positive systematic error appears in the skymap as a more dominant red region, also highlighted by a positive mean value in the distribution, meaning an underestimation of the background model. In the second row, for energies around 1 TeV, the systematic error is negative, presenting an overestimation of the background model, resulting in bigger regions towards negative significance in the skymap. Finally, the last row, presents the skymap of the energy bin at 5 TeV, with a positive systematic error, and therefore a positive significance dominance in the skymap.

To conclude, this section showed the method to calculate the background systematic error level for any dataset using lookup tables.

3.4.3 Including Systematic Error in an Analysis: Nuisance Parameters

One option for including systematic errors is by introducing nuisance parameters in the analysis of the stacked dataset. The parameters are binned in space and energy axes and included in the minimization of the likelihood, providing a corrected expected background level for the stacked dataset.

For instance, for energy bin at 1 TeV for the example Crab dataset, shown in figure 3.32, the model overpredicts the data, leading to an overall shift towards negative significance values. Thus, the nuisance parameters, in this case, would correct the model with a subtraction of the background events.

As a first approximation, we assume that the systematic error value at a given energy is normally distributed around the mean provided by the error curve.

The maximum likelihood equation, which is modified by the addition of one more term, is derived from the Gaussian distribution of the nuisance parameters. As a side effect the equation to be minimized, the $-2\ln\mathscr{L}$, with $\mathscr{L}$ defined in equation 3.10, has one more term as a penalty to the total likelihood. The correction of the systematic error is done via the new term ΔB, and $K_{ij} \equiv \Delta B_i \Delta B_j$ is the covariance matrix. Further description of this method can be found in [108].

$$\mathscr{L} = \prod_i p_i = \prod_i \frac{m_i^{n_i} e^{-m_i}}{n_i!} \times e^{-\frac{1}{2}\Delta B_k \, \Sigma (K^{-1})_{kl} \Delta B_l} \tag{3.10}$$

For this approach, the correction is done per bin in space and energy, therefore, the nuisance parameters are also defined in 3D.

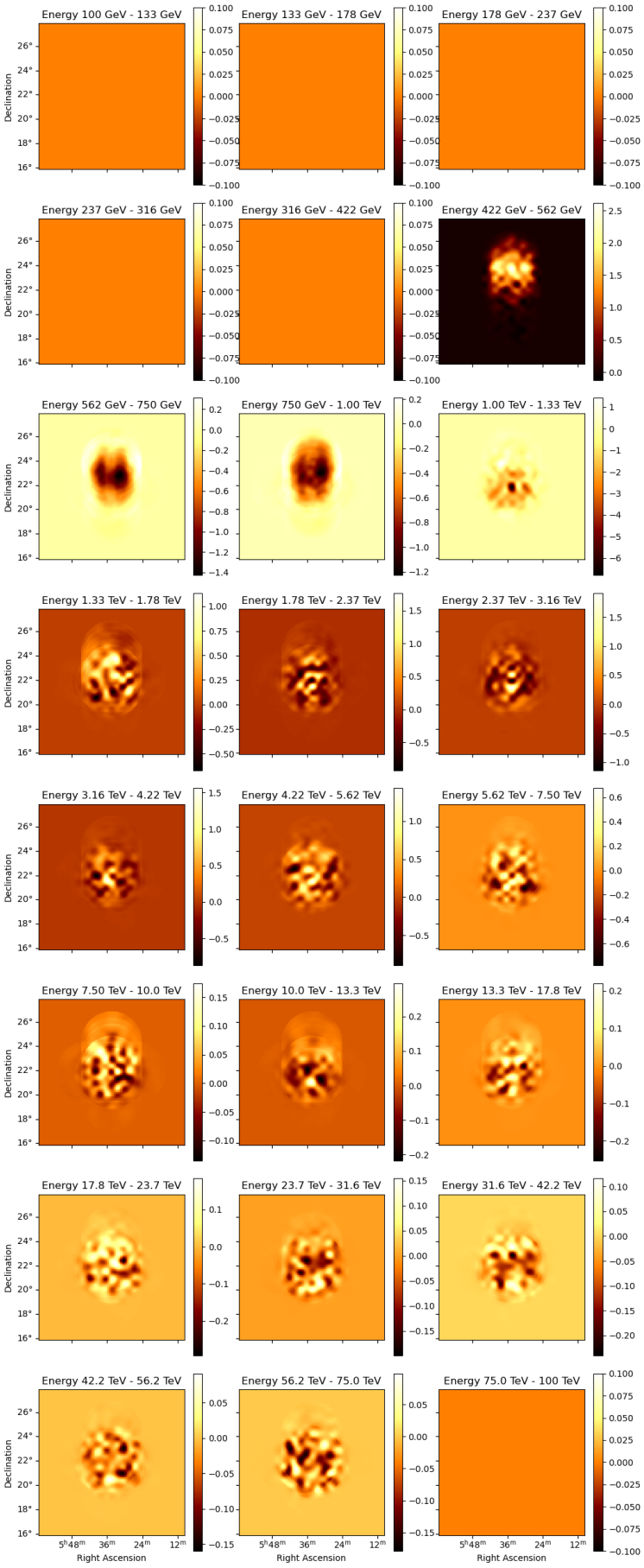

Figure 3.33: Skymap of the background correction due to nuisance parameter in each energy bin. The color map is shown in units of counts.

The energy bins of the nuisance parameters are constrained by this method and they must be the same as the analysis energy bins.

The choice of the spatial bins is not constrained by the error estimation method, since this method considers the integral of the source-free regions. However, the shape of the spatial error is known as extended regions in the FoV, caused by the miss modeling of the spatial asymmetry at low energies, as exemplified in figure 3.21. In the analysis, each run contributes to this spatial error pattern, resulting in a nonclear extended pattern in the stacked dataset. Thus, the nuisance parameters in the spatial coordinates depend on the dataset itself.

The size of the spatial bins for the nuisance parameter can be as small as the spatial bin of the analysis, or as big as the whole FoV. The finer the bin, the more computationally expensive. On top of that, the very fine bins can overfit the systematic and statistical errors.

The optimal size of the nuisance spatial bin must be larger than the point source extension and also larger than the PSF, and it is estimated by a method developed by [109] using simulations and Fourier transformation. Thus, the nuisance parameter does not correct for the point source contribution but rather for a bigger region where the point source is located. Thus, the implementation of the nuisance parameters does not lead to a miss modeling of the central source, which is a point source.

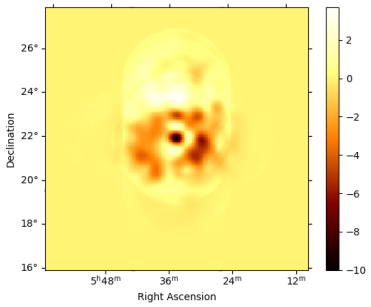

Figure 3.34: The background correction due to the nuisance parameters in the skymap integrated in energy, for the Crab example dataset.

The nuisance parameters are fitted together with the free parameters of the analysis, such as the parameters of the source. The result is a corrected estimation of the background in each bin of the dataset.

Figure 3.33 shows the sky maps of the background correction by the nuisance parameters for each energy bin, in units of counts. The energy bin 0.42-0.56 TeV, shows a positive correction, which compensates for the underestimation of the model shown in figure 3.32.

The next following two energy bins, also provide correction of background but on a much lower scale, since the expected systematic error for these bins is much lower. The next energy bin, from 1-1.33 TeV, shows a high level of negative correction, to compensate for the overestimation of the background observed in figure 3.32.

Note that the nuisance parameters do not follow the same spatial pattern across the different energy bins, thus it can cover the different spatial and energy behavior of the systematic errors.

The total effect of the nuisance parameters in the sky map integrated into energy is presented in figure 3.34.

Although the nuisance does not strongly impact the spectrum of strong point sources, such as Crab, it does change

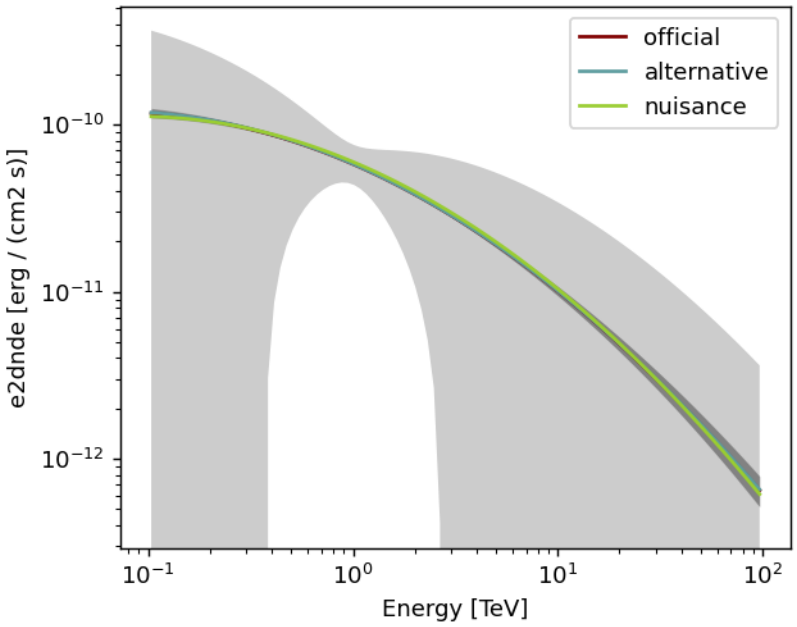

Figure 3.35: Best fit spectrum of the different Crab datasets, the official dataset is shown as the brown curve, the alternative dataset as the blue curve, and the nuisance dataset as the green curve. Both spectra are similar, showing a good agreement between them. The uncertainties are shown as the gray band. The larger gray band is derived as errors from the nuisance dataset.

the error bars, since it includes more parameters in the likelihood. Figure 3.35 shows the spectrum derived for different background estimations, using the official model, and the alternative model, and including the nuisance parameters. The spectra are very similar among the different settings, however, the uncertainty band of the nuisance parameter analysis is much bigger than the previous two, which overlaps.

Since the nuisance parameter analysis is still a novelty, some properties are still not implemented yet. Such as the flux points estimation of the confidence contours for the stacked dataset.

3.5 Overview of the Systematic Error Corrections in a Dataset

In this section, the systematic error corrections are shown using the example Crab dataset. The comparison is done between the official model, the alternative model, and the nuisance parameters in the analysis. For a fair comparison, the same low energy threshold, liberal, is applied.

One approach to demonstrate the improvement of the different corrections is to use the error of the corrected stacked dataset, based on equation 3.4. The comparison is shown in figure 3.36. The expected result for a perfect background model is a normal distribution of the error around zero. The convergence of the curves towards zero after each correction indicates the improvement of each step.

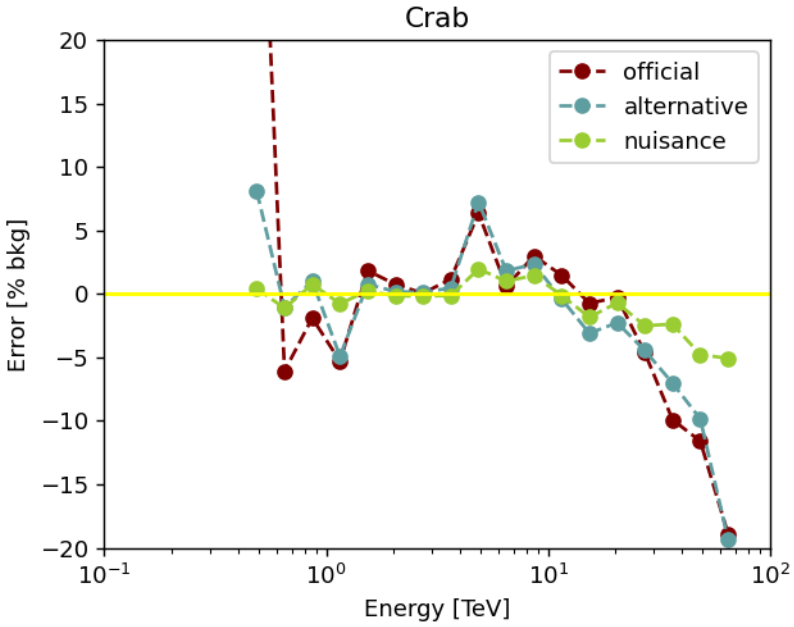

Figure 3.36: The background error comparison between the different dataset approaches. The brown points show the error calculated using the official 3D background model, the light blue points are using the alternative 3D background, and the green data consider the nuisance parameters. The error is in units of % of background in each analysis energy bin. The yellow line is a reference for zero.

Another observable effect of systematic errors is a non-uniform distribution of the significance in the skymap. The improvement of the corrections in the significance skymaps for integral in energy is displayed in each row of figure 3.37. The improvement of the corrections is observed by the mean and std values of the distribution getting closer to the expected of a normal distribution, zero and one. However, the integral in energy does not show the full improvement of the corrections, since it is done in individual energy bins.

Figure 3.38 presents the significance skymap for the three energy bins with the highest values of systematic error: at 0.5, 1, and 5 TeV.

The first energy bin presents a very poor description of the data by the official model. In the common practices of the official analysis, data at these energies is excluded due to high systematic errors. Here, it is a criterion of comparison for the other corrections. The alternative model presents a very good improvement in this energy bin, observed by a more uniform distribution in the skymap. The alternative model corrects runs with a high value of muoneff, and as presented in table 3.6, this dataset contains these runs. However, in case no runs with high muoneff are included in the stacked dataset, no big improvement is expected. Yet, some large-scale patterns in the spatial distribution of the alternative model are still observed. This issue is repaired by the nuisance parameters by showing a flat distribution of the significance.

The second energy bin ranges from 1-1.33 TeV, displayed in the third and fourth columns of figure 3.38. The official model

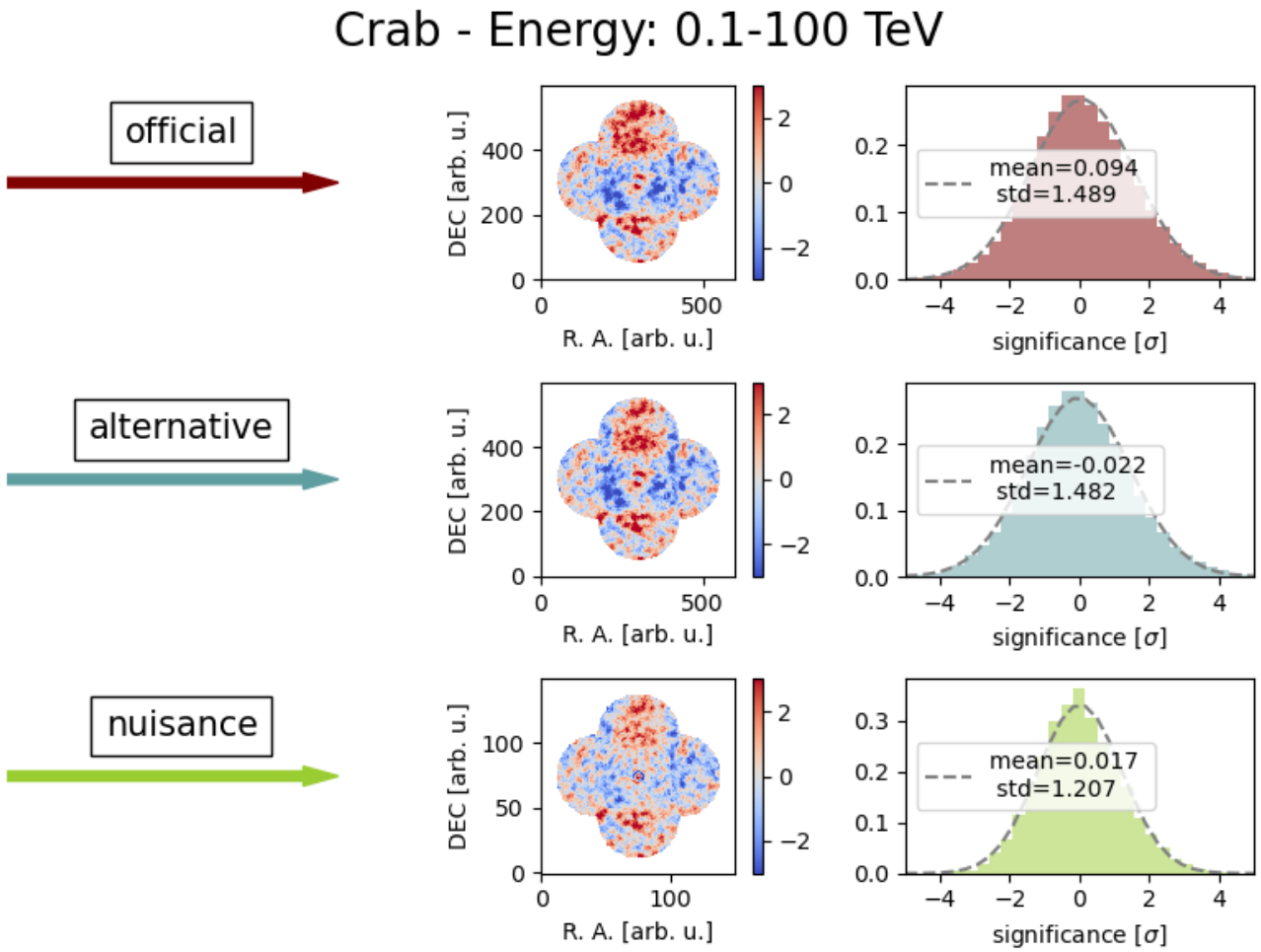

Figure 3.37: Significance skymap and its distribution, considering the integration of the energy range. The first row indicates the official 3D background model, the second row is the alternative background model and the last row is for the nuisance parameters correction. The fit of a gaussian and the mean and std are shown for the distribution on the plots of the last column.

presents a much better performance when compared to the previous energy bin. The systematic error pattern observed for the official model at 1 TeV presents a shift towards negative values, indicating an overestimation of the background. The pattern observed in the alternative model is very similar to the official model, as also observed in the error curves in figure 3.36. Using the nuisance parameters the spatial distribution is corrected and the significance skymap becomes more uniform, as expected for a good description by the model of the data.

The last energy bin presented covers the range of 4.22-5.62 TeV, which encompasses the 5 TeV BDT edge. Equivalently to the previous energy bin, the systematic error in the official model is observed in the same level and pattern in the alternative model and accounted for by the nuisance parameter step.

The official model performs better with a higher value of the low energy threshold. However, the goal here is to demonstrate that with these corrections the analysis can increase the statistics in lower energy when considering the systematic errors properly.

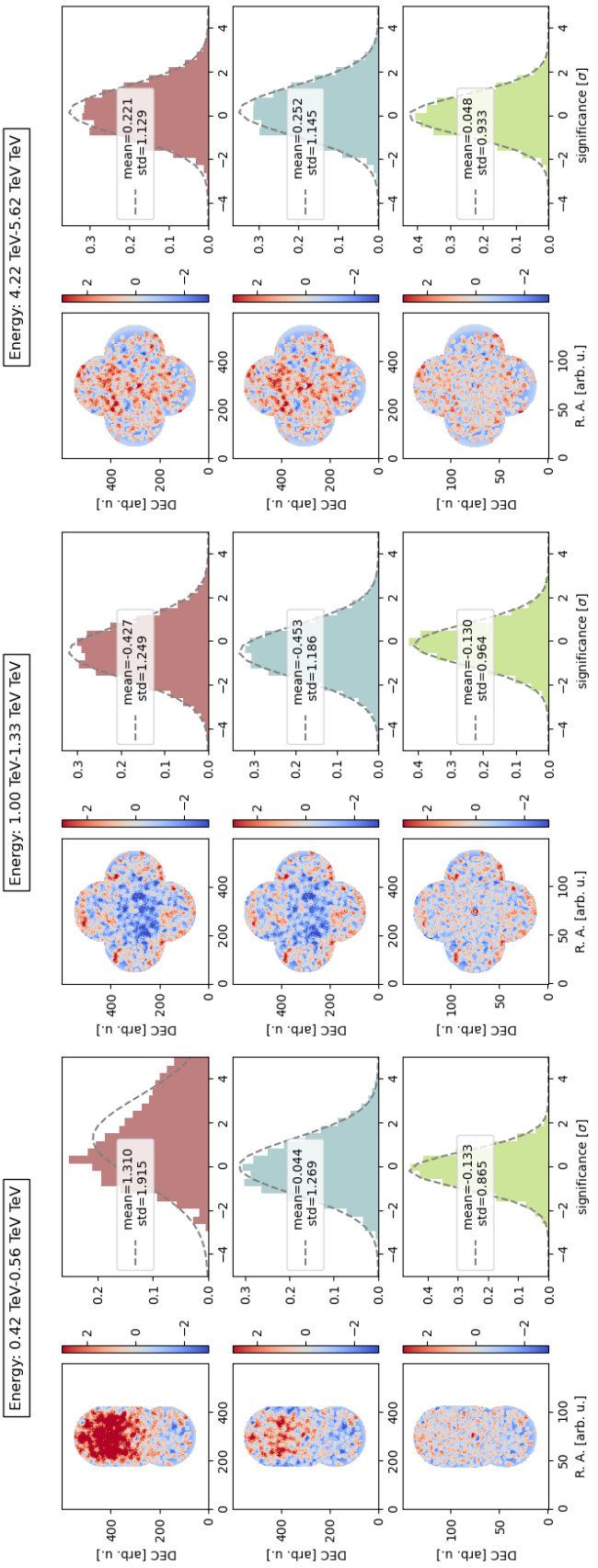

Figure 3.38: Significance skymap and its distribution, considering three different energy bins. Each row represents a dataset with different background estimations: the first row with an official 3D background model, the second row with the alternative background model, and the third row with nuisance parameters correction. The first two columns present the results for the energy bin: 0.42-0.56 TeV, the following two columns for the energy bin: 1-1.33 TeV, and the last two columns for the energy bin: 4.22-5.62 TeV. The skymaps present the spatial distribution of the significance and the total distribution, fitted with a gaussian distribution is shown on the right-hand side of each skymap.

The alternative model is implemented at the level of individual runs during the pre-fit process, by using an alternative construction of the 3D background model. It mainly corrects at the low energy for runs with high values of muoneff. This explains the difference between the official and the alternative model in low energies, and a similar behavior as the energy increases.

The correction of the nuisance parameter is applied for the stacked dataset. It improves the background estimation in the whole energy range, as observed from figure 3.36, and the whole FoV, as observed from figure 3.38.

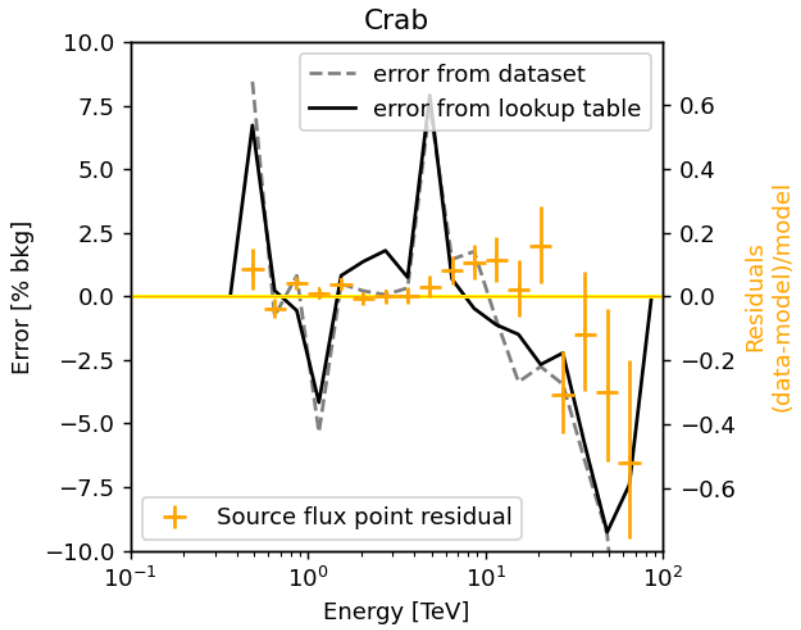

Figure 3.39: The systematic error of the background as continuous curves, solid black derived from lookup tables, and dashed gray derived from the dataset itself. The orange points show the residual of the flux points of the Crab source, with the scale on the right-hand side of the plot.

The systematic errors of the background model do not influence the description of an intense point source, since the error level is negligible compared to the source signal.

A comparison of the background error for the Crab stacked dataset and the residual of the source flux points is shown in figure 3.39. The different trends of the flux point residuals and the systematic error show the uncorrelation of the systematic error of the background and the spectrum of a strong point source.

It is worth mentioning that Crab has a very intense signal. However, for weak sources and or in crowded regions, the systematic errors of the background potentially influence the source analysis.

3.6 Summary and Outlook

This chapter introduced a method of estimating the systematic error of a 3D background template model for IACT data. The systematic error is provided per analysis energy bin, per systematic bin, and per run. Using this result, lookup tables are constructed and the estimation of systematic error of any dataset can be calculated. The spread of the systematic error in the energy range due to the analysis procedure is also presented in this chapter.

For the estimation of the systematic error, two main parameters are defined: (i) the deviation curve, one per run, which includes the systematic and statistical error; and (ii) the error curve, one per systematic bin, and is defined as the average of deviation curves, which provides only the systematic error in case of an infinite number of runs.

The systematic error per run is defined by the error curve and it is sign-dependent (positive or negative). The robustness of this estimation is provided by the spread of the deviation curves.

The method is valid for any 3D template background model version. For this work, the entire archival H.E.S.S. data, assuming the std_zeta_fullEnclosure configuration and the canonical energy bins of 8 bins/decade are used.

For these settings, there are two most prominent patterns observed for systematic errors. The first one is observed in the low zenith bins at low energies, caused by radial asymmetry. The second one is observed and in all systematic bins at 5 TeV, due to BDT edges.

This study presented the origins of the most prominent systematic errors: the radial asymmetry in the spatial distribution in low energies and the discontinuity of the model at BDT edge at 5 TeV.

The radial asymmetry issue affects especially runs with outlier values of the muoneff parameter. These outlier values indicate runs with a very good atmosphere and/or excellent experiment conditions, which fall out from the average runs. This matter can be corrected by constructing an alternative model version with one more bin for these special cases or by correcting the IRFs of these runs.

The second error cause comes from a procedure before the model construction and is attenuated by the analysis method, such as interpolation. Although this problem is model version dependent, it shed light on how the analysis method and steps before the model construction can introduce systematic error features.

This chapter also presented the inclusion of systematic error in analysis via the nuisance parameters method. Using the estimation of the systematic error level, it corrects the background estimation in energy and the spatial axes. The usage

of systematic error estimation and the improvement of the analysis is endorsed by the tests using the example dataset, Crab, a strong point source.

The systematic errors of the background model are negligible for strong point source analysis. However, it is potentially relevant as the source signal is comparable to the background estimation and/or it is located within complex and crowded regions. Thus, the next chapter is dedicated to applying the same method in the crowded region of the GC, to explore the spectral features of the central source in such a complex environment.

Caveats and limitations of this method must also be mentioned. This method considers runs with very similar exposure times. The less exposure time, the fewer the statistics and the method fails for these cases, one example of this type is a GRB analysis.

The presented method is robust; nevertheless, further improvements are possible. For instance, the asymmetry at low energies is caused by divergencies in the effective area of runs with high muoneff values. A new definition of IRFs is currently being developed and the method here developed can be used to explore the improvement of the new analysis compared to the current model version.

Another option for improvement is to explore more in-depth the causes of the high spread of the deviation curves, which is barely used in this analysis. This parameter indicates the robustness of the estimation, by the spread of the deviation curves, and could provide insights into new origins of the error.

This is the first step to establishing a common ground method for estimating the systematic error of IACT data, using a 3D background. It is robust and independent of any dataset, being applicable in a wide range of analyses. Besides, it allows estimating and including the systematic error in the analysis, admitting data that were previously excluded in the low energy range.

The Galactic Center Source in Gamma Rays

4

4.1 Introduction

The present study was designed to analyze the gamma-ray emission from the center of the Galaxy, using data collected by LAT and H.E.S.S. experiments, covering a total energy range of 600 MeV to 100 TeV. This is the first time the same analysis method, the maximum likelihood, and the same analysis software were used to combine the data from *Fermi*-LAT and H.E.S.S. for this region.

The Galactic Center region description bears a high degeneracy of astrophysical models. The accumulated data allows the possibility to test the astrophysical models presented in [23, 93], that predicts spectrum variability in the timescale of years.

Using 14 and 18 years of data from LAT and H.E.S.S. experiments, and the modern analysis method, the goals of this study are:

- Obtain the spectrum model for the sources 4FGL J1745.6–2859 and HESS J1745–290 with the maximum likelihood method using all available data.
- Apply the systematic error corrections in the H.E.S.S. analysis and demonstrate its improvement in the results for the source HESS J1745–290.
- Obtain the source spectrum in time intervals of two years for LAT and H.E.S.S. data.
  For LAT data, evaluate the physical model from [23], which assumes a flaring emission of leptons ~ 300 years ago from Sgr A*, that are cooling via IC. This model predicts a displacement of the bump emission towards lower energies. A decrease of ~5–10% in the energy flux, in the range 1–10 GeV in the 10 years time scale is expected.
  For H.E.S.S. data, evaluate the physical model from [93], which assumes a flaring emission of protons ~ 10 years ago from Sgr A*, cooling via p-p interaction. This model predicts a spectrum variability above 10 TeV in the time scale of 5 years.
- Tests for pectrum variability for each instrument, and possible correlation between them.

An astrophysical model can in principle also be fit in the maximum likelihood analysis in gammapy. However, due to the high degeneracy of models describing the data, this work focuses on excluding possible model parameter values of astrophysical models rather than fitting an astrophysical model to the data.

4.1.1 Methodology

The analysis is performed using the data of each instrument separately, although a joint analysis is supported in gammapy. The data is stored in *MapDataset* gammapy objects, whose geometry is defined accordingly to the instrument's capabilities.

Firstly, considering each experiment's archival data up to date, the central source spectrum is obtained, here namely the full-time spectrum. It comprises the 14 and 20 years for *Fermi*-LAT and H.E.S.S., respectively. This spectrum is settled as a reference for time variability studies. The spectrum variability analysis is performed by splitting the archival data into two years time intervals. This work adopts the following color convention: the full-time spectrum is displayed in black, while each time bin dataset is assigned to one color.

To complement the resulting spectra, other products of the 3D analysis, such as significance sky maps and flux points, are presented.

Spectrum variability is evaluated by comparing the individual time bin spectrum to the full-time spectrum. As a consequence of such investigation, the astrophysical models from [23, 93] are automatically tested and some other subproducts of the analysis are also presented to support the discussion. The last part is dedicated to a combined discussion of *Fermi*-LAT and H.E.S.S. results.

The input model is assumed from catalogs and it comprises spatial and spectral parameters. Since this analysis is focused on the spectrum, the spatial model is set as fixed to decrease computational expenses.

The neighboring gamma-ray sources in the FoV are assumed to be well-described by the catalog models and therefore are set as steady contributions in the analysis. In both experiments, the gamma-ray diffuse emission is introduced as a 3D map template. These parameters are fitted in the full-time analysis. The best-fit values of the diffuse emission are set as fixed for the time bin analysis to preserve the same contribution from it for the different time periods.

The intrinsic difference between LAT being a survey and H.E.S.S. a pointing instrument results in different statistics available for the time bin analysis. While LAT provides a fairly constant volume of data across all time periods, H.E.S.S. does not. Consequently, by assuming the same time periods for both experiments, as this work does, H.E.S.S. has an additional uncertainty caused by the different statistics available.

The hypothesis test for each time bin dataset is performed to verify whether the spectrum obtained in each time period differs significantly from the full-time spectrum. For this, the probability of data D_i of time bin i is calculated considering

two different central source spectral models. The null hypothesis H_{null} assumes that the full-time spectrum is a good model for each time interval, thus assuming the full-time spectrum for data D_i. The alternative hypothesis $H_{\text{alternative}}$ assumes the best-fit spectrum obtained in the time interval i. The probability of D_i yielding from each hypothesis is compared, resulting in the variable $\sqrt{\Delta\text{TS}_i}$, defined as:

$$\Delta\text{TS}_i = -2\ln\frac{P(D_i \mid H_{\text{alternative}})}{P(D_i \mid H_{\text{null}})}. \tag{4.1}$$

The variable $\sqrt{\Delta\text{TS}_i}$ has units of statistical significance, σ, since in this case considering the number of degrees of freedom is one, the number of measured events. The $\sqrt{\Delta\text{TS}_i}$ compiles the probability of wrongly excluding the null hypothesis due to statistical fluctuations.

The test of each time bin dataset counts as one trial in searching for spectral variability. For a correct statistical treatment, the total number of trials N, in this case, equivalent to the number of time bin datasets, must be properly included in the calculation [110]. This step prevents the bias of assuming spectrum variation based on the most convenient result, among all the other options. The procedure assumed in this work follows the description from [111]. For each dataset i, with the hypothesis test resulting into α_i, the new probability P'_i considering the trial factor N has the shape of:

$$P'_i(\text{at least one test with } p\text{−value} < \alpha_i) = 1-(1-\alpha_i)^N. \tag{4.2}$$

Thus, the corrected values of hypothesis tests are presented and used as an argument for discussion on the spectral variability of the central source.

4.2 *Fermi*-LAT

For this analysis, the LAT Pass 8 (P8R3_V3) data is used, retrieved online in the FITS format. However, to be correctly introduced in gammapy the data must be converted using *Fermi* Science Tools, *Fermi*py [112]. The products from *Fermi*py can be categorized into two types: the measured data, and information about the instrument and observation. The data is provided in an event list, accounting for the detected photons and their features. The observation information condenses the IRFs and exposure time information into cubic shape, the appropriate for *MapDataset*.

The geometry of the *MapDataset* for the LAT data is defined with a spatial bin size of 0.2° and further details of the geometry are defined accordingly to the analysis goals, explored in the following section.

Table 4.1: Data selection criteria of *Fermi*-LAT, separated into the medium and high energy range.

parameter	med_energy	hi_energy
energy range	600 MeV - 4 GeV	4 GeV - 1 TeV
event class	1024, P8R3_ULTRACLEANVETO_V3	128, P8R3_SOURCE_V3
event type	32, PSF3	512, EDISP3
isotropic model	iso_P8R3_ULTRACLEANVETO_V3_v1.txt	iso_P8R3_SOURCE_V3_v1.txt
energy bin/dec	12	8

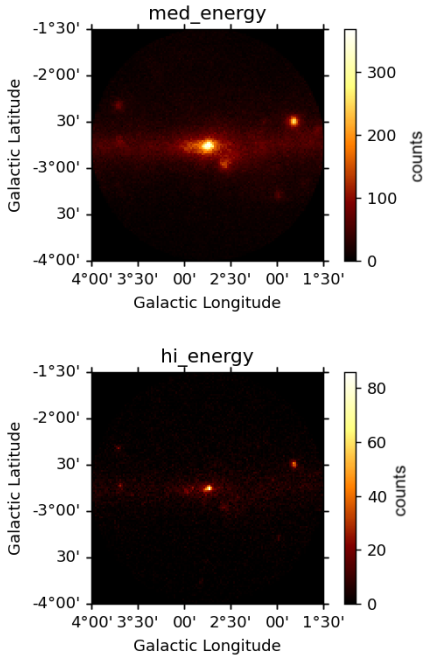

Figure 4.1: Skymap of selected data from LAT, top for med_energy dataset, 600 MeV-4 GeV, and bottom for hi_-energy dataset, 4 GeV-1 TeV, in units of counts.

4.2.1 Data Selection

The data selected ranges from October 27th, 2008 until July 2nd, 2022, equivalent to 246823875–678426195 in Misson Elapsed Time (MET) units. Although LAT measurements began on August 4th, 2008, the time gap between it and the chosen starting date is justified due to considerable background contamination above energies 30 GeV, as described in the caveats webpage.

Although LAT capabilities reach energies as low as 30 MeV, the energy range assumed for this work spams from 600 MeV to 1 TeV, since the expected spectral variability of this study is visible only in the high energy range. Thus, the low-energy data, besides containing higher systematic uncertainties, is irrelevant to this analysis. The FoV chosen is 5°, based on the 95% containment at the poorest PSF performance at 600 MeV, the analysis' lowest energy, and still enclosing enough statistics for modeling the galactic diffuse emission.

Across the energy range, the IRFs vary considerably and therefore, the data is divided into medium and high-energy datasets. The configurations of each dataset are optimized accordingly to the performance of the instrument within the energy range and shown in table 4.1.

The medium dataset is often mentioned in this work as a low-energy dataset. It contains more statistics, affording a finer energy binning. This energy range has higher uncertainties regarding the photon incoming direction; thus harder selection cuts and emphasis on the PSF are applied.

The high-energy dataset, with considerably lower statistics and better direction precision, adopts standard source analysis selection cuts, with emphasis on the energy dispersion of the events.

Figure 4.1 shows the selected data of each dataset displayed in sky maps in units of counts. Compared to the high-energy dataset, the medium-energy dataset presents higher statistics, visible from the range of the color scale, a more prominent diffuse emission from the Galactic Plane, and a larger extension of the central source emission.

For the time bin analysis, the selected data is split into bins of 2 years duration, accounting from the starting date 2008-10-27. The last bin covers until 2022-07-02, with slightly fewer statistics.

4.2.2 Assumed Models

There are three main types of input models considered in this analysis: (I) the central source, the object of interest, (II) the diffuse emission from the galactic plane, and (III) neighboring gamma-ray sources within the FoV. Figure 4.2 presents the expected counts' sky maps of each model contribution. For both datasets, the model assumed is the same and fitted simultaneously.

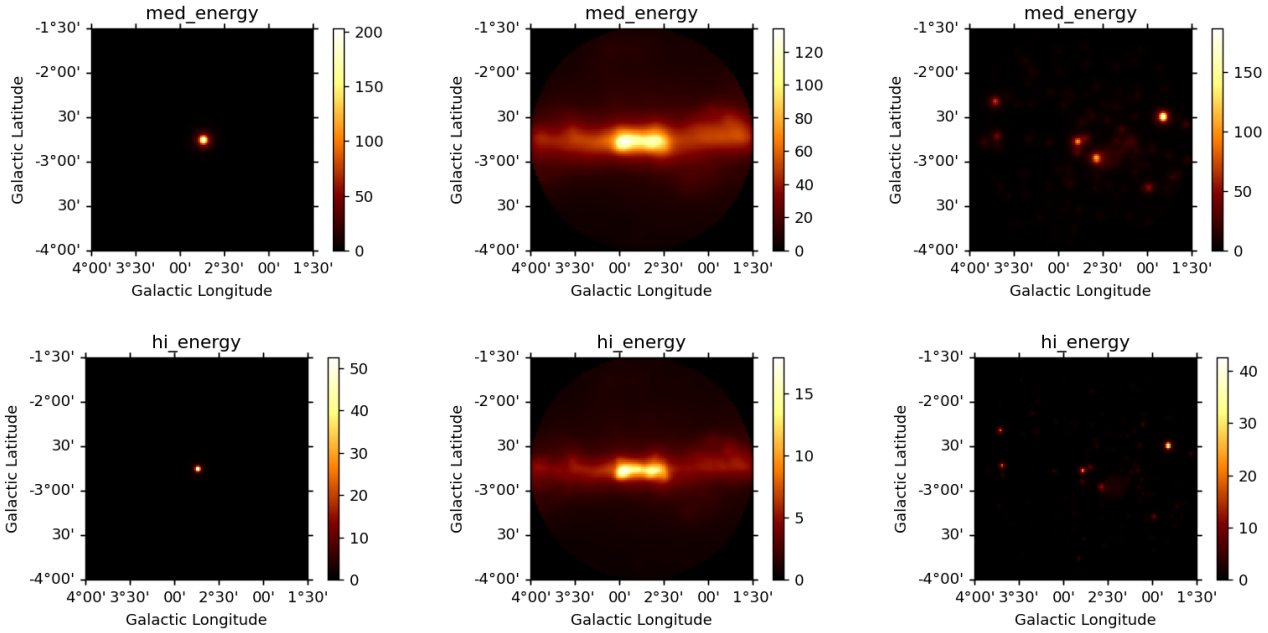

Figure 4.2: Expected counts skymaps from the models: (left to right) central source, diffuse emission neighboring sources. The different rows indicate the different energy datasets, top for medium and bottom for high energy, with respective energies 600 MeV-4 GeV, and 4 GeV-1 TeV.

The Central Source The emission from the galactic center source is identified as 4FGL J1745.6–2859 in the 4FGL catalog. It is modeled as a point source located at (266.415°, -28.997°) in ICRS coordinates, with a log parabola spectral emission, described by the following function:

$$\phi(E) = \phi_0 \left(\frac{E}{E_0}\right)^{-\alpha-\beta\log\left(\frac{E}{E_0}\right)} . \tag{4.3}$$

The catalog values of each parameter are described in table 4.5. The free parameters in this analysis are ϕ_0, α, β, and the remaining ones, including the spatial parameters, are set as frozen.

The Diffuse Emission The diffuse emission from the Galactic Plane is provided by the LAT collaboration as a 3D map template, optimized for the P8R3_V3 data. Within the gammapy framework, such a model bears spectral normalization and

index as free parameters. The best-fit values are set as frozen for the time bin analysis.

Similar to the Galactic Plane diffuse emission, the isotropic emission is also provided by LAT. It is optimized for P8R3_V3 data and also for the different event class configurations. The assumed isotropic models are described in table 4.1. Since its influence is negligible compared to the Galactic diffuse emission, its contribution is set as frozen to decrease computational costs.

Neighboring Sources All the gamma-ray sources in the 4FGL catalog within the FoV with a significance detection higher than 5σ are considered. These sources' contributions are set as frozen throughout the entire analysis. Although this approach does not provide a perfect description of the entire region, it considerably simplifies the analysis, and it is enough for spectrum variability analysis.

4.2.3 Spectral Analysis

The full-time analysis results in best-fit values for 4FGL J1745.6–2859 and diffuse emission described in table 4.5. Figure 4.3 shows the comparison of the catalog and the best-fit model spectra of the central source.

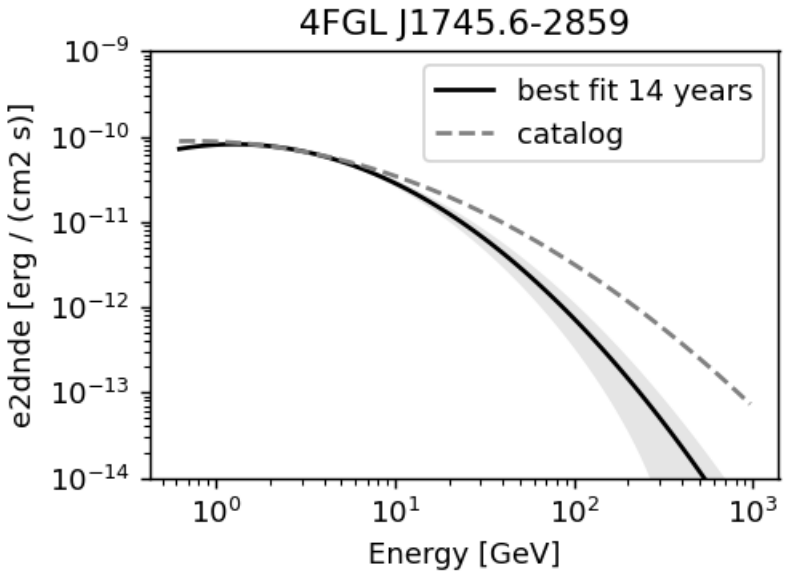

Figure 4.3: Spectral model of 4FGL J1745.6–2859. The solid black line shows the best-fit model derived from this analysis, with uncertainty described by the gray band, and in the dashed gray line is the input catalog model.

The discrepancy between the best-fit and the catalog models above 10 GeV observed in figure 4.3 is heavily caused due the different analysis procedures assumed to obtain the spectrum. While in the catalog analysis, the gamma-ray sources'

Table 4.2: Best fit parameters for *Fermi*-LAT data of source 4FGL J1745.6-2859 considering data over 14 years.

parameter	catalog value	best fit value
	4FGL J1745.6-2859	
ϕ_0 10^{-13}/(cm^2 MeV s)	6.78	6.22 +/- 0.34
α	2.601	2.806 +/- 0.09
β	0.137	0.247 +/- 0.04
	diffuse emission	
normalization	1	0.615 +/- 0.01
tilt	0	0.058 +/-0.00

contributions are fitted simultaneously, in the present analysis, the contributions of the neighboring sources are fixed. Further discussion about it is presented in the section about the analysis stability.

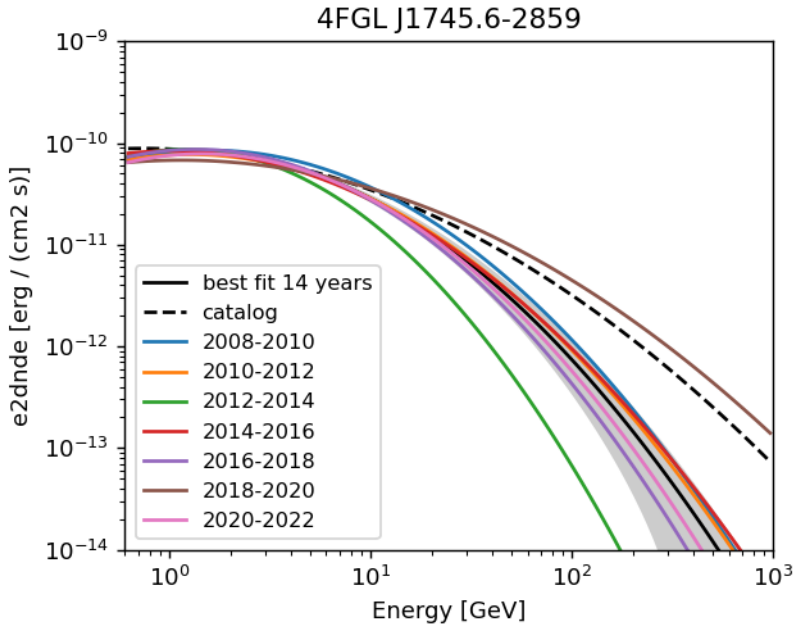

Figure 4.4: Spectrum from 4FGL J1745.6–2859 spectrum for two years time interval bins. The spectrum from the catalog and the full-time best fit, and its uncertainty band, are shown for comparison.

The results of the spectrum of each time bin dataset are shown in figure 4.4. The majority of the spectra are in agreement with the full-time spectrum, displayed as the black line. Even in the case of physically steady emission, spectrum fluctuations are expected due to the stochastic nature of the emission process. No clear trend in the spectra is observed with time. At high energies, the datasets from the time period of 2012-2014, green, and 2018-2020, brown, present the largest divergence from the full-time spectrum and they are in opposite directions.

Figure 4.5 shows the best-fit values distribution in parameters phase space. The high discrepancy observed in figure 4.4 for the 2012–2014 and 2018–2020 datasets are observed as high variation values of amplitude, α and β parameters. Additionally the 2008–2010 dataset, also presents a high variation in amplitude, although not clearly visible in figure 4.4.

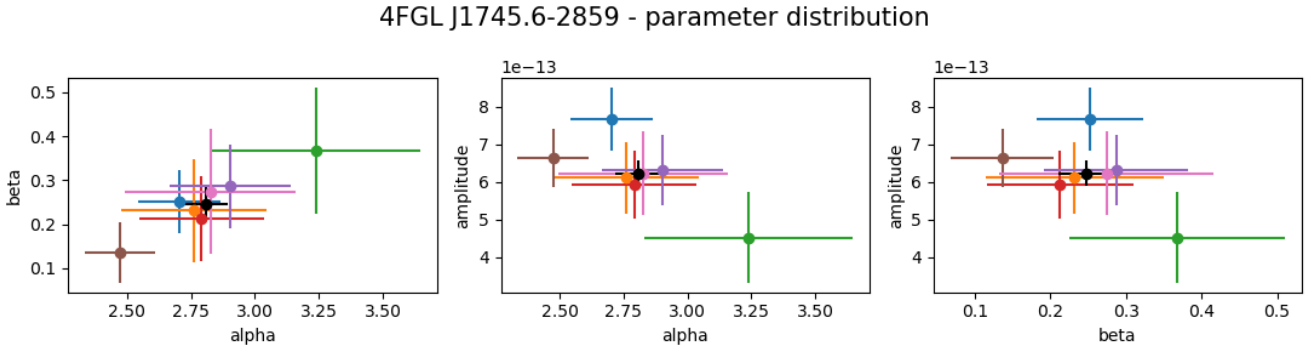

Figure 4.5: Distribution of the best-fit parameter values of each time bin dataset. The color scheme follows the color convention adopted in this work. The 14 years' best-fit values are shown in black.

4.2.4 Analysis Stability

Significance Sky Maps Figure 4.6 shows the results of the significance sky map for each dataset. It presents a positive shift for the low-energy dataset, and a negative shift for the high-energy. A positive value of significance indicates an underestimation of the model, while negative values indicate an overprediction of the model. Furthermore, the high-energy dataset provides a spatial pattern in the skymap similar to the morphology of the diffuse emission model, highlighting the impact of the diffuse emission model in this analysis.

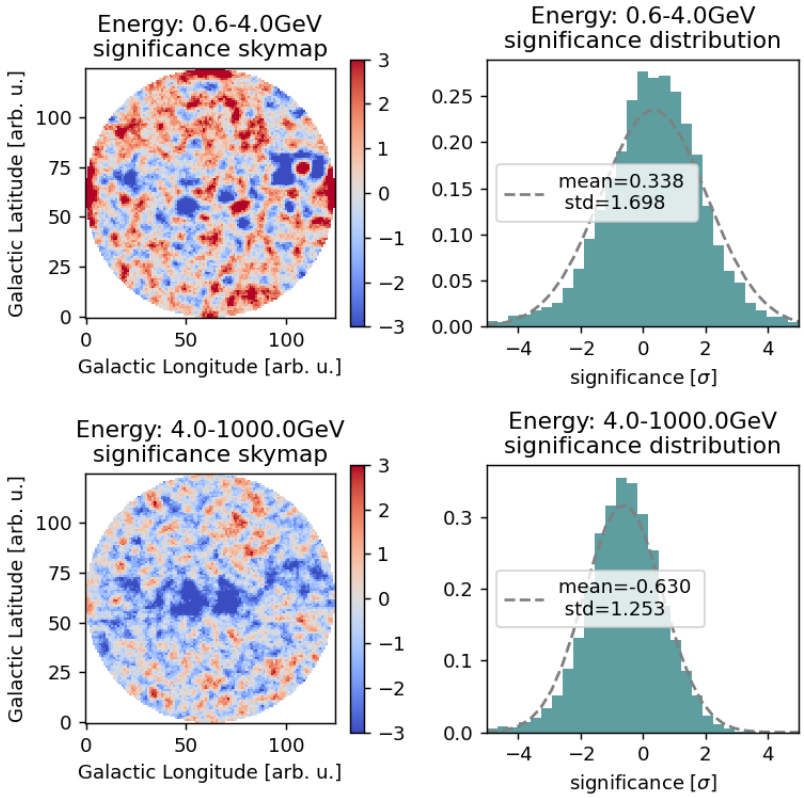

Figure 4.6: Significance sky map, in the first column, and the significance distribution, in the second column. The upper row shows the results for the low-energy dataset, while the bottom row shows the high-energy dataset. These results are integrated in the energy range of each dataset, for the 14 years dataset analysis.

In this analysis, the neighboring gamma-ray sources are assumed to be well described by the catalog model and set as frozen contributions in the analysis. This scheme tightly limits the fit of the diffuse emission, and subsequently, affects the spectral description of the central source. However, such limitation does not influence the goal of the analysis which is the spectral variability of the central source.

For the variability analysis, it is important to maintain the external contribution, as from the neighboring sources, constant over time to reveal possible variations of the central source. Hence a first-order approximation of the region, as provided by the catalog model, is sufficient.

However, one implication emerging from this assumption is the inaccurate best-fit values of the diffuse emission. The maximum likelihood method attempts to compensate for the neighboring sources' bad modeling with the diffuse emission's free parameters. Consequently, patterns of the bad fitting of the diffuse emission arise in the sky map, as is observed in the high-energy dataset in figure 4.6.

The maximum likelihood calculation prioritizes the low-energy range due to the higher statistics, leading to better results for this dataset compared to the high-energy range. This effect is observable in figure 4.6 in which the low-energy sky map presents a more homogeneous distribution, while the high-energy dataset clearly presents a pattern. The pattern indicates the diffuse model is overpredicted in this dataset.

The overprediction of the diffuse emission in the high-energy results in an underprediction of the central source model, due to the spatial correlation between the two emissions. Such an effect is observed as a lower gamma-ray emission at high energies for the spectral model of the central source.

Thus, the discrepancy observed between the best-fit spectrum of this analysis and the catalog model is a consequence of assuming frozen contributions of neighboring sources.

However, for the goal of this work, a first-order description of the diffuse emission is enough. Therefore, the best-fit values of the diffuse emission obtained from the full-time analysis, are set as frozen for the time bin analysis. The significance sky map and its distribution for each time interval are shown in figure **??** in the appendix. For the time bin significance sky maps, a similar pattern is observed, the significance distribution of the low-energy dataset presents a shift toward positive values whereas the high-energy dataset with a shift toward negative values.

Flux Points For each energy bin, the flux from a source is calculated considering the IRFs and all input models. Poor modeling of the external contribution leads to a deceptive estimation of flux points.

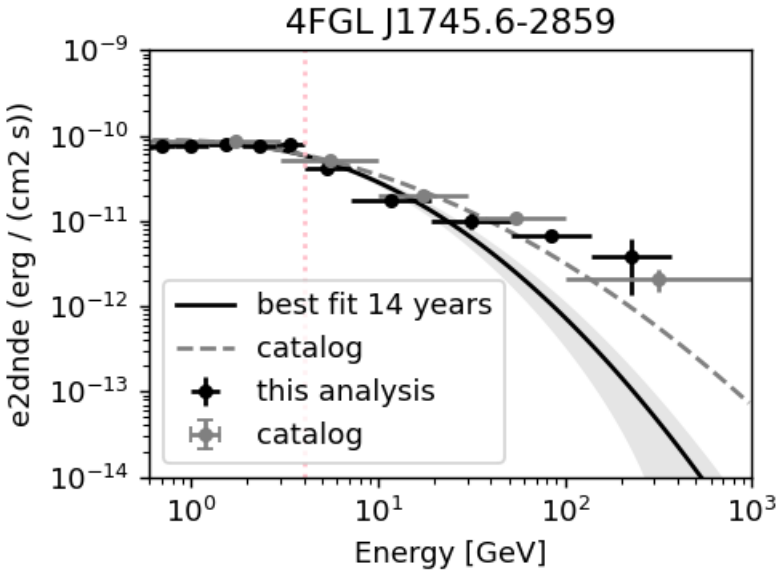

Figure 4.7: Flux points for source 4FGL J1745.6–2859 in comparison with the catalog values. the results of this analysis are displayed in black while the catalog model is displayed in gray. The vertical light pink line separates the low and high-energy datasets.

Figure 4.7 shows the comparison of the flux points from the 14 years dataset and from the catalog. Up to 40 GeV, the flux points present are in good agreement indicating the robustness of this analysis. The absence of a flux point in the last energy bin, above 40 GeV, is another consequence of the mis-modeling of the diffuse emission.

The overprediction of the diffuse emission model in the high-energy dataset leads to a lower flux of the central source. This effect is observed in this case as the absence of a flux point in the last energy bin.

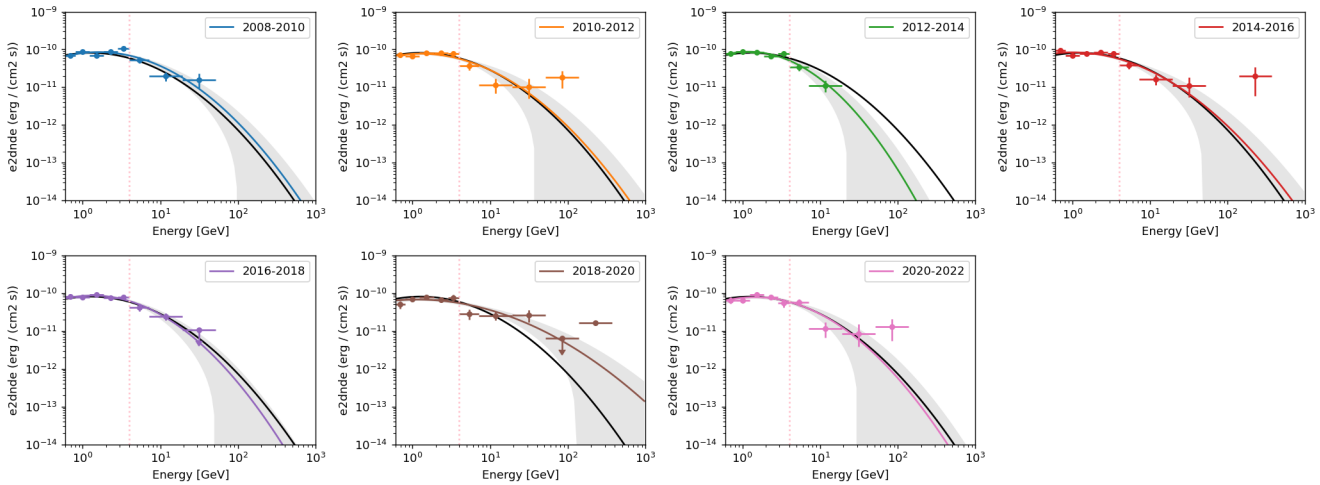

Figure 4.8: Flux points for each time bin dataset from the central source, together with the best-fit full-time spectrum and the best-fit spectrum for the specific dataset. The color scheme follows the convention of this work. The dashed vertical line shows the energy edge of the low and high energy datasets.

The flux points for each time bin dataset are shown in figure 4.8. Most of the flux points in the time bin datasets agree with the full-time spectrum. The exceptions occur for particular

energy bins in the 2008–2010, 2012–2014, and 2018–2020 datasets. The high amplitude in the spectrum for the 2008–2010 dataset is caused by the high value of the last flux point from the low dataset. It is an isolated energy bin and does not represent an overall higher normalization.

The 2012–2014 dataset shows no flux points above 20 GeV, indicating that indeed this dataset has a lower flux compared to the other datasets. This lower flux is responsible for the high α and β values. And the opposite behavior is observed in the 2018–2020 dataset, which presents three more flux points compared to the 2012–2014 dataset, being the flux point from 50-100 GeV an upper limit. The last flux point, above 100 GeV, presents high statistics, observed by the small error bars, and justifies the behavior of the spectrum with low values of α and β.

In conclusion, the agreement of the flux points from the full-time analysis and the catalog indicates stable results. It demonstrates again that the difference in the spectra is due to the very high range, above 40 GeV. The variation in the 2012–2014/2018–2020 spectra is endorsed by the absence/intense of flux points at high energies. It requires further investigation to test whether this behavior is within the statistical fluctuations.

Confidence Contours The confidence contours indicate the parameter space values which provide a valid description of the data within certain statistical fluctuation levels. As a convention in this work, the confidence contours from inner to outer lines are for 1, 2, and 3σ confidence levels.

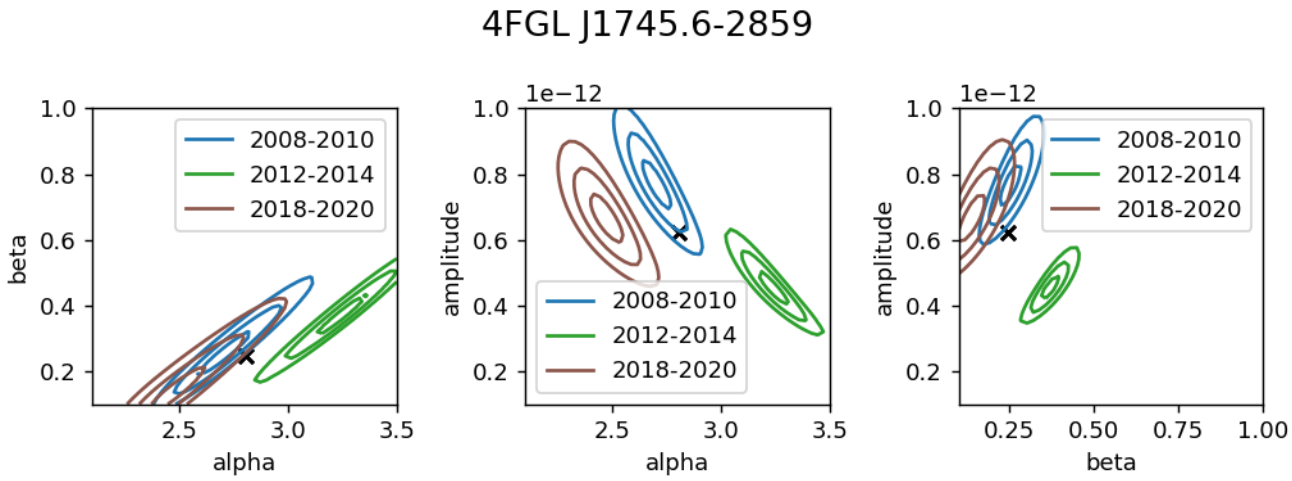

Figure 4.9: Confidence contours of the three most extreme datasets, 2008–2010, 2012–2014, and 2018–2020 for the spectrum fitted parameters. The best-fit values for the 14 years spectrum are shown as the black cross. The edges of plots are the limits in which the parameters are allowed to vary.

The confidence contours of the three most extreme datasets are presented in figure 4.9. By not including the best-fit full-time values within the outermost contour, the full-time spectrum fails in describing the 2012–2014 and brown datasets within 3σ confidence level. the 2008–2010 and brown datasets

are more similar among them than compared to the 2012–2014 dataset, highlighting the uniqueness of the 2012–2014 dataset.

4.2.5 Discussion

Based on the spectral results from the time bin analysis, the spectrum variability is investigated and consequently, the prediction from the astrophysical model [23] was examined.

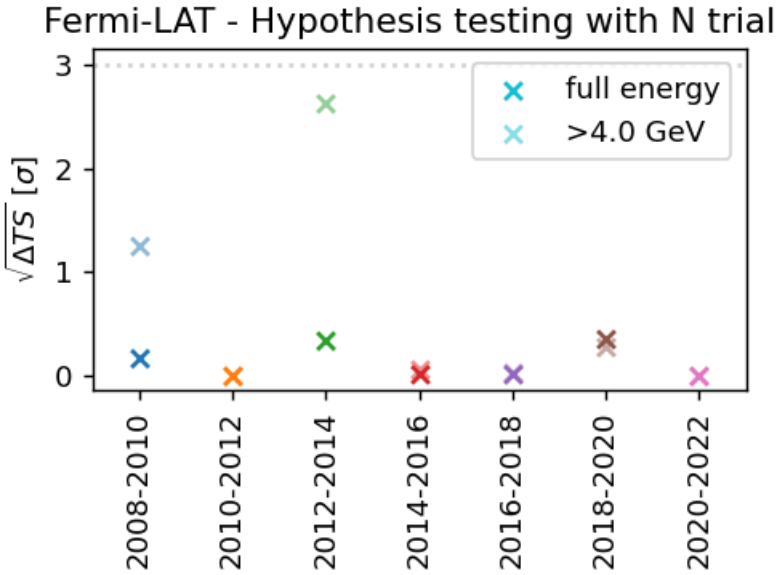

Figure 4.10: Results of $\sqrt{\text{TS}}$ for each time bin dataset in units of σ. The solid cross shows the results considering 600 MeV-1 TeV, while the transparent cross shows the results considering only the high-energy dataset, which is above 4 GeV. The dotted light gray horizontal line is set as 3σ for comparison.

Testing the Spectrum Stability over Time Figure 4.10 shows the results of the hypothesis tests for each time bin dataset, considering the number of trials N, calculated using equations 4.1 and 4.2. From it, neither the full energy range nor the high energy range presents significant values of $\sqrt{\Delta\text{TS}}$, meaning that the null hypothesis cannot be rejected. This indicates that the 14 years spectrum describes the data in the time bin dataset within the statistical fluctuations. The most critical values are shown for the high energy of green and blue datasets; however, it is not statistically significant to exclude the null hypothesis.

The results shown in figure 4.10 consider the number of trial factors as treated in [111]. Results considering only the hypothesis test, meaning calculated using only equation 4.1, are shown in figure 4.11 for comparison. Omitting the number of trials, the $\sqrt{\Delta\text{TS}}$ values are higher, above 5σ for the high energy range for the 2012–2014 dataset. The comparison between the values shown in figures 4.10 and 4.11 elucidate the influence of the trial factor in one analysis.

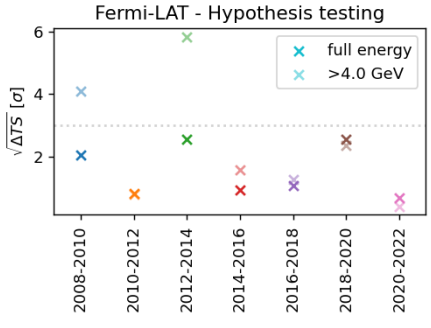

Figure 4.11: Similar description of figure 4.10, however the $\sqrt{\text{TS}}$ calculation considers only equation 4.1.

In conclusion, this analysis argues the absence of spectral variability in the full-time spectrum supported by the low values of $\sqrt{\Delta TS}$.

Physical Model Testing The astrophysical model presented in [23] combines the two components of the spectrum from GeV-TeV. It assumes a leptonic scenario cooling via IC with two different injection processes, a constant injection, responsible for the high energy emission observed in H.E.S.S., and one flaring episode, occurring ~300 years ago, responsible for the emission observed with *Fermi*-LAT.

The flare episode is supported by echos measured in X-ray and radio in the neighboring region. In this hypothesis, only the GeV component is predicted to present spectral variability and therefore the description is focused on this part of the model. During the flaring emission, electrons are injected with a spectral index of 1.5, reaching a gamma-ray luminosity of 2×10^{39} erg/s. After the flare, the emission decreases by a factor of the order of 10^4. In this hypothesis, considering a gradual cooling via IC mechanism in the GC ambiance characteristics, the higher energy electrons cool down shortly after the end of the flare, and its emission is no longer observable, while the cooling of lower-energy electrons, of the order of 10 GeV, reproduces a compatible gamma-ray spectrum observed currently with LAT. As a consequence of the gradual cooling of the electrons, this model predicts a variation in the gamma-ray emission, as a shift of the GeV bump towards lower energies in a 10 years time scale. Moreover, in this time scale, the energy flux in the 1–10 GeV range is expected to decrease 5–10%.

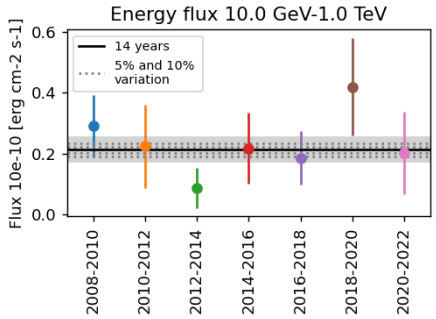

Figure 4.12: Energy flux from 10 GeV-1 TeV for different time bin datasets. The energy flux from the full-time dataset is shown as a constant black line, with the error bar shown as a gray band. The dotted lines show the 5 and 10% variation from the full-time flux for comparison.

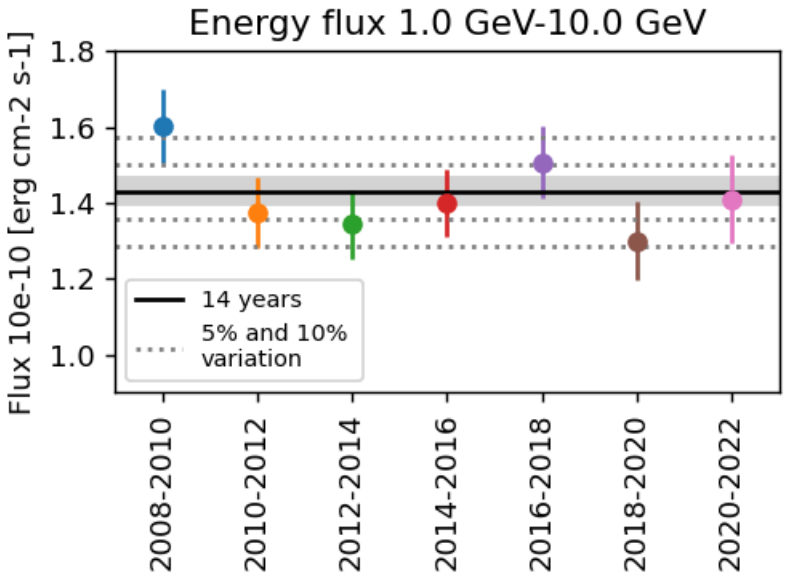

Figure 4.13: Energy flux calculated from the best-fit spectral model, full-time as a black constant line, and time bin datasets, colored points, in the range of 1–10 GeV. The gray band is the 1 σ uncertainty for the full-time energy flux. The dotted lines represent the 5 and 10% variation of the full-time energy flux.

The features predicted within this model is would be observed as a trend in time of the best-fit values of the spectrum. However, this pattern is not observed in figure 4.5. Furthermore, the energy flux in the 1–10 GeV shows no decrease with time, as presented in figure 4.13. Although the uncertainty in the 14 years flux (gray band) is smaller than 5 and 10% variation (dotted horizontal lines), for the individual time bin, the uncertainty is larger and of the order of the expected variation. Nevertheless, the energy flux in the different time periods is constant within the statistical fluctuations.

Since the cooling process in this time scale would displace also the high energy tail of the GeV emission, another interesting parameter to test is the energy flux above 10 GeV. A trend in time of this variable would support a gradual cooling, however, it is also not observed as shown in figure 4.12.

Based on absence the of spectral variability analysis using the 14 years of archival data of LAT, and the absence of a trend in time of the energy flux as shown in figures 4.12 and 4.13, the emission in the GeV range cannot be explained by electrons cooling down from only one major flare episode from 300 years ago. However, an important caveat is a high degeneracy among the model values, as mentioned in [23]. However, additional recent flares episodes with lower intensity after the major flare of 300 years ago, are also feasible and they would contribute to injecting more particles, resulting in the absence of the trend in time of the studied parameters.

4.3 H.E.S.S.

This analysis uses the H.E.S.S. DL3 FITs format data [43] and the 3D template background model.*. Similarly to *Fermi*-LAT case, this analysis consists of a full-time dataset, for the full archival data and the datasets in time intervals of two years. the full-time period comprises 18 years of H.E.S.S. data, from the beginning of the experiment until July 2022, the date this analysis started.

The H.E.S.S. data is treated as described in section 3.1.2; and three different types of full-time datasets are considered, based on different dataset preparation as mentioned in section 3.1.2. The datasets are here named conservative, standard, and nuisance datasets.

The conservative dataset assumes the official background model and the conservative low energy threshold. The standard dataset assumes the alternative background model, which has the muon efficiency bins in the model construction and the liberal low energy threshold. The nuisance dataset is the standard dataset with the nuisance parameter corrections to the background model. The nuisance dataset is set as the

* The data consider uses the HD calibration, configuration std_zeta_fullEnclosure, background model version v05_c.

main dataset for the analysis, for both 18 years and time bin analysis.

The time bin dataset assumes the same time edges as in *Fermi*-LAT analysis. Although each H.E.S.S. time bin dataset contains different statistics, for temporal correlation between the two experiments it is relevant to keep the same time period.

The analysis with a nuisance dataset uses a modified likelihood formula that takes into account nuisance parameters simultaneously during the fit procedure of the source spectrum. Since it is a new technique, not all products commonly obtained in a gamma-ray analysis are implemented with this technique, in particular the flux points and confidence contours.

As a temporary remedy to this issue, and only for purpose of comparison, the background in the dataset is corrected based on the nuisance parameters, and the flux points are calculated through the normal likelihood.

4.3.1 Data Selection

The data considered for the analysis comprises all H.E.S.S. runs with 4 telescopes, pointing direction within a radius of 0.7° from the Galactic Center, with a maximum zenith pointing direction of 60°. This is a total of 576 runs, equivalent to 260.4 hours over 18 years, and it constitutes the full dataset. The total detected events are shown in the skymap in figure 4.14.

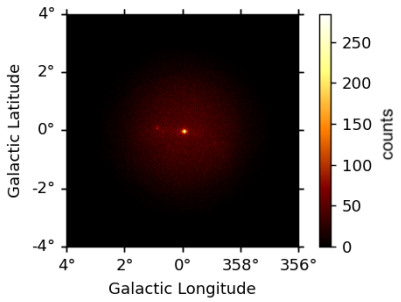

Figure 4.14: Stacked skymap of detected events for the full-time dataset.

Since H.E.S.S. is a pointing instrument, the observation of the central source must be scheduled and it is not necessarily constant over time or neither constant over the settings. Figure 4.15 presents the runs spread in time and zenith pointing direction for each time bin dataset and the 18 years dataset is composed of all of them.

Besides the zenith-pointing direction, the muon efficiency parameter of each run also strongly influences the data. Similar to figure 4.15, figure 4.16 shows the runs distribution over time.

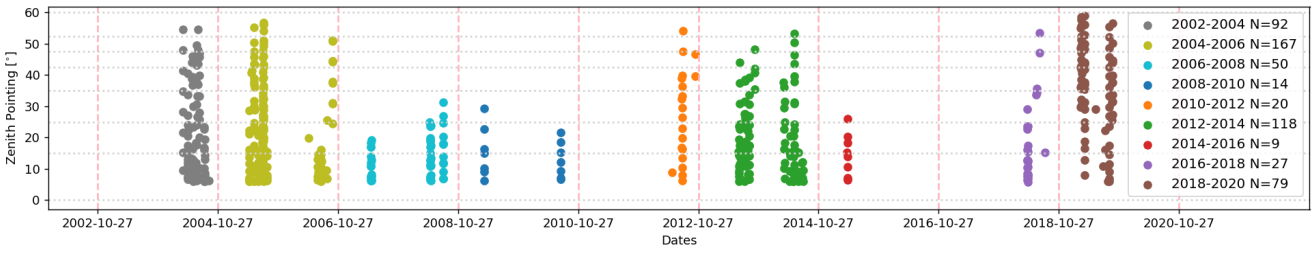

Figure 4.15: Runs distribution in time and zenith pointing direction. The different colors indicate the runs for each time bin dataset. The vertical light pink lines indicate the time bin edges, with N being the number of runs present in the specific dataset. The horizontal lines indicate the zenith bins of the background model.

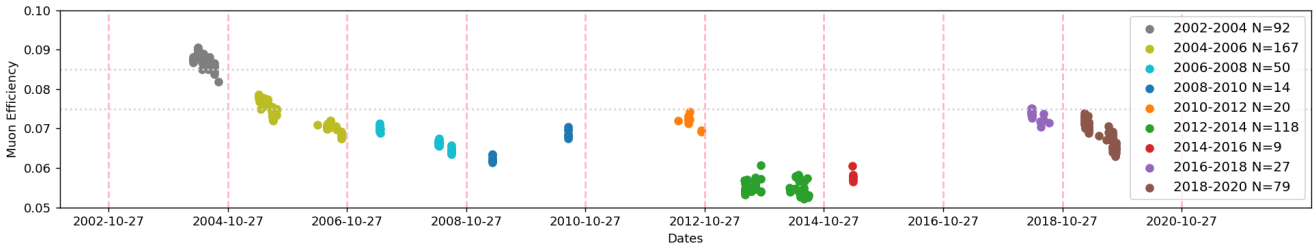

Figure 4.16: Run selection distribution with time and in muon efficiency parameter. The different colors indicate the runs for different time bins, and the full-time dataset uses the integral of all runs. The vertical light pink lines represent the time bin edges while the horizontal gray lines indicate the muon efficiency bin edges in the background model.

4.3.2 Assumed Models

The input models are divided into a central source, diffuse emission, neighboring sources from the catalog (HGPS [45]), and background from the gamma-like events.

The free parameters in the analysis are the spectral parameters of the central source, the diffuse emission, and the background model. The remaining parameters of input models are set as frozen contributions.

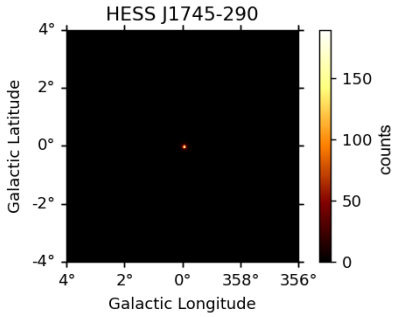

Figure 4.17: Expected gamma-ray events from the source HESS J1745–290. Considering 18 years of data.

The Central Source The source HESS J1745–290 is described as a point source located at (359.945°, -0.044°) in galactic coordinates, with an exponential cutoff spectral model defined as:

$$\phi(E) = \phi_0 \left(\frac{E}{E_0}\right)^{\Gamma} e^{-\lambda E}. \tag{4.4}$$

The parameters to be fitted are the amplitude ϕ_0, index Γ, and the cutoff λ. The expected number of events considering the 18 years dataset based on the catalog model is shown in the skymap in figure 4.17.

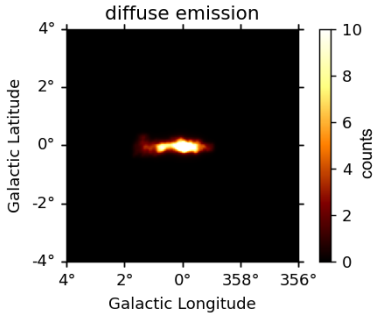

Figure 4.18: Gamma-ray events expected from the diffuse emission for the selected dataset. The color scale is saturated at 10 events to highlight also the weaker parts of the emission.

The Diffuse Emission The spatially extended diffuse emission from the Galactic Plane is also relevant in the H.E.S.S. range. In the classical IACT analysis, the diffuse emission is considered as part of the background, estimated by adaptive reflected regions. In this analysis, the diffuse emission is also considered a gamma-ray input model. It is worth highlighting that the 3D analysis of IACT data of the GC region with a 3D template diffuse emission is a novelty.

Similarly to the *Fermi*-LAT data, the diffuse emission is a 3D template model, developed by [113]. Since the emission from the central source overlaps spatially with the diffuse emission, its spectral parameters normalization and tilt are fitted. The sky map integrated in energy with the expected events from the diffuse emission to match the selected data is shown in figure 4.18.

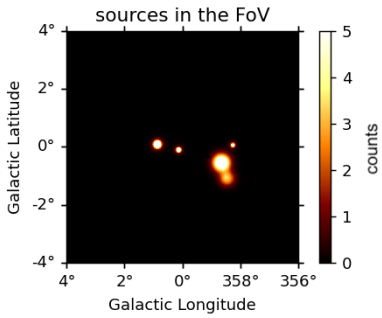

Figure 4.19: Skymap of expected counts from the neighboring sources. Map saturated at 5 so the weak sources are also visible.

Neighboring Sources For the considered FoV, 2.5° in radius, the neighboring sources described in the HGPS catalog are HESS J1741–302, HESS J1745–303, HESS J1746–285, HESS J1746–308, HESS J1747–281. They are included in the analysis as frozen contributions defined by the catalog model. An overview of the features of the sources is shown in table 4.3. The expected events from all neighboring sources for this analysis are shown in figure 4.19.

Table 4.3: Spatial and spectral characterization of the gamma-ray neighboring sources present in the studied FoV. The position is given in galactic coordinates, PS in extension stands for Point-Source and PL stands for Power-Law spectral model.

source	position (l,b)°	extension °	spectral model
HESS J1741–302	(358.28, 0.05)	PS	PL
HESS J1745–303	(358.71,-0.64)	0.179	PL
HESS J1746–285	(0.14,-0.11)	PS	PL
HESS J1746–308	(358.45,-1.11)	0.16	PL
HESS J1747–281	(0.87,0.08)	PS	PL

The Background Model The background from gamma-like events is estimated using a 3D background template model [48].

The different types of full-time datasets use different versions of the background model. The conservative dataset, uses the current official version[†], while the standard and nuisance datasets use the alternative model, constructed considering bins in muon efficiency axis. On top of that, the nuisance dataset has one more correction of the background estimation, using the nuisance parameters, which are fitted simultaneously with the source spectrum.

The background model is on a run-wise basis and must be estimated for each run to be further stacked in the *MapDataset*. Thus, a pre-treatment of the background model is done before performing the analysis. This step is named 'pre-fit' in section 3.1.2. The details of the dataset preparation are shown in the following section.

4.3.3 The Dataset Preparation

The dataset preparation consists of treating each run individually by selecting the safe range of the data and adjusting the background model to the data. It provides one *MapDataset* per run, which is stacked into a final *MapDataset*, comprising the information of all runs.

Although the analysis considers three different types of datasets, official, alternative, and nuisance, the alternative and nuisance datasets follow the same procedure in the dataset preparation.

The spatial geometry defined is the same for all datasets, with a radius of 2.5° deg from the run pointing position, and the source-free region is the white region shown in figure 4.20.

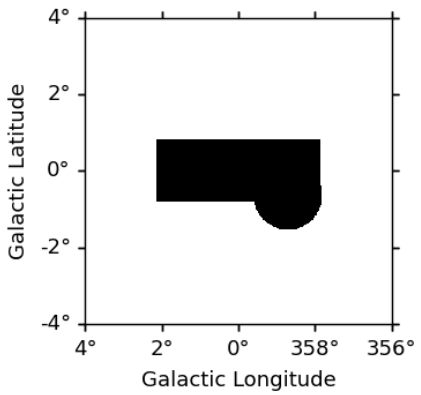

Figure 4.20: Source-free regions, shown as white in the sky map, used for pre-fit of the background model.

[†] For HESS internal communication, namely v_05c

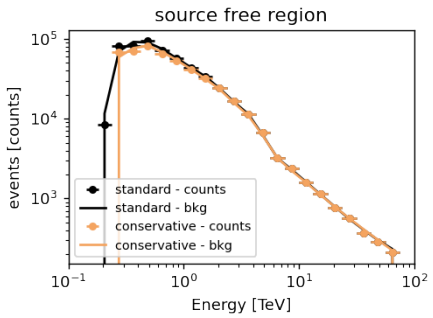

Figure 4.21: The dot points shows the selected events data as a function of energy for the different datasets, black for the standard/nuisance, and orange for the conservative dataset. The full line shows the expected background for the respective dataset. These results is integrated over the source-free region.

The energy range description follows the nomenclature defined in section 3.1.2. The official dataset assumes a conservative low energy threshold, with a value of 237 GeV. The standard and nuisance datasets assume a liberal low energy threshold, with a value of 178 GeV. It is worth highlighting that the same method for defining the low energy threshold (conservative or liberal) yields different energy values due to different run configurations, such as zenith pointing direction.

Considering the selected energy range and the source-free region, a background model is fitted to the run data, with spectral power-law normalization and tilt as free parameters. The outcome is the expected background events in each bin of the run *MapDataset*, which is stacked in the final *MapDataset*.

Finally, the final stacked dataset, one for the conservative and one for the standard/nuisance setting, comprises the selected events in the defined safe spatial and energy ranges. It also contains the expected background events for this amount of data. A comparison of the data in the conservative and standard datasets is shown in figure 4.21.

The consequence of different energy thresholds is visible as a discrepancy in the data in the low energy range, with more statistics for the standard dataset. Thus the main difference between the different datasets lies in how the low-energy data is treated, and an overview of it is presented in table 4.4.

Table 4.4: Overview of the main differences between the different datasets

feature	conservative	alternative	nuisance
lowest energy	value	value	value
high background systematic error present?	X	✓	✓
systematic error controlled?	X	X	✓

4.3.4 Spectral Analysis

The spectrum of HESS J1745–290 is calculated for the conservative, standard, and nuisance datasets and shown in figure 4.22. Although the spectra show different amplitude and index behavior, the cutoff energy agrees among the different datasets.

The best-fit parameters for these datasets are shown in figure 4.23. The index and λ parameters agree among the different datasets within the error bars. The amplitude presents considerable differences, being the highest for the catalog model and the nuisance dataset is 10% lower than it.

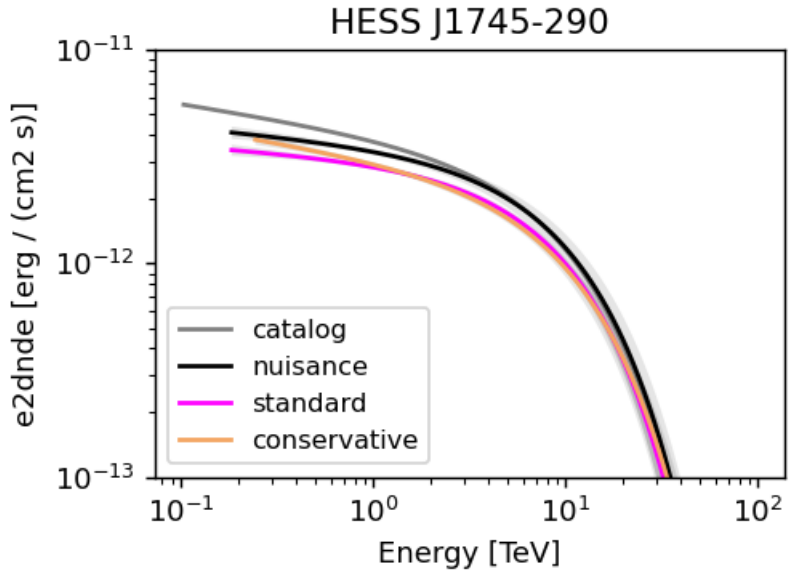

Figure 4.22: Spectrum for source HESS J1745–290 calculated for different datasets, nuisance dataset shown as the black line, standard dataset as magenta line, and conservative dataset as the orange line. The catalog spectrum is shown in gray for comparison. The uncertainty of each model is shown as a gray band enveloping the spectrum.

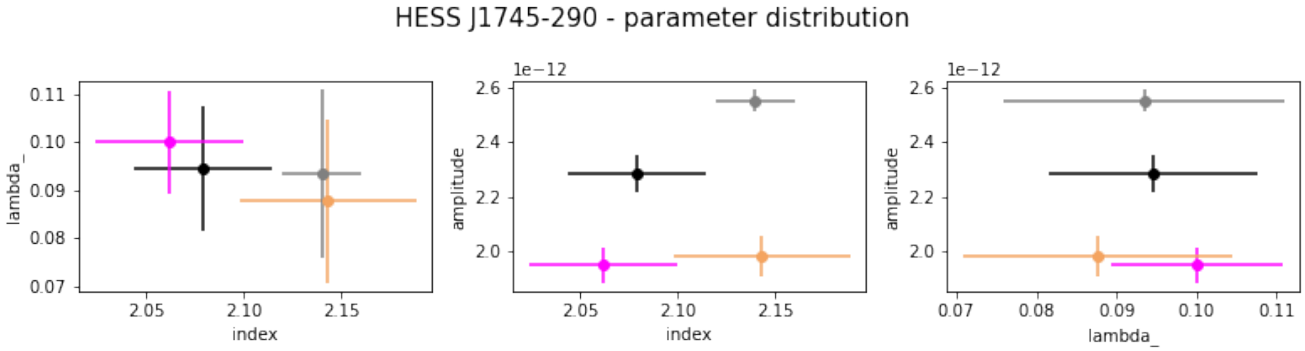

Figure 4.23: Fitted spectrum parameters for source HESS J1745–290 for the different datasets considered: gray - catalog values, black - nuisance method, magenta - standard dataset, and light orange - conservative dataset. The parameters are indicated in equation 4.4 as amplitude Φ_0, index as Γ and lambda_ as λ.

The highest amplitude for the catalog spectrum is explained by the different treatments of the diffuse emission. In the catalog analysis, the diffuse emission is obtained from adaptive reflected regions, thus the diffuse emission contribution at the source location is estimated from regions adjacent to the source in the same FoV. While in the 3D analysis, the diffuse emission is considered as a gamma-ray input model, with a 3D template shape, based on physical and multi-wavelength arguments. Thus, it models the entire region, including the source location.

The conservative, standard, and nuisance dataset assumes the same 3D template for the contribution of the diffuse emission and its normalization is a free parameter in each dataset. Figure 4.24 shows the correlation between the amplitude of the central source and the normalization of the diffuse emission for each dataset. This correlation is expected, due to the spatial overlap of the emissions. The higher the amplitude

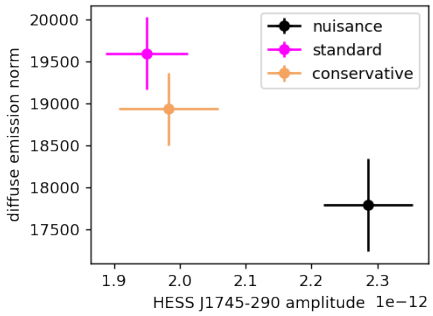

Figure 4.24: Diffuse emission amplitude and central source amplitude parameters distribution.

of the central source, the lower the normalization of the diffuse emission.

Although assuming the same template for the diffuse emission, the difference in the source amplitude is a consequence of the data at low energies. The comparison of the spectrum from the conservative/standard datasets shows the effect of excluding/including the low-energy data, which contains high levels of systematic errors in the background. The comparison of the spectrum standard/nuisance shows the improvement in uncontrolled/controlled systematic errors in the analysis. And finally, the comparison between conservative/nuisance shows the effect of using fewer statistics at the expense of no systematic error compared to more statistics and properly including the systematic errors of the background model.

Table 4.5: Best fit parameters for H.E.S.S. data, nuisance dataset of source HESS J1745–290 considering full time.

	HESS J1745–290	
parameter	catalog value	nuisance best fit values
ϕ_0 10^{-12}/(cm2 TeV s)	2.5500	2.29 +/- 0.067
Γ	2.14	2.079 +/- 0.04
λ 1/TeV	0.093458	0.095 +/- 0.01
E_0 TeV	1	1

From this point on, only the procedure assumed for the nuisance dataset is used in the analysis. The parameter values for the best-fit nuisance dataset and the catalog are shown in table 4.5.

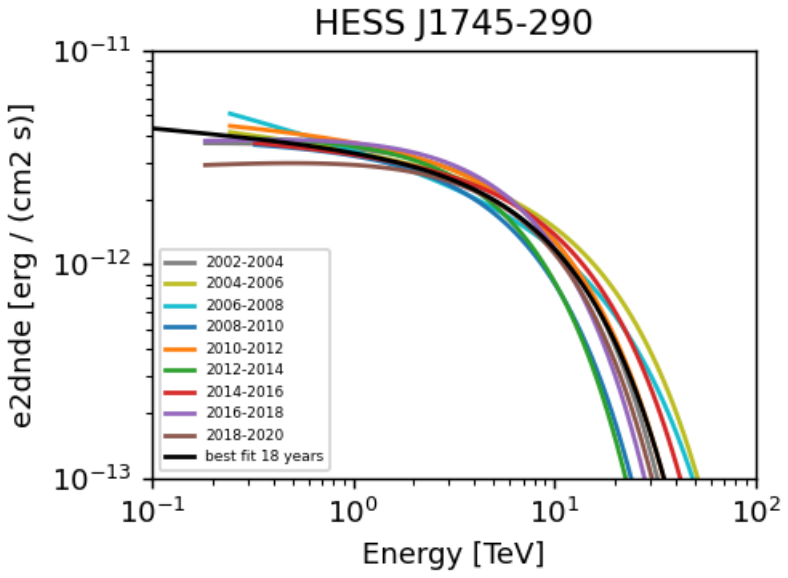

Figure 4.25: Fitted spectrum parameters for source HESS J1745–290 for the different time bins, the black spectrum shows the fulltime result for comparison.

For the time bin analysis, which also considers nuisance parameters, the diffuse emission parameter values are fixed to the best fit 18 years nuisance dataset. It is worth noting that in contrast to the LAT case, even fixing the external

gamma-ray input models, the different time bin datasets have different calibrations, settings, and statistics.

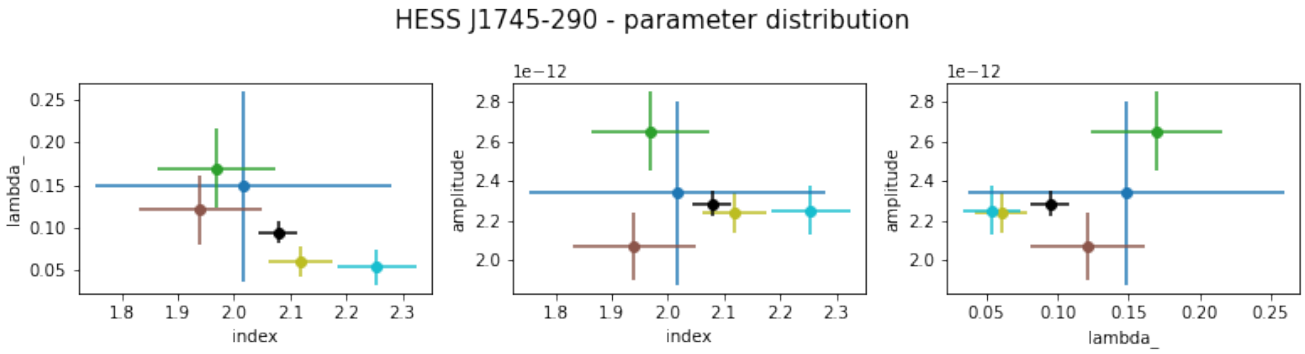

Figure 4.26: Fitted spectrum parameters for source HESS J1745–290 for the different time bins, the black spectrum shows the full-time result for comparison.

The spectrum for each time bin is presented in figure 4.25. Although the spectra are similar, interesting features stand out for some datasets. The 2004-2006 dataset presents a higher energy cutoff. The 2008-2012 and 2012-2014 datasets present the lowest energy cutoff. And finally, the 2018-2020 dataset presents a lower amplitude value. The not mentioned datasets yield spectra statistically equal to the 18 years dataset.

The distribution of the best-fit values for the most different spectra is shown in figure 4.26. The 2008-2012 dataset presents large uncertainties, due to the low number of runs present in the dataset, as shown in figure 4.15. The lambda parameter indicates the inverse of the cutoff energy. The cutoff energy is highest for the 2006-2008 dataset, with a value of 20 TeV, and the lowest for the 2012-2014 dataset of 5 TeV. The biggest amplitude variation is of order 11% positive for datasets 2012-2014 and 11% negative for the 2018-2020 dataset, compared to the best-fit full-time results.

4.3.5 Analysis Stability

Techinical Differences in the Time-bin Datasets Each time bin dataset is composed by a different amount of data, indicated by the number of runs N in figure 4.15. The smallest dataset, 2014-2016, contains 9 runs, followed by the 2008-2010, with 14 runs, while the largest dataset, 2004-2006, contains 167 runs. The lack of statistics in a dataset causes large uncertainties in the best-fit parameters, as observed for the 2008-2010 dataset in figure 4.26.

Additionally, each dataset has a different value of low energy threshold. Although they all have the lowest energy threshold possible, chosen following the liberal setting, its exact value change from dataset to dataset as shown in figure 4.27.

However, regardless of the threshold value, due to the nuisance parameters in the analysis, the systematic errors are under control.

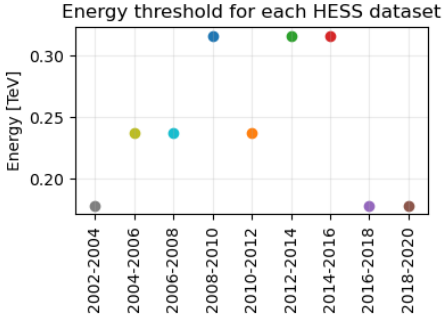

Figure 4.27: Fitted spectrum parameters for source HESS J1745–290 for the different time bins, the black spectrum shows the 18 years result for comparison.

Even after the correction of the systematic errors, differences in the spectra are still observed, as shown in figure 4.25.

Error Estimation for Nuisance Dataset The nuisance dataset is the standard dataset with the correction of the nuisance parameters. The systematic error for the standard dataset is estimated using the lookup tables and used as input values for the nuisance parameters. Then, the central source spectrum and the nuisance parameters are fitted simultaneously.

Figure 4.28 shows the error estimation for the different datasets with different procedures. The magenta and purple curves shows the systematic error for the standard dataset, estimated through different methods. The estimation of the error using the lookup tables, purple curve, is the input for the nuisance parameters analysis. The comparison of purple and black uses the same estimation for different datasets and highlights the improvement of the nuisance dataset over the standard one.

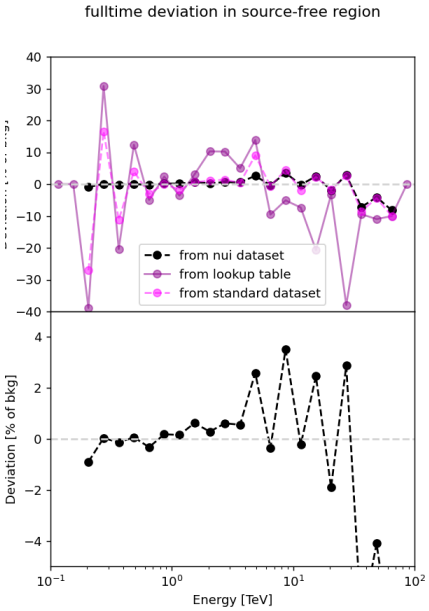

Figure 4.28: Systematic error estimation considering the source-free region. In the upper plot, the magenta data points show the estimation from the lookup tables, the purple points show the estimation using equation 3.4 calculated from the dataset itself, and the black points show the error estimation considering the same equation 3.4 calculated from the nuisance dataset. The bottom plot shows a zoom-in of the upper plot showing only the black points.

The standard dataset has systematic errors of the order of 30% of background in the first two energy bins, and it slowly decreases as the energy increases up to 1 TeV. At ~ 5 TeV 10% of systematic error is expected from lookup tables, which is also observed in the dataset. Above 10 TeV, the error estimation increases again, mainly due to the lack of statistics in these bins. After the correction of the nuisance parameters, as better observed from the bottom plot, the error due to the background model is less than 2% for the full-time dataset in the low energy range, highlighting the improvement this method brings to the analysis.

Similarly to the full-time dataset, the background systematic error is estimated for each time bin dataset from the lookup tables and implemented in the analysis. The error estimation from the lookup tables and the error estimation using the equation 3.4 for each time bin dataset is shown in the first column of figure B.4 in the appendix. A similar pattern as in the full-time analysis is observed. The systematic error is higher in the low energy range, reaching ~20% in some datasets, and it is drastically corrected by the nuisance parameters. Once again, due to the lack of statistics in the high energy range, the error estimation and the nuisance parameters do not present a major impact.

Significance Sky Maps Figure 4.29 shows the significance sky map integrated over the energy range for the different datasets. The standard and conservative plots show strong spatial patterns, not only coincidence with gamma-ray sources but also in source-free regions. For the nuisance dataset, the significance sky map presents a homogenous distribution, as is expected for a good model description of the data. The achieved homogeneity in the significance sky map highlights the power of this technique.

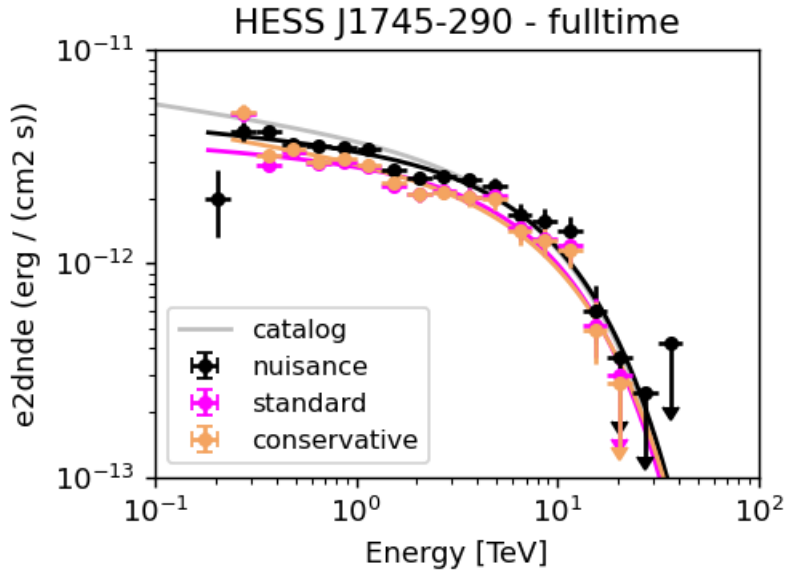

Figure 4.30: Flux points for the different HESS datasets: black for the nuisance dataset, pink for standard, and orange for conservative. For comparison, the spectrum from the catalog is shown in solid gray line.

For the time bin datasets, figure B.4 in the appendix shows in the third and fourth columns the significance maps for the standard and nuisance datasets respectively. Patterns in the sky map are observed for the standard datasets, although not necessarily the same across the different time bin datasets. This shows that systematic errors are not caused by a specific source nor even following the same pattern. Nevertheless, the nuisance parameter corrects these systematic errors, providing a better estimation of the background for the whole region, as shown through the homogenous distribution of significance in the sky maps of the fourth column.

Flux Points As previously mentioned, the flux points for the nuisance dataset are not yet fully implemented and the results for this dataset are a first approximation for the purpose of comparison only.

Figure 4.30 shows the flux points calculated for the different full-time datasets. In general, the obtained flux points present a step pattern for all datasets, which is caused by the gamma-hadron separation using BDT, a step before the 3D analysis, and therefore is not covered in this work. Another feature is the high value of the first flux point of the standard and conservative dataset, which is not within the error bars.

The nuisance dataset provides one more flux point at low energy and two more at high energy, although the safe energy range for standard and nuisance datasets is the same. The lowest energy bin for the standard dataset contains high systematic errors, of the order of 30% as shown in figure 4.28, and it is corrected in the nuisance dataset. This correction provides better modeling of the data in the nuisance dataset.

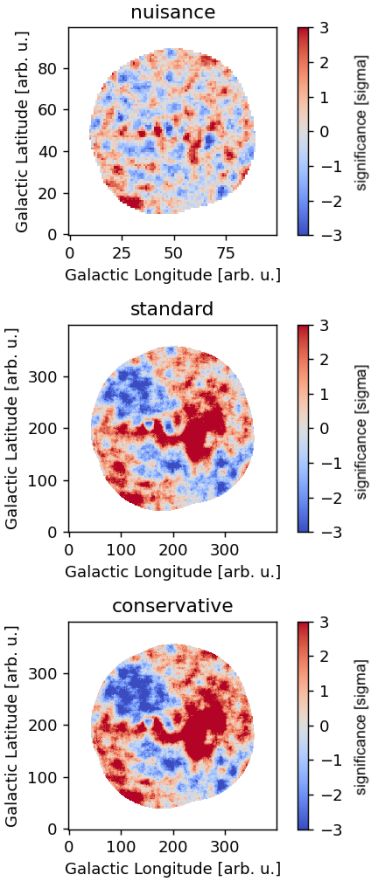

Figure 4.29: Significance sky map integrated in energy for the different datasets: nuisance, upper plot, standard, middle plot, and conservative, lower plot.

With a better description of the data, the fitting procedure computationally converges, enabling the estimation of flux points at such low energy.

The comparison of nuisance and standard datasets' flux points in each time bin is shown in figure 4.31. For the green dataset, there is no flux above 10 TeV, and as a consequence, this dataset presents a lower cut-off energy. The brown dataset presents an overall lower normalization of the flux points, indicating that the low amplitude obtained in the spectrum might not be caused by one bin error, as is the case for the blue dataset in LAT data. The yellow dataset is the only one presenting data above 40 TeV, in this case, an upper limit, resulting in a higher energy cutoff. The high statistics of the yellow dataset, 167 runs in total, support the robust results. In the light blue dataset, although it presents a high energy cutoff, many points are upper limits. This is probably an effect of the dataset being composed of many runs with low zenith pointing direction, which favors the low energy detection.

4.3.6 Discussion

Similar to the *Fermi*-LAT analysis section, from this point on, it is considered the spectral results from the time bin analysis are stable and reliable. Based on this assumption, the spectrum variability is investigated and consequently, the prediction from the astrophysical model [93] was examined.

Testing the Spectrum Stability over Time Figure 4.32 shows the results of the hypothesis tests considering the number of trial in the $\sqrt{\mathrm{TS}}$ calculation. The choice of the high energy range, shown as opaque data points, above 7 TeV, is chosen such that it does not include the systematic error above 5 TeV and it is lower than the cutoff energy for the full-time spectrum (~10 TeV).

The datasets presenting the highest values are the yellow, green, and brown datasets, as also pointed out in the previous tests. However, even for these datasets, no significant values of $\sqrt{\Delta\mathrm{TS}}$ are observed for the full energy range nor for the high energy range. Thus, the null hypothesis is still valid, meaning that the full-time spectrum can describe the time bin data within statistical fluctuations.

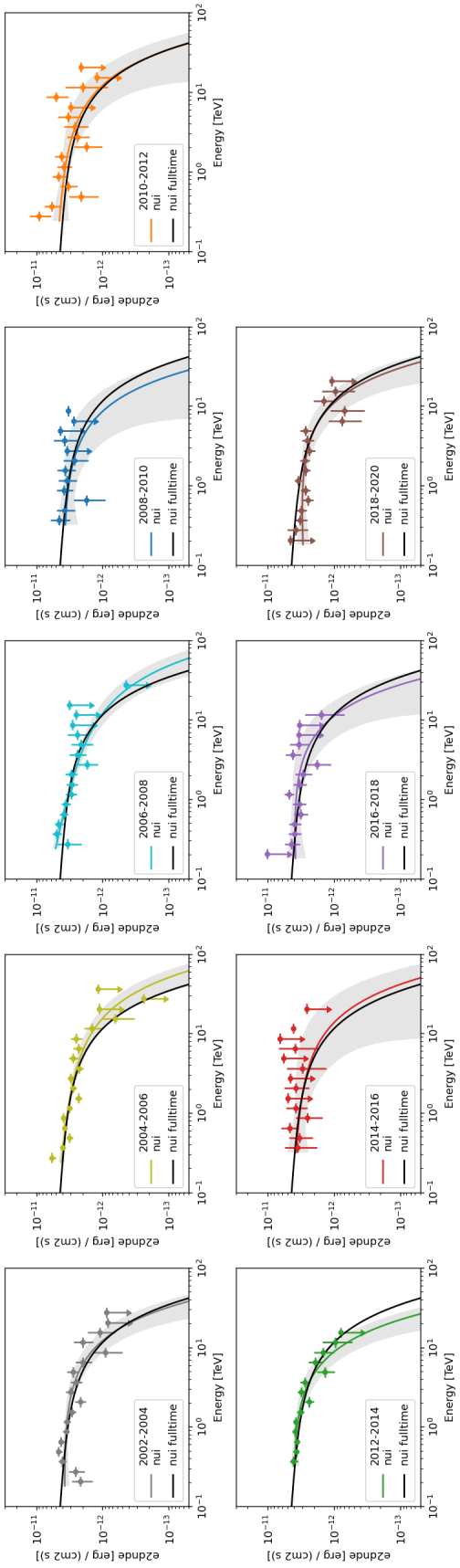

Figure 4.31: Flux points and the best-fit spectrum for each time bin nuisance dataset. The 18 years nuisance best-fit spectrum is shown for reference as the black line.

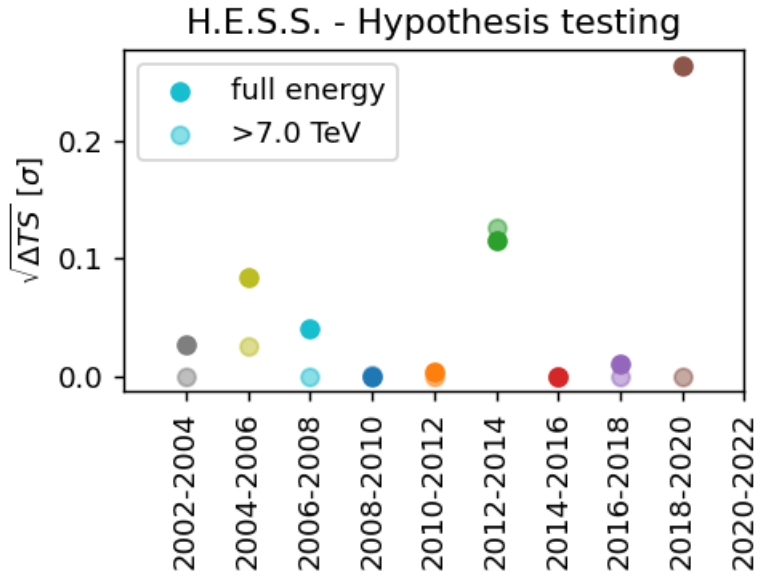

Figure 4.32: Calculation of $\sqrt{\text{TS}}$ using equations 4.1 and 4.2. The solid dots consider the full energy range, while the opaque dots shows the results considering energy above 7 TeV.

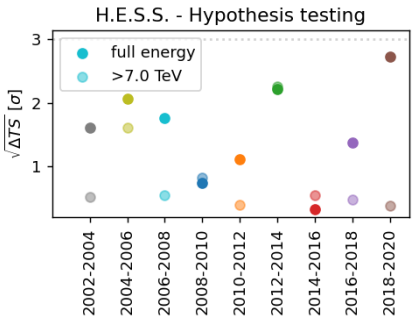

Figure 4.33: Similarly to figure 4.32 this plot shows the calculation of $\sqrt{\text{TS}}$, however, considering only equation 4.1.

The values of $\sqrt{\Delta \text{TS}}$ neglecting the number of trials is shown in figure 4.33. It does not indicate the correct result, but it is presented for purposes of comparison, highlighting the effect of the number of trials. Although the $\sqrt{\Delta \text{TS}}$ increases by neglecting the number of trials, it is still not significant to exclude the null hypothesis.

In conclusion, this result indicates that the emission from HESS J1745–290 is stable over time. It is in agreement with previous IACT works [81, 83, 82], although they considered a lower-time span.

Physical Model Testing The astrophysical model presented in [93] assumes energy-dependent propagation of protons injected due to burst episodes from Sgr A*, and predictions of variability for HESS J1745–290 spectrum. In this model, the gamma rays are produced due to the interaction of the protons during the escape from the Sgr A* accretion disk, in the range of 1 pc region[‡].

Different configurations of proton injection potentially resulting in the emission of HESS J1745–290 are investigated in [93]. Independent of the scenario proposed, a consequence of the energy-dependency in the proton propagation is that the low-energy protons require a longer diffusion time and therefore the gamma-ray emission for this energy band is delayed compared to the gamma rays due to the high-energy protons.

One hypothesis presented is a continuous injection. To match the data in the H.E.S.S. energy range, an injection of at least

[‡] The exact mechanisms of acceleration are not part of the investigation

10^4 years with a proton spectral index of 0.75 is expected. The minimum period of injection, 10^4 years, is the required time to reproduce 90% of the gamma-ray energy flux observed in the 0.1–1 TeV band. However, the same rate, 90% of the energy flux, is achieved within 10 years for the range 10-100 TeV. Thus, in this scenario, any variation in the injection rate of protons would be visible in the 10–100 TeV range after ~10 years.

Another scenario presented is one burst episode, injecting accelerated particles during 3–10 years, that ended ~ 10 years ago, with a proton injection index of 2.7. While the continuous injection model provides a better fit[§] to the H.E.S.S. spectrum from 2006, the burst injection model provides a proton spectral index value accordingly to the expected from particle acceleration mechanisms described in [114, 115]. The prediction within this scenario is a softening of the spectrum after ~ 5 years for the energy range above 10 TeV.

Another possible hypothesis is considering several burst episodes of proton injection. The prediction for this case is variations in the spectral index and cutoff energy on a few years-long time scales, based on the assumption that the bursts are unlikely to be identical.

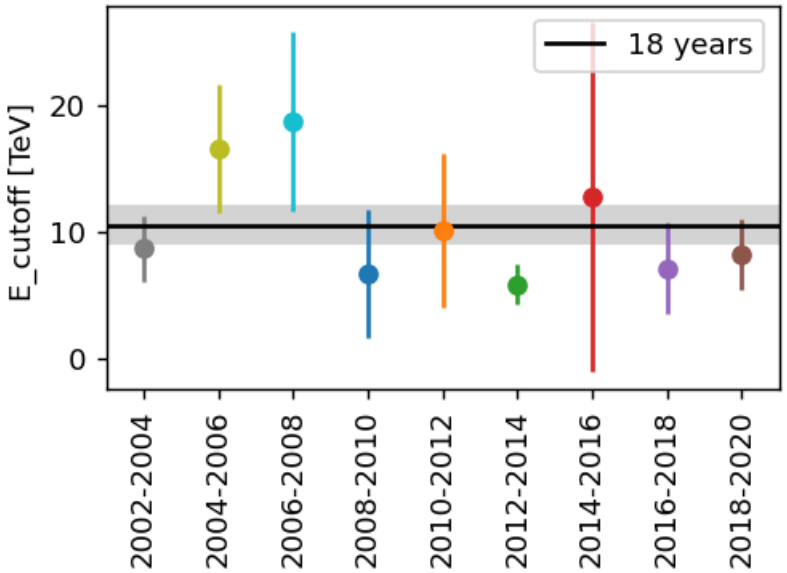

Figure 4.34: The energy cutoff from the spectrum of different time bin datasets for source HESS J1745–290. The constant black line and the gray band show the cutoff value and the uncertainty for the cutoff from the full-time spectrum.

However, the results of this work presented in figure 4.32 show that no statistically significant variation is observed in any time period. Additionally, the agreement on the cutoff energy in the different time periods with the 18 years cutoff energy, as presented in figure 4.34, evidences no significant variation in the spectrum above 10 TeV.

The spectral stability in the high energy tail of the central

[§] Comparison of χ^2 values presented in the paper.

source emission presented in this work indicates that emission from HESS J1745–290 is improbable to be due to (i) one burst episode of a few years duration occurring 10 years ago, since no gradual softening of the spectrum in time is observed; and it is improbable to be due to (ii) several bursts episodes since no significant variation in the cutoff energy is observed.

Assuming the hadronic scenario with energy dependency transport, this work supports the hypothesis of continuous emission or series of identical bursts occurring apart by <10 years, since this is the shortest time scale for a measurable variability.

4.4 Combined Analysis and Discussion

A combined analysis of the GeV and TeV emissions is attractive, especially due to the possibility of a common underlying astrophysical model. More specifically, the combination of LAT and H.E.S.S. data is interesting, since H.E.S.S. is the IACT with the highest sensitivity towards low energies for GC observations, due to its location in the Southern Hemisphere. On top of that, the technique presented in this work, by including the systematic errors through nuisance parameters, allows the usage of data of even lower energies, enabling a closer connection to LAT range.

To date, it is not clear whether GeV and TeV emissions share a common location or a common parent particle population. Although both emissions come from the GC, the region covered by source 4FGL J1745.6–2859 can be as large as 100 pc for the lowest energies, while for H.E.S.S. the source covers a region of the order of 6 pc. However, even in the improved resolution of H.E.S.S. copious processes are feasible resulting in a complex emission, in which the disentanglement is challenging.

Gammapy supports a joint fit of LAT and H.E.S.S. data. However, due to the high degeneracy among the astrophysical models, it is not the focus of this work.

To overcome these challenges, any hint of a correlation between the data from LAT and H.E.S.S. could guide in discriminating the process in the region. Figure 4.35 shows the full-time spectrum of both experiments, which comprises 14 for LAT and 18 years for H.E.S.S., obtained individually, overlapped with the flux points obtained in [23]. The discrepancy observed in the normalization of the spectrum for LAT data from [23] and this analysis result is a consequence of the different analysis procedure and more accumulate data. While [23] uses 6 years of LAT data, this analysis uses 14 years of data, a more complete catalog, improved IRFs, and a different version of the diffuse model.

Temporal analysis is one option to assist in discriminating between the various hypothesis, and if confirmed it is a strong

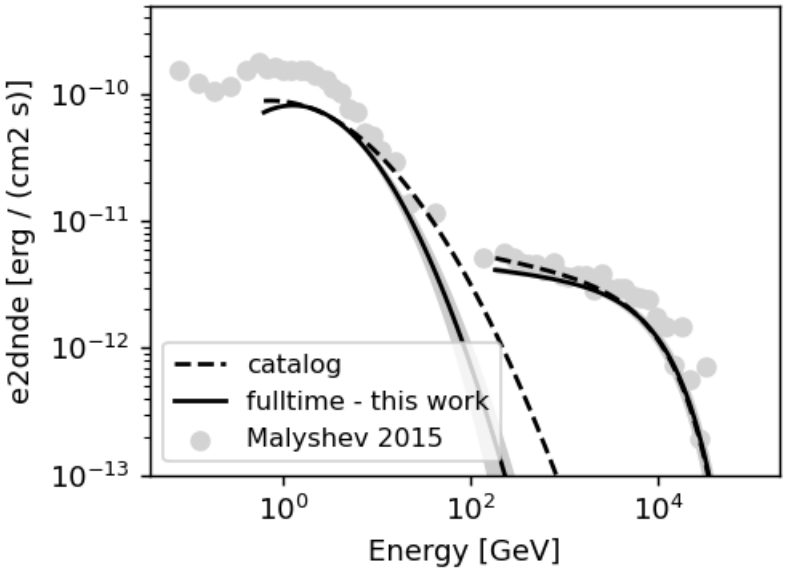

Figure 4.35: GC source spectrum for *Fermi*-LAT and H.E.S.S.. The solid black line shows the best-fit results for this work, the dashed black line shows the catalog values while the gray points show the flux points obtained in [23].

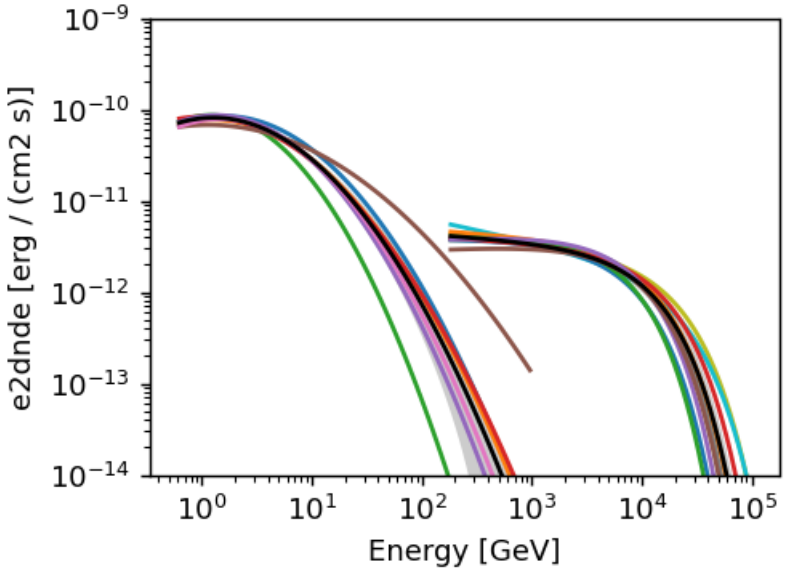

Figure 4.36: Energy spectrum for the different time bin datasets for *Fermi*-LAT and H.E.S.S..

advocate for flaring emission from Sgr A*. Figure 4.36 shows the combination of the LAT and H.E.S.S. spectra from each time bin dataset assumed in this analysis.

Although this work indicates a steady emission of the central source within the statistical fluctuation, the time periods with higher variation from the full-time spectrum are coincident for LAT and H.E.S.S., as shown in figure 4.37. These are the 2012-2014 and 2018-2020 datasets.

The behavior for the 2012-2014 dataset is similar for both experiments, a fading at higher energies compared to the full-

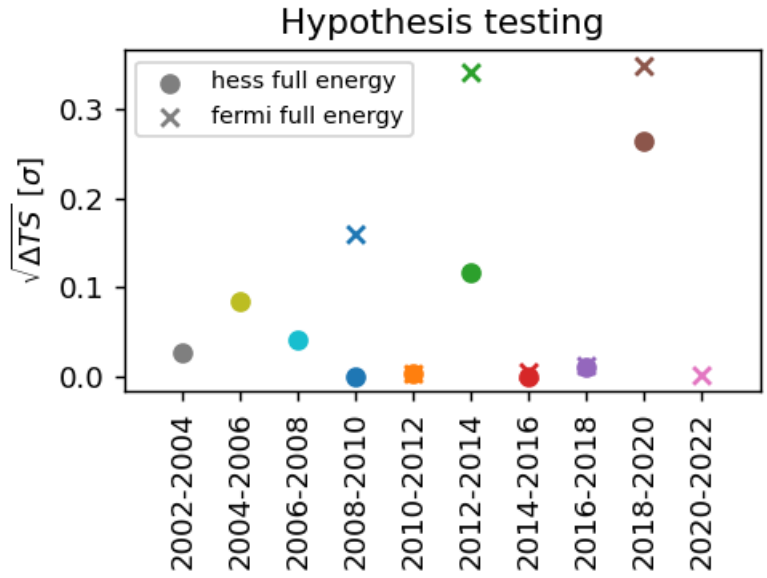

Figure 4.37: Hypothesis testing for *Fermi* and HESS including the nuisance parameters.

time spectrum. This time period coincides with the periastron of the G2 cloud around Sgr A*. However, with the available statistics, no correlation can be made between G2 and the small variation in the spectra from LAT and H.E.S.S..

For the 2018-2020 dataset, LAT data present data at higher energies, while HESS data present an overall lower normalization and low cutoff. No astrophysical object is known to be a possible candidate responsible for this behavior.

Coincident spectrum variability between the two experiments could indicate a common source of the emission of the GeV and TeV emission. As a prospect for future analysis, one possibility is spectrum variability investigation in a specific time period, defined by external visitors. With this approach, the number of trials is reduced, and as shown in the previous section, it strongly influences the values of $\sqrt{\Delta TS}$.

In summary, no statistically significant variation of the spectrum is observed, considering time interval of two years, over 14 years, and 18 years of Fermi-LAT and H.E.S.S. data. However, the time periods with the most extreme variation from the full-time spectrum are the same for LAT and HESS. Future experiments, with higher capabilities, might be able to disentangle the puzzle of the GeV-TeV emission from the Galactic Center.

4.5 Conclusions

The accumulated data of 14 years in the LAT energy range and 18 years for the H.E.S.S. energy range provide enough statistics for reliable spectrum variability investigation of the GeV-TeV emission from the GC central source. For this analysis, it is

used the maximum likelihood technique, with updated IRFs and diffuse emission models within gammapy.

The analysis of the H.E.S.S. data is performed in the framework presented in chapter 3.2, which includes the estimated systematic errors of the background model in the maximum likelihood computation of the best-fit parameters. This novel analysis shows that independent of the causes of the systematic error, using only the estimated level of it, better accuracy of the region is achieved, and the energy range is increased.

At the limit of the spatial and energy precision of the gamma-ray experiments, the discrimination of the astrophysical source is still unclear. The complexity of the region allows different astrophysical models to describe the physics of the GC region.

As an option, the investigation in time allows an increase in statistics with time, with not necessarily improvement in the instruments. If a spectrum variability in time for the H.E.S.S. data is observed, it is strong evidence for models supporting Sgr A* as an astrophysical source responsible for the emission, since the PWN G359.95–0.04 is expected to be constant in time. Additionally, if a coincident time variability is observed in both experiments, it indicates that the emission of 4FGL J1745.6–2859 and HESS J1745–290 are from the same astrophysical source, which up to now is not confirmed yet.

This work indicates that the spectrum of sources 4FGL J1745.6–2859 and HESS J1745–290 are stable over time. Also, due to the absence of variation, no claim on the correlation between the experiments can be made.

The spectrum invariability observed in LAT allows the exclusion of the model proposed by [23], in which the GeV emission is due to high energy electrons injected during a flaring episode from Sgr A* occurring 300 years ago and gradually cooling via IC. This model predicts flux variability in the 10-year time scale, and it is tested in this work. The absence of a trend in time of the energy flux, and the spectrum parameters contradicts this model.

The spectrum invariability in H.E.S.S. allows the exclusion of the hypothesis proposed by [93], which assumes flare episodes in which high energy protons are injected and accelerated in the accretion disk of Sgr A* and cooling down via p-p interaction with the matter field during the proton scape from GC. This model assumes energy-dependent proton transport, and as a consequence of this assumption, variation in the proton acceleration rate is visible in the time scales of 10 years for energies above 10 TeV. The highest energies of the H.E.S.S. spectrum require gamma-ray production mechanisms in short time scales, due to the strong cooling process. The spectrum invariability at these energies supports a continuous injection rather than flaring scenarios since it would be visible as spectrum variation above 10 TeV, as shown in [93].

The data analyzed in this work reaches the cooling time of the leptonic astrophysical model in the GeV range, and the hadronic model in the TeV range. In case of variation in the acceleration of the parent particle spectrum, for instance, due to a burst episode from Sgr A*, the accumulated data could potentially reveal such variation. Due to the high energy of H.E.S.S. data, the gamma-ray production must be recent and therefore, the stability of the cutoff is a strong indication of continuous injection of accelerated particles.

Conclusions 5

This work explored the capabilities of the 3D template background model by qualitatively and quantitatively estimating the level of systematic errors. Regardless of their causes, the error level is stored in lookup tables, which are used to calculate the error for any dataset and it is properly incorporated into the analysis through nuisance parameters. As a consequence, this framework affords a widening of the energy range towards low energies and a more accurate description of the background model, consequently improving the analysis results. Furthermore, this work also presents spectral variability studies of the Galactic Center central sources 4FGL J1745.6–2859 with *Fermi*-LAT and HESS J1745–290 with H.E.S.S., and for the latter source, the analysis includes the systematic errors of the background model.

The method estimates the error in systematic bins, in which the behavior of the bias caused by the error is expected to be the same. Each run in a systematic bin provides one deviation curve, which presents the level of mismatch between the data and the model, per energy bin and integrated over the source-free regions. The deviation curve includes statistical and systematic errors. The average of the deviation curves in one systematic bin yields the error curve, which corresponds to the systematic error level in the lookup tables. The averaging procedure decreases the statistical fluctuations intrinsic to the deviation curves. However, when there are only a few runs within a systematic bin the systematic errors cannot be disentangled from the statistical errors.

The error curves are calculated with two different units, the statistical standard deviation ([std]), and the percentage of the total background events ([% of bkg]). While the first one is useful when considering the number of runs available for the error estimation, the second one is practical for the calculation of the error in a dataset.

From the lookup tables, the systematic errors due to the background model in a dataset can be estimated and corrected in the analysis via nuisance parameters in the maximum likelihood calculation. The nuisance parameters, also in a 3D shape, are fitted simultaneously with the source of interest, yielding in the addition/subtraction of background events in each bin of the 3D dataset. The validation of the method is proved with a Crab dataset.

The two most prominent origins of the systematic error for this version are explored. The first one is due to the bad spatial modeling at low energies, which is intrinsic to the model construction and it is probable to be significant in other model versions. The second error is inherent to the studied version, due to the technique of Boosteded Decision Trees for

gamma/hadron separation; however, it highlights issues in previous steps in the pipeline that can potentially appear as errors in the background model. While the causes of systematic errors are version dependent the method developed for the estimation is model-independent and reproducible in any model version.

The analysis including the systematic errors of the background model was applied to the H.E.S.S. data in the Galactic Center region for spectral variability investigation of the central source, namely HESS J1745–290. Given the adjacent energy range and the common analysis method, data from the central source observed by *Fermi*-LAT, 4FGL J1745.6–2859, is also included in the study. The motivation for the spectral variability arose since the accumulated archival data in both experiments is large enough to test astrophysical models and coincident spectral variability between the two experiments could indicate a common origin of the two emissions.

The energy range explored in this work is 600 MeV–100 TeV, in which the gamma-ray spectrum is described by two components, a bump in the GeV range and a power law with an exponential cutoff at higher energies. This work obtains for each experiment, the spectrum considering the total archival data, which comprises 14 and 18 years of LAT and H.E.S.S. data. The 14 and 18 years spectra are compared to the spectrum obtained in two years time intervals for each experiment, using the hypothesis test method. The spectra obtained in the two years time interval in each experiment are within the statistical fluctuations of the 14 and 18 years spectrum. Thus, this work indicates a stable spectrum over 14 and 18 years of accumulated data of the central source spectrum.

The stability of the spectrum in this time scale allows the constraint on astrophysical models predicting spectrum variability. In the literature, there are two models describing the emission of the central source that are testable with the current lifetime of LAT and H.E.S.S. experiments due to the short predicted time scale variability.

The first model, proposed by [23] describes the GeV–TeV emission as a product of the cooling down of electrons via IC. The injection of particles has two components, both caused by Sgr A. The first one is a continuous injection responsible for the TeV emission, and the second one is due to a major burst that occurred 300 years ago, responsible for the GeV emission. The burst hypothesis is supported by measured echos from the burst in other wavelengths in neighboring sources. Spectral variability predicted in this model for the GeV component is a displacement of the GeV bump towards low energies due to the gradual cooling of the charged particles. Additionally, a decrease of 5–10% in the energy flux at 1–10 GeV is expected. However, given the stability of the spectrum, such variation expected as a trend in time of the spectrum parameters is not

observed. This rules out that the GeV emission is only due to a gradual IC cooling of electrons injected 300 years ago.

The second model, proposed by [93] explains the H.E.S.S. emission as a result of p-p cooling mechanism of protons from Sgr A* from a flaring episode of 3–5 years duration, which ended ~10 years ago, with an injection spectrum index of 2.7. This model matches the H.E.S.S. measurements from 2006. The basic assumption of the model is the energy dependency of the proton transport, which leads to faster cooling of the high-energy protons. The predicted time scales are such that the predicted time scales are of the order of ~ 10 years, which is testable with the current data. Thus, in case the rate of the accelerated protons presents a variation, it would result in an observable variation in the high-energy part of the gamma-ray spectrum. In this scenario, a prediction of variation in the spectrum above 10 TeV is expected in the time scales of ~5 years. Additional burst episodes hypothesis is also presented in this model, and they would be observed in the gamma-ray spectrum as variation in the spectral parameters since it is unlikely that the burst episodes are identical. However, the stability of the spectrum contradicts the hypothesis of one or several flaring episodes. Given the rapid cooling of the high-energy protons, variability in the cutoff would be measurable, however, the cutoff value of the gamma-ray spectrum is stable with time, favoring a continuous emission of accelerated particles.

The results of this analysis are within statistical fluctuations and no significant variation coincident in time between the experiments can be stated. The origin of the gamma-ray emission from the Galactic Center's central source is still a paradigm. Considering the spatial coordinates, there are different candidates responsible for the emission within the PSF of each instrument, hampering the coincidence of the spatial origin of each emission. Considering the time coordinate, on the other hand, no emission presented variability up to date. However, with the increase in statistics and higher precision of future instruments, like CTA, the mysteries of the GC region might be finally revealed.

Appendix

A

Lookup Tables for the Systematic Error Estimation

The comparison of different configurations for the systematic error estimation. Figure A.1 shows the comparison of the lookup tables for the different muon efficiency bins. It is noticeable that the high muon efficiency bin has an even lower energy threshold, although it has higher levels of error, it is controlled by the nuisance parameters. Therefore, the energy threshold of the analysis can be further decreased..

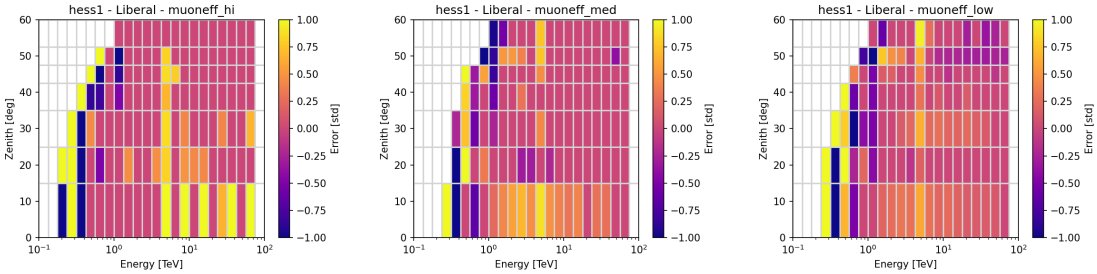

Figure A.1: Lookup tables for different configurations. The results are shown for H.E.S.S. I era, for the alternative model, for the liberal energy threshold. Each column is one muon efficiency bin.

Another interesting comparison between the different configurations is the alternative background model with a liberal energy threshold and the official model with a conservative energy threshold. The first one is the proposed setting used in this work the later one is the configuration used in the previous analysis with the 3D model. The error between these two configurations can be done by comparing the error curves from figures 3.28 and A.2.

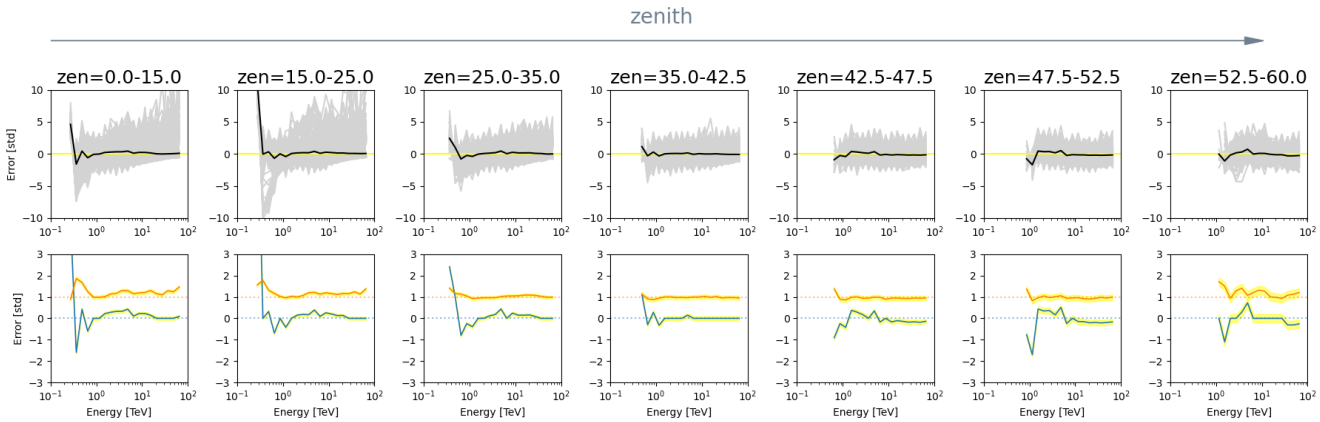

Figure A.2: The systematic error estimation for all zenith bin in H.E.S.S. 1 phase for the official model and conservative low energy threshold.

B

Time Bin Datasets Supplementary Plots for GC Dataset

Figure B.1 shows the significance map for the different time bins for LAT data. The confidence contours of the best-fit spectrum in each time bin dataset are shown in figure B.2.

Figures B.3 and B.4 shows the results for the H.E.S.S. time bin datasets. It is worth mentioning that the confidence contour is not performed for the nuisance dataset, but for the standard. Confidence contours are not yet implemented in the framework of the nuisance parameter analysis.

From figure B.4 it is observed that the deviation estimated from the lookup tables, dark magenta, agrees with the deviation estimated from the standard dataset. Moreover, after the correction of the nuisance parameters, using the estimated deviation from the lookup tables, solid colored line, the deviation decreases drastically presenting a better description of the background model. The improvement is observed especially in the low energy, and the highest energies for individual time bins might not have enough statistics for the nuisance parameters to be applicable. From the third column, the spatial pattern observed is different for each time bin dataset, indicating that the visible consequence of the systematic error of the background model is not constant over the runs. By comparing the last two columns, the improvement due to the nuisance parameter is visible by providing a uniform distribution of the significance sky map.

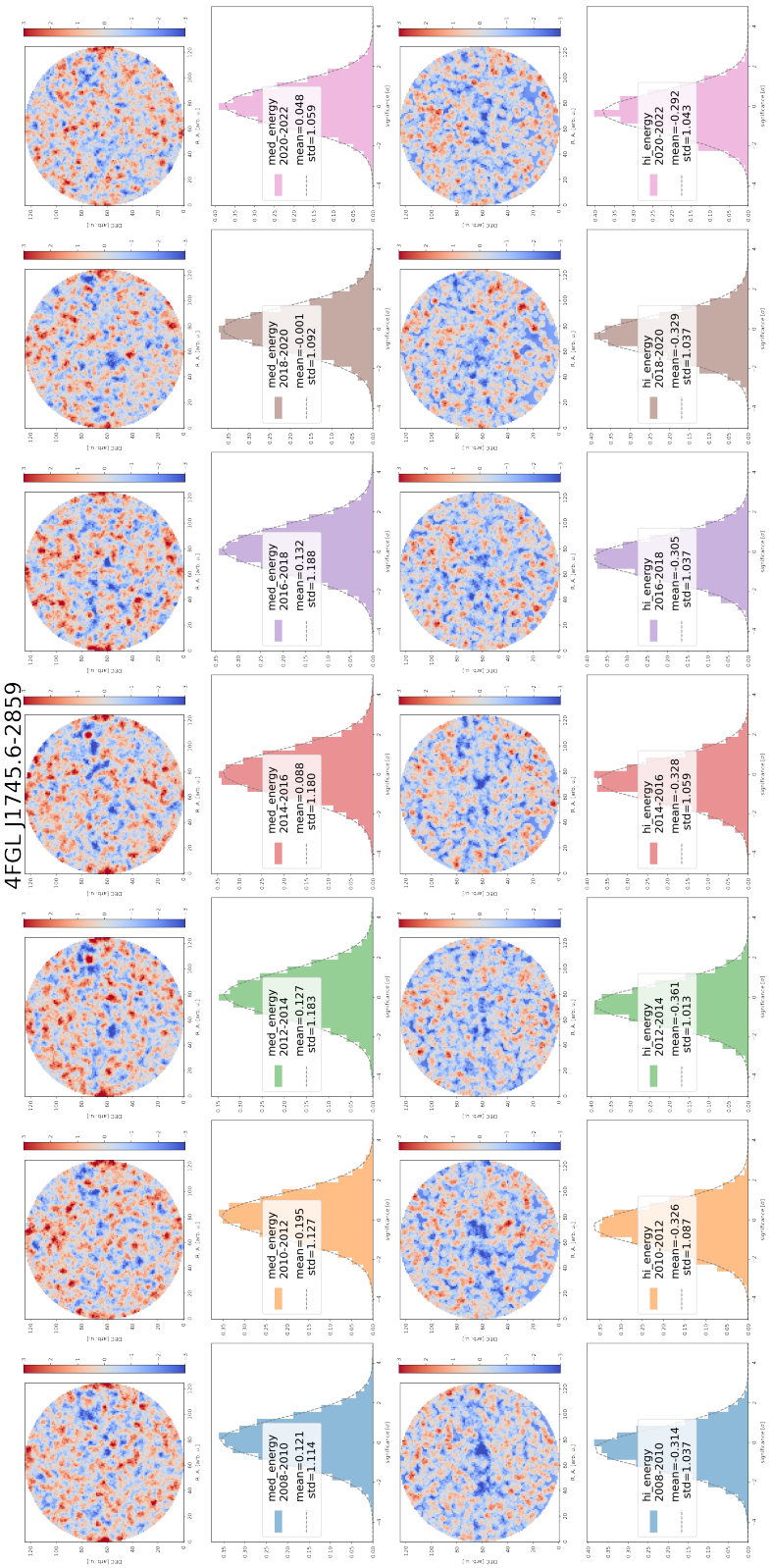

Figure B.1: Fermi-LAT significance skymap and distribution for different time bin datasets.

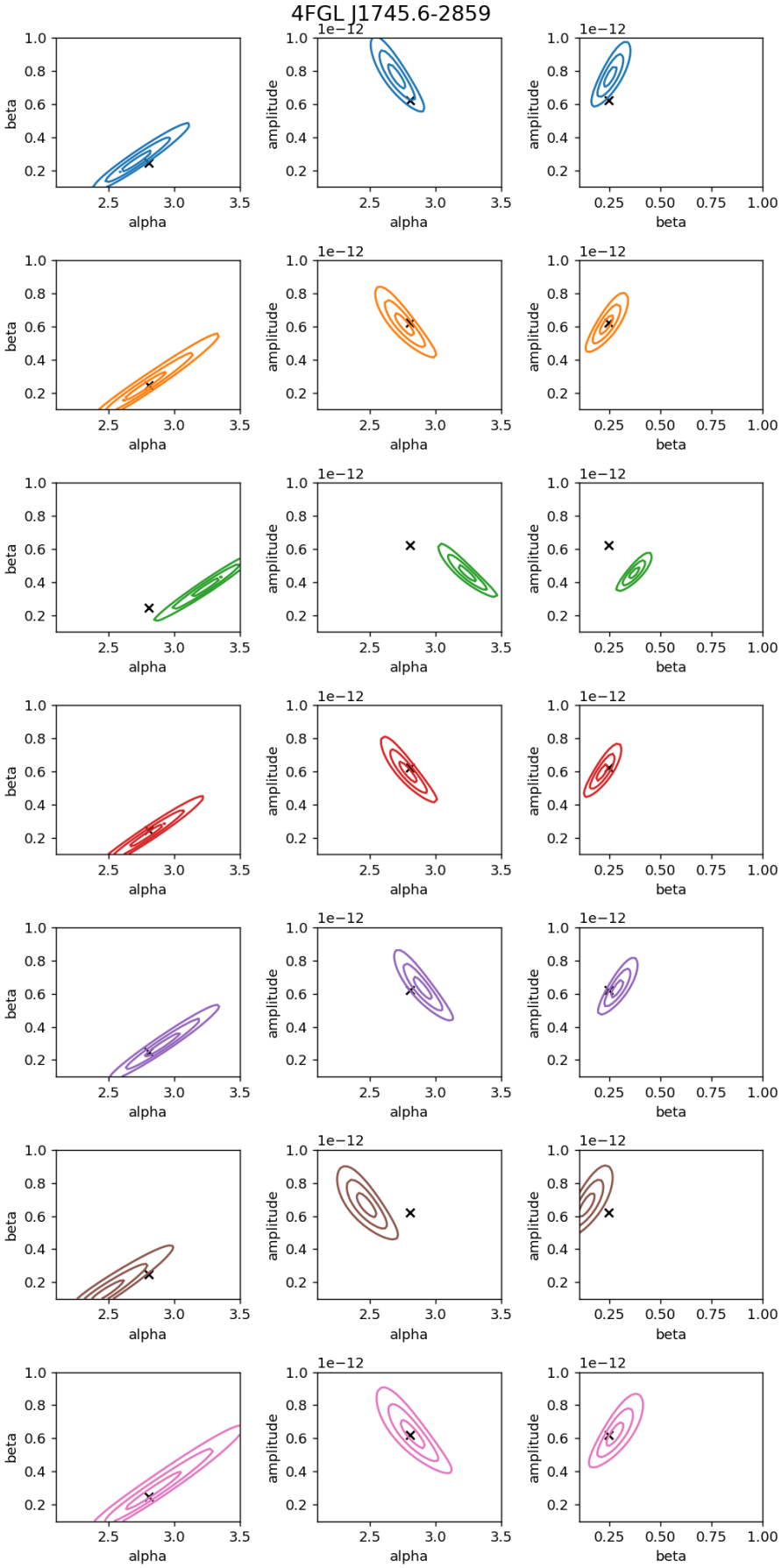

Figure B.2: Fermi-LAT confidence contour for different time bin datasets. The black cross shows the best fit values for the 14 years spectrum.

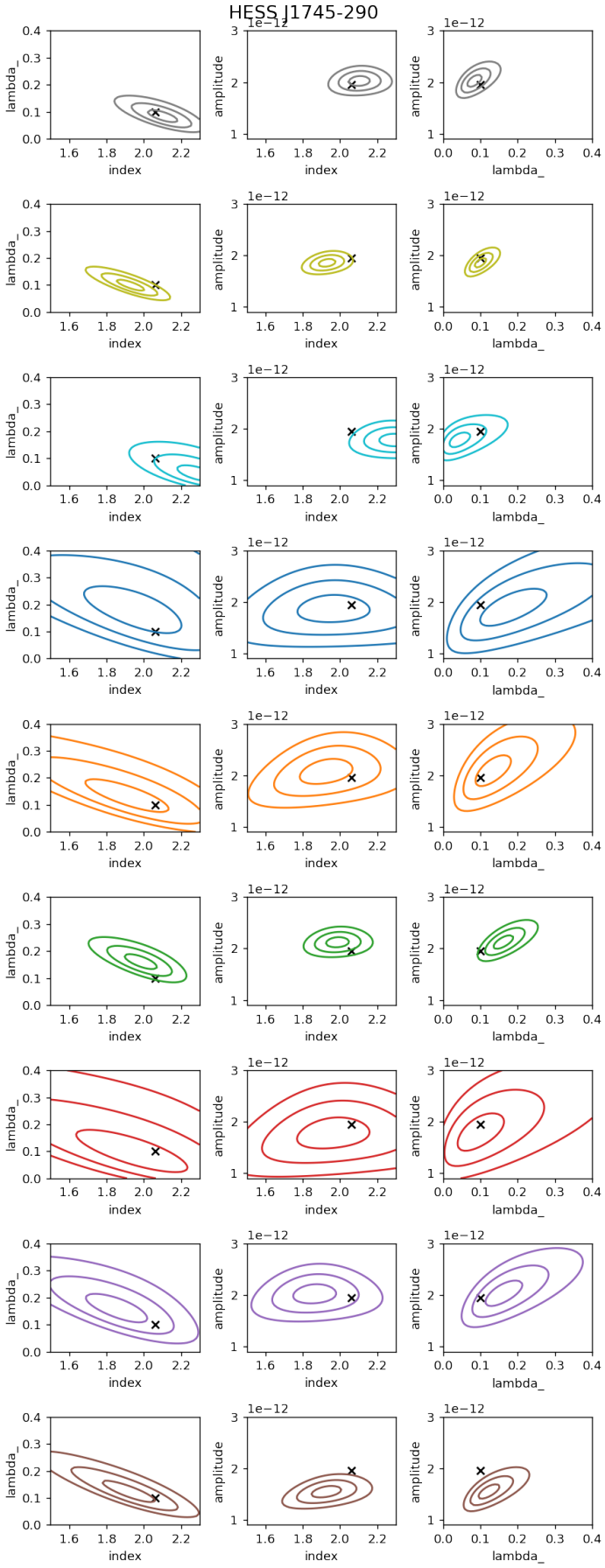

Figure B.3: Confidence contour for different time bin datasets considering the standard dataset.

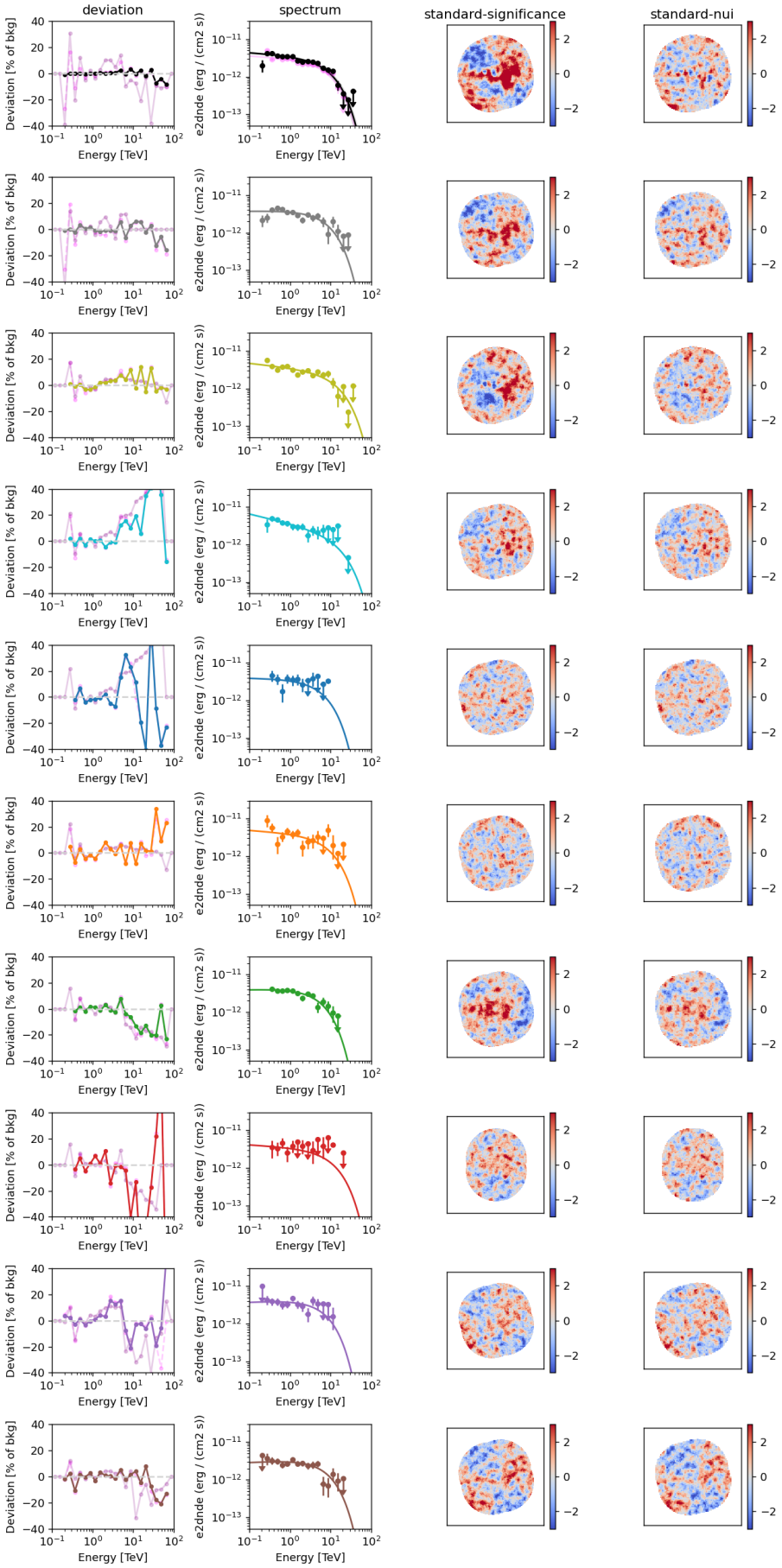

Figure B.4: The first presents the results for the 18 years dataset, and the following lines are the time bin datasets in chronological order. The first column shows the deviation of the dataset, in dark magenta is the expected deviation for the dataset calculated using the systematic error estimation method from chapter **??**, the magenta line shows the deviation calculated from the standard dataset and the black curve shows the deviation of the background and data after the nuisance parameters correction. This column follows the same pattern as shown in figure 4.28. The second column presents the best-fit spectrum for the nuisance dataset and its flux points. The third column presents the significance skymap for the standard dataset and the last column shows the significance skymap for the nuisance dataset, both integrated in the energy energy. This column follows the same pattern shown in figure 4.30.

Bibliography

[1] Zhen Cao et al. 'Ultrahigh-energy photons up to 1.4 petaelectronvolts from 12 -ray Galactic sources'. In: *Nature* 594 (7861 June 2021), pp. 33–36. DOI: 10.1038/s41586-021-03498-z (cited on pages 3, 8).

[2] W. L. Kraushaar and G. W. Clark. 'Search for Primary Cosmic Gamma Rays with the Satellite Explorer XI'. In: *Phys. Rev. Lett.* 8 (3 Feb. 1962), pp. 106–109. DOI: 10.1103/PhysRevLett.8.106 (cited on page 3).

[3] W. B. Atwood et al. 'THE LARGE AREA TELESCOPE ON THEiFERMI GAMMA-RAY SPACE TELESCOPE/iMISSION'. In: *The Astrophysical Journal* 697.2 (2009), pp. 1071–1102. DOI: 10.1088/0004-637x/697/2/1071 (cited on pages 3, 16–18).

[4] M. Meyer, D. Horns, and H.-S. Zechlin. 'The Crab Nebula as a standard candle in very high-energy astrophysics'. In: *Astronomy &amp Astrophysics* 523 (2010), A2. DOI: 10.1051/0004-6361/201014108 (cited on pages 4, 10, 32, 47).

[5] and Zhen Cao et al. 'Peta–electron volt gamma-ray emission from the Crab Nebula'. In: *Science* 373.6553 (2021), pp. 425–430. DOI: 10.1126/science.abg5137 (cited on pages 4, 17, 32).

[6] Humberto Martınez-Huerta, Rodrigo Guedes Lang, and Vitor de Souza. 'Lorentz Invariance Violation Tests in Astroparticle Physics'. In: *Symmetry* 12.8 (2020), p. 1232. DOI: 10.3390/sym12081232 (cited on page 4).

[7] H. Abdalla et al. 'The 2014 TeV iγ/i-Ray Flare of Mrk 501 Seen with H.E.S.S.: Temporal and Spectral Constraints on Lorentz Invariance Violation'. In: *The Astrophysical Journal* 870.2 (2019), p. 93. DOI: 10.3847/1538-4357/aaf1c4 (cited on page 4).

[8] Torsten Bringmann and Christoph Weniger. 'Gamma ray signals from dark matter: Concepts, status and prospects'. In: *Physics of the Dark Universe* 1.1 (2012). Next Decade in Dark Matter and Dark Energy, pp. 194–217. DOI: https://doi.org/10.1016/j.dark.2012.10.005 (cited on pages 4, 6).

[9] Stefan Funk. 'Indirect detection of dark matter with γ rays'. In: *Proceedings of the National Academy of Sciences* 112.40 (2015), pp. 12264–12271. DOI: 10.1073/pnas.1308728111 (cited on page 4).

[10] B. P. Abbott et al. 'GW170817: Observation of Gravitational Waves from a Binary Neutron Star Inspiral'. In: *Physical Review Letters* 119.16 (2017). DOI: 10.1103/physrevlett.119.161101 (cited on page 4).

[11] M. G. Aartsen et al. 'Multimessenger observations of a flaring blazar coincident with high-energy neutrino IceCube-170922A'. In: *Science* 361.6398 (2018), eaat1378. DOI: 10.1126/science.aat1378 (cited on page 4).

[12] Jim Hinton and Edna Ruiz-Velasco. 'Multi-messenger astronomy with very-high-energy gamma-ray observations'. In: *Journal of Physics: Conference Series* 1468.1 (2020), p. 012096. DOI: 10.1088/1742-6596/1468/1/012096 (cited on page 4).

[13] Felix A. Aharonian. *Very high energy cosmic gamma radiation : a crucial window on the extreme Universe*. 2004 (cited on pages 6, 11, 21, 22).

[14] GEORGE R. BLUMENTHAL and ROBERT J. GOULD. 'Bremsstrahlung, Synchrotron Radiation, and Compton Scattering of High-Energy Electrons Traversing Dilute Gases'. In: *Rev. Mod. Phys.* 42 (2 Apr. 1970), pp. 237–270. DOI: 10.1103/RevModPhys.42.237 (cited on pages 6, 7, 13).

[15] Malcolm S. Longair. *High Energy Astrophysics*. 3rd ed. Cambridge University Press, 2011 (cited on page 6).

[16] D. N. Page and S. W. Hawking. 'Gamma rays from primordial black holes.' In: 206 (1976), pp. 1–7. DOI: 10.1086/154350 (cited on page 6).

[17] Stefan Funk. 'Ground- and Space-Based Gamma-Ray Astronomy'. In: *Annual Review of Nuclear and Particle Science* 65.1 (2015), pp. 245–277. DOI: 10.1146/annurev-nucl-102014-022036 (cited on pages 9, 12–15).

[18] R. L. Workman et al. 'Review of Particle Physics'. In: *PTEP* 2022 (2022), p. 083C01. DOI: 10.1093/ptep/ptac097 (cited on page 10).

[19] Stephen L. Adler. 'Axial-Vector Vertex in Spinor Electrodynamics'. In: *Phys. Rev.* 177 (5 Jan. 1969), pp. 2426–2438. DOI: 10.1103/PhysRev.177.2426 (cited on page 11).

[20] John Stewart Bell and Roman Jackiw. 'A PCAC puzzle: $\pi 0 \to \gamma\ \gamma$ in the σ-model'. In: *Il Nuovo Cimento A (1965-1970)* 60 (1969), pp. 47–61 (cited on page 11).

[21] F. W. Stecker. 'The Cosmic γ-Ray Spectrum from Secondary Particle Production in Cosmic-Ray Interactions'. In: 6.3 (Mar. 1970), pp. 377–389. DOI: 10.1007/BF00653856 (cited on page 12).

[22] M. Chernyakova et al. 'THE HIGH-ENERGY, ARCMINUTE-SCALE GALACTIC CENTER GAMMA-RAY SOURCE'. In: *The Astrophysical Journal* 726.2 (2010), p. 60. DOI: 10.1088/0004-637x/726/2/60 (cited on pages 12, 33, 35).

[23] D. Malyshev et al. 'Leptonic origin of the 100 MeViγ/i-ray emission from the Galactic centre'. In: *Astronomy &amp Astrophysics* 582 (2015), A11. DOI: 10.1051/0004-6361/201526120 (cited on pages 12, 33, 35, 81, 82, 92–94, 108, 109, 111, 114).

[24] W. Galbraith and J. V. Jelley. 'Light Pulses from the Night Sky associated with Cosmic Rays'. In: 171.4347 (1953), pp. 349–350. DOI: 10.1038/171349a0 (cited on page 16).

[25] T. C. Weekes et al. 'Observation of TeV Gamma Rays from the Crab Nebula Using the Atmospheric Cerenkov Imaging Technique'. In: 342 (1989), p. 379. DOI: 10.1086/167599 (cited on page 16).

[26] G. Bosia et al. 'Observation of Structure in Čerenkov Pulses from Extensive Air Showers using Fast Techniques'. In: 225.5232 (1970), pp. 532–533. DOI: 10.1038/225532a0 (cited on page 16).

[27] F. Aharonian et al. 'Observations of the Crab nebula with HESS'. In: *Astronomy &amp Astrophysics* 457.3 (2006), pp. 899–915. DOI: 10.1051/0004-6361:20065351 (cited on pages 16, 20, 23, 47).

[28] J. Holder et al. 'The first VERITAS telescope'. In: *Astroparticle Physics* 25.6 (2006), pp. 391–401. DOI: https://doi.org/10.1016/j.astropartphys.2006.04.002 (cited on page 16).

[29] J. Aleksić et al. 'Performance of the MAGIC stereo system obtained with Crab Nebula data'. In: *Astroparticle Physics* 35.7 (2012), pp. 435–448. DOI: https://doi.org/10.1016/j.astropartphys.2011.11.007 (cited on pages 17, 47).

[30] A. U. Abeysekara et al. 'Observation of the Crab Nebula with the HAWC Gamma-Ray Observatory'. In: *The Astrophysical Journal* 843.1 (2017), p. 39. DOI: 10.3847/1538-4357/aa7555 (cited on page 17).

[31] M. Ackermann et al. 'THE iFERMI/i LARGE AREA TELESCOPE ON ORBIT: EVENT CLASSIFICATION, INSTRUMENT RESPONSE FUNCTIONS, AND CALIBRATION'. In: *The Astrophysical Journal Supplement Series* 203.1 (2012), p. 4. DOI: 10.1088/0067-0049/203/1/4 (cited on page 18).

[32] S. Abdollahi et al. 'iFermi/i Large Area Telescope Fourth Source Catalog'. In: *The Astrophysical Journal Supplement Series* 247.1 (2020), p. 33. DOI: 10.3847/1538-4365/ab6bcb (cited on pages 18, 31).

[33] A. M. Hillas. 'Cerenkov Light Images of EAS Produced by Primary Gamma Rays and by Nuclei'. In: *19th International Cosmic Ray Conference (ICRC19), Volume 3*. Vol. 3. International Cosmic Ray Conference. Aug. 1985, p. 445 (cited on page 21).

[34] J. Matthews. 'A Heitler model of extensive air showers'. In: *Astroparticle Physics* 22.5 (2005), pp. 387–397. DOI: https://doi.org/10.1016/j.astropartphys.2004.09.003 (cited on page 21).

[35] A M Hillas and J R Patterson. 'Characteristics and brightness of Cerenkov shower images for gamma-ray astronomy near 1 TeV'. In: *Journal of Physics G: Nuclear and Particle Physics* 16.8 (1990), p. 1271. DOI: 10.1088/0954-3899/16/8/022 (cited on page 22).

[36] A. Mitchell. 'Optical Efficiency Calibration for Inhomogeneous IACT Arrays and a Detailed Study of the Highly Extended Pulsar Wind Nebula HESS J1825-137'. PhD thesis. Karl-Ruprecht University, Heidelberg, Germany, 2016 (cited on pages 22, 24).

[37] Pierre Brun. 'Seeking particle dark matter in the TeV sky'. In: *AIP Conference Proceedings*. AIP, 2012. DOI: 10.1063/1.4732717 (cited on page 22).

[38] Konrad Bernlöhr. 'Impact of atmospheric parameters on the atmospheric Cherenkov technique'. In: *Astroparticle Physics* 12.4 (2000), pp. 255–268. DOI: 10.1016/s0927-6505(99)00093-6 (cited on page 22).

[39] *Science with the Cherenkov Telescope Array*. WORLD SCIENTIFIC, 2018 (cited on page 22).

[40] F. Aharonian et al. 'Calibration of cameras of the H.E.S.S. detector'. In: *Astropart. Phys.* 22 (2004), pp. 109–125. DOI: 10.1016/j.astropartphys.2004.06.006 (cited on page 23).

[41] J.A Hinton. 'The status of the HESS project'. In: *New Astronomy Reviews* 48.5-6 (2004), pp. 331–337. DOI: 10.1016/j.newar.2003.12.004 (cited on page 23).

[42] 'H.E.S.S. contributions to the 28th international cosmic ray conference'. In: *28th International Cosmic Ray Conference*. July 2003 (cited on page 23).

[43] H.E.S.S. Collaboration. *H.E.S.S. First Public Test Data Release*. en. 2018. DOI: 10.5281/ZENODO.1421098. URL: https://zenodo.org/record/1421098 (cited on pages 24, 94).

[44] D. Berge, S. Funk, and J. Hinton. 'Background modelling in very-high-energy iγ/i-rayastronomy'. In: *Astronomy &amp Astrophysics* 466.3 (2007), pp. 1219–1229. DOI: 10.1051/0004-6361:20066674 (cited on pages 24–26).

[45] and H. Abdalla et al. 'The H.E.S.S. Galactic plane survey'. In: *Astronomy &amp Astrophysics* 612 (2018), A1. DOI: 10.1051/0004-6361/201732098 (cited on pages 24, 31, 47, 96).

[46] C. Deil et al. 'Gammapy - A prototype for the CTA science tools'. In: *35th International Cosmic Ray Conference (ICRC2017)*. Vol. 301. International Cosmic Ray Conference. Jan. 2017, 766, p. 766 (cited on pages 24, 26, 39).

[47] S. Ohm, C. van Eldik, and K. Egberts. 'γ/hadron separation in very-high-energy mml:math xmlns:mml="http://www.w3.org/1998/Math/Mat altimg="si34.gif" overflow="scroll"mml:mrowmml:miγ/mml:mi/mml:mrow/mml:math-ray astronomy using a multivariate analysis method'. In: *Astroparticle Physics* 31.5 (2009), pp. 383–391. DOI: 10.1016/j.astropartphys.2009.04.001 (cited on pages 25, 39).

[48] Lars Mohrmann et al. 'Validation of open-source science tools and background model construction in γ-ray astronomy'. In: *Astron. Astrophys.* 632 (2019), A72. DOI: 10.1051/0004-6361/201936452 (cited on pages 25, 26, 38, 39, 97).

[49] J. Knödlseder et al. 'GammaLib and ctools'. In: *Astronomy &amp Astrophysics* 593 (2016), A1. DOI: 10.1051/0004-6361/201628822 (cited on pages 26, 39).

[50] Y. Maeda et al. 'A Chandra Study of Sagittarius A East: A Supernova Remnant Regulating the Activity of Our Galactic Center?' In: *The Astrophysical Journal* 570 (2 May 2002), pp. 671–687. DOI: 10.1086/339773 (cited on page 28).

[51] Attila Abramowski et al. 'Time-dependent absorption of very high-energy gamma-rays from the Galactic center by pair-production'. In: *American Institute of Physics Conference Series*. Ed. by Felix A. Aharonian, Werner Hofmann, and Frank Rieger. Vol. 1085. American Institute of Physics Conference Series. Dec. 2008, pp. 368–371. DOI: 10.1063/1.3076683 (cited on pages 28, 30).

[52] Christopher van Eldik. 'Gamma rays from the Galactic Centre region: A review'. In: *Astroparticle Physics* 71 (2015), pp. 45–70. DOI: https://doi.org/10.1016/j.astropartphys.2015.05.002 (cited on page 28).

[53] Q. D. Wang, F. J. Lu, and E. V. Gotthelf. 'G359.95-0.04: an energetic pulsar candidate near Sgr A*'. In: *Monthly Notices of the Royal Astronomical Society* 367.3 (Apr. 2006), pp. 937–944. DOI: 10.1111/j.1365-2966.2006.09998.x (cited on pages 28–30).

[54] Kazunori Akiyama et al. 'First Sagittarius A* Event Horizon Telescope Results. I. The Shadow of the Supermassive Black Hole in the Center of the Milky Way'. In: *The Astrophysical Journal Letters* 930 (2 May 2022), p. L12. DOI: 10.3847/2041-8213/ac6674 (cited on pages 28, 29).

[55] Karl M. Menten et al. 'The Position of Sagittarius A*: Accurate Alignment of the Radio and Infrared Reference Frames at the Galactic Center'. In: *The Astrophysical Journal* 475.2 (1997), p. L111. DOI: 10.1086/310472 (cited on page 28).

[56] A. Eckart et al. 'High Angular Resolution Spectroscopic and Polarimetric Imaging of the Galactic Center in the Near-Infrared'. In: 445 (May 1995), p. L23. DOI: 10.1086/187880 (cited on page 28).

[57] GRAVITY Collaboration et al. 'A geometric distance measurement to the Galactic center black hole with 0.3% uncertainty'. In: 625, L10 (May 2019), p. L10. DOI: 10.1051/0004-6361/201935656 (cited on page 28).

[58] M. J. Reid and A. Brunthaler. 'The Proper Motion of Sagittarius A*. III. The Case for a Supermassive Black Hole'. In: 892.1, 39 (Mar. 2020), p. 39. DOI: 10.3847/1538-4357/ab76cd (cited on page 28).

[59] B. Balick and R.L. Brown. 'Intense sub-arcsecond structure in the galactic center'. In: *Astrophysical Journal* 194 (2 1974), pp. 265–270 (cited on page 28).

[60] B. Balick and R. L. Brown. 'Intense sub-arcsecond structure in the galactic center.' In: 194 (Dec. 1974), pp. 265–270. DOI: 10.1086/153242 (cited on page 28).

[61] K. Y. Lo et al. 'On the size of the galactic centre compact radio source: diameter <20 AU'. In: 315.6015 (May 1985), pp. 124–126. DOI: 10.1038/315124a0 (cited on page 28).

[62] Reinhard Genzel, Frank Eisenhauer, and Stefan Gillessen. 'The Galactic Center massive black hole and nuclear star cluster'. In: *Reviews of Modern Physics* 82.4 (2010), pp. 3121–3195. DOI: 10.1103/revmodphys.82.3121 (cited on page 29).

[63] J. A. Hinton and F. A. Aharonian. 'Inverse Compton Scenarios for the TeV Gamma-Ray Emission of the Galactic Center'. In: *The Astrophysical Journal* 657.1 (2007), pp. 302–307. DOI: 10.1086/510283 (cited on pages 29, 35).

[64] A. M. Ghez et al. 'The accelerations of stars orbiting the Milky Way's central black hole'. In: 407.6802 (Sept. 2000), pp. 349–351. DOI: 10.1038/35030032 (cited on page 30).

[65] A. M. Ghez et al. 'High Proper-Motion Stars in the Vicinity of Sagittarius A*: Evidence for a Supermassive Black Hole at the Center of Our Galaxy'. In: 509.2 (Dec. 1998), pp. 678–686. DOI: 10.1086/306528 (cited on page 30).

[66] Heino Falcke et al. 'The Simultaneous Spectrum of Sagittarius A* from 20 Centimeters to 1 Millimeter and the Nature of the Millimeter Excess'. In: 499.2 (May 1998), pp. 731–734. DOI: 10.1086/305687 (cited on page 30).

[67] Tuan Do et al. 'Relativistic redshift of the star S0-2 orbiting the Galactic Center supermassive black hole'. In: *Science* 365.6454 (Aug. 2019), pp. 664–668. DOI: 10.1126/science.aav8137 (cited on page 30).

[68] P. M. Plewa et al. 'The Post-pericenter Evolution of the Galactic Center Source G2'. In: 840.1, 50 (May 2017), p. 50. DOI: 10.3847/1538-4357/aa6e00 (cited on page 30).

[69] Geoffrey C. Bower et al. 'Radio and Millimeter Monitoring of Sgr A*: Spectrum, Variability, and Constraints on the G2 Encounter'. In: *Astrophys. J.* 802.1 (2015), p. 69. DOI: 10.1088/0004-637X/802/1/69 (cited on page 30).

[70] S. Gillessen et al. 'A gas cloud on its way towards the supermassive black hole at the Galactic Centre'. In: 481.7379 (Jan. 2012), pp. 51–54. DOI: 10.1038/nature10652 (cited on page 30).

[71] M. Mościbrodzka et al. 'The Galactic Center Weather Forecast'. In: 752.1, L1 (June 2012), p. L1. DOI: 10.1088/2041-8205/752/1/L1 (cited on page 30).

[72] E. Mossoux et al. 'Multiwavelength study of the flaring activity of Sagittarius A in 2014 February-April'. In: 589, A116 (May 2016), A116. DOI: 10.1051/0004-6361/201527554 (cited on page 30).

[73] Élie Bouffard et al. 'No Sign of G2's Encounter Affecting Sgr A*'s X-Ray Flaring Rate from Chandra Observations'. In: *The Astrophysical Journal* 884.2 (2019), p. 148. DOI: 10.3847/1538-4357/ab4266 (cited on page 30).

[74] Helen Poon. 'H.E.S.S. observations of Sgr A*'. PhD thesis. Heidelberg: Ruprecht-Karls-Universität, 2016. DOI: 10.17617/2.2306970 (cited on page 30).

[75] M. L. Ahnen et al. 'Observations of Sagittarius A* during the pericenter passage of the G2 object with MAGIC'. In: 601, A33 (May 2017), A33. DOI: 10.1051/0004-6361/201629355 (cited on page 30).

[76] K. Kosack et al. 'TeV Gamma-Ray Observations of the Galactic Center'. In: *The Astrophysical Journal* 608.2 (2004), pp. L97–L100. DOI: 10.1086/422469 (cited on page 30).

[77] K. Tsuchiya et al. 'Detection of Sub-TeV Gamma Rays from the Galactic Center Direction by CANGAROO-II'. In: *The Astrophysical Journal* 606.2 (2004), pp. L115–L118. DOI: 10.1086/421292 (cited on page 30).

[78] F. Aharonian et al. 'Very high-energy gamma rays from the direction of Sagittarius A*'. In: *Astron. Astrophys.* 425 (2004), pp. L13–L17. DOI: 10.1051/0004-6361:200400055 (cited on page 30).

[79] J. Albert et al. 'Observation of Gamma Rays from the Galactic Center with the MAGIC Telescope'. In: *The Astrophysical Journal* 638.2 (2006), pp. L101–L104. DOI: 10.1086/501164 (cited on page 30).

[80] A. Archer et al. 'Very-high Energy Observations of the Galactic Center Region by VERITAS in 2010-2012'. In: 790.2, 149 (Aug. 2014), p. 149. DOI: 10.1088/0004-637X/790/2/149 (cited on page 30).

[81] F. Aharonian et al. 'Spectrum and variability of the Galactic center VHE γ-ray source HESS J1745-290'. In: 503.3 (Sept. 2009), pp. 817–825. DOI: 10.1051/0004-6361/200811569 (cited on pages 30, 32, 106).

[82] C. B. Adams et al. 'VERITAS Observations of the Galactic Center Region at Multi-TeV Gamma-Ray Energies'. In: *Astrophys. J.* 913.2 (2021), p. 115. DOI: 10.3847/1538-4357/abf926 (cited on pages 30, 31, 106).

[83] V. A. Acciari et al. 'MAGIC observations of the diffuse γ-ray emission in the vicinity of the Galactic center'. In: *Astron. Astrophys.* 642 (2020), A190. DOI: 10.1051/0004-6361/201936896 (cited on pages 30, 106).

[84] F. Aharonian et al. 'Discovery of very-high-energy γ-rays from the Galactic Centre ridge'. In: 439.7077 (Feb. 2006), pp. 695–698. DOI: 10.1038/nature04467 (cited on page 31).

[85] HESS Collaboration et al. 'Acceleration of petaelectronvolt protons in the Galactic Centre'. In: 531.7595 (Mar. 2016), pp. 476–479. DOI: 10.1038/nature17147 (cited on pages 31, 33).

[86] Fabio Cafardo and Rodrigo Nemmen. 'Fermi-LAT Observations of Sagittarius A*: Imaging Analysis'. In: *Astrophys. J.* 918.1 (2021), p. 30. DOI: 10.3847/1538-4357/ac0efe (cited on pages 31, 32).

[87] L Rolland. 'Spectrum and variability of the VHE Galactic Centre source observed with H.E.S.S.' In: (2005) (cited on page 32).

[88] F. Acero et al. 'Localizing the VHE γ-ray source at the Galactic Centre'. In: 402.3 (Mar. 2010), pp. 1877–1882. DOI: 10.1111/j.1365-2966.2009.16014.x (cited on page 32).

[89] S. Funk et al. 'The GeV-TeV Connection in Galactic gamma-ray Sources'. In: *Astrophys. J.* 679 (2008), pp. 1299–1314. DOI: 10.1086/587129 (cited on page 32).

[90] Silvia Celli, Andrea Palladino, and Francesco Vissani. 'Neutrinos and γ -rays from the Galactic Center Region after H.E.S.S. multi-TeV measurements'. In: *European Physical Journal C* 77.2, 66 (Feb. 2017), p. 66. DOI: 10.1140/epjc/s10052-017-4635-x (cited on page 33).

[91] A. Albert et al. 'Combined search for neutrinos from dark matter self-annihilation in the Galactic Center with ANTARES and IceCube'. In: 102.8, 082002 (Oct. 2020), p. 082002. DOI: 10.1103/PhysRevD.102.082002 (cited on page 33).

[92] F. Aharonian et al. 'Simultaneous HESS and Chandra observations of Sagitarius A^{star} during an X-ray flare'. In: 492.1 (Dec. 2008), pp. L25–L28. DOI: 10.1051/0004-6361:200810912 (cited on page 33).

[93] D. R. Ballantyne, M. Schumann, and B. Ford. 'Modelling the time-dependence of the TeV γ-ray source at the Galactic Centre'. In: 410.3 (Jan. 2011), pp. 1521–1526. DOI: 10.1111/j.1365-2966.2010.17533.x (cited on pages 33, 35, 81, 82, 104, 106, 111, 115).

[94] A. Viana et al. 'The Cherenkov Telescope Array view of the Galactic Center region'. In: *36th International Cosmic Ray Conference (ICRC2019)*. Vol. 36. International Cosmic Ray Conference. July 2019, 817, p. 817. DOI: 10.22323/1.358.0817 (cited on page 34).

[95] Armen Atoyan and Charles D. Dermer. 'TeV Emission from the Galactic Center Black Hole Plerion'. In: *The Astrophysical Journal* 617.2 (2004), p. L123. DOI: 10.1086/427390 (cited on page 35).

[96] F. Aharonian and A. Neronov. 'High-Energy Gamma Rays from the Massive Black Hole in the Galactic Center'. In: 619.1 (Jan. 2005), pp. 306–313. DOI: 10.1086/426426 (cited on page 35).

[97] Tim Linden, Elizabeth Lovegrove, and Stefano Profumo. 'The Morphology of Hadronic Emission Models for the Gamma-Ray Source at the Galactic Center'. In: 753.1, 41 (July 2012), p. 41. DOI: 10.1088/0004-637X/753/1/41 (cited on page 35).

[98] M. Fatuzzo and F. Melia. 'Diffusive Cosmic-Ray Acceleration in Sagittarius A*'. In: 757.1, L16 (Sept. 2012), p. L16. DOI: 10.1088/2041-8205/757/1/L16 (cited on page 35).

[99] Masaaki Kusunose and Fumio Takahara. 'A Leptonic Model of Steady High-energy Gamma-Ray Emission from Sgr A*'. In: 748.1, 34 (Mar. 2012), p. 34. DOI: 10.1088/0004-637X/748/1/34 (cited on page 35).

[100] Yi-Qing Guo et al. 'A hybrid model of GeV-TeV gamma ray emission from the Galactic center'. In: *Journal of Physics G Nuclear Physics* 40.6, 065201 (June 2013), p. 065201. DOI: 10.1088/0954-3899/40/6/065201 (cited on page 35).

[101] F. Yusef-Zadeh et al. 'Interacting Cosmic Rays with Molecular Clouds: A Bremsstrahlung Origin of Diffuse High-energy Emission from the Inner 2°×1° of the Galactic Center'. In: 762.1, 33 (Jan. 2013), p. 33. DOI: 10.1088/0004-637X/762/1/33 (cited on page 35).

[102] Matthew D. Kistler. 'Gamma Rays, Electrons, Hard X-Rays, and the Central Parsec of the Milky Way'. In: (Nov. 2015) (cited on page 35).

[103] M. Holler et al. 'A Run-Wise Simulation and Analysis Framework for Imaging Atmospheric Cherenkov Telescope Arrays'. In: *Astropart. Phys.* 123 (2020), p. 102491. DOI: 10.1016/j.astropartphys.2020.102491 (cited on page 37).

[104] Andreas Specovius. 'A new analysis of the PeVatron candidate HESS J1646-458 using a novel analysis technique'. doctoralthesis. Friedrich-Alexander-Universität Erlangen-Nürnberg (FAU), 2021, p. 133 (cited on pages 37, 62, 63).

[105] Fabio Acero et al. *Gammapy: Python toolbox for gamma-ray astronomy*. Version 1.0. If you use this software, please cite it using the metadata from this file. Nov. 2022. DOI: 10.5281/zenodo.7311399 (cited on page 39).

[106] F. A. Aharonian et al. 'The Energy Spectrum of TEV Gamma Rays from the Crab Nebula as Measured by the HEGRA System of Imaging Air Cerenkov Telescopes'. In: 539.1 (Aug. 2000), pp. 317–324. DOI: 10.1086/309225 (cited on page 47).

[107] F. Acero et al. 'Fermi Large Area Telescope Third Source Catalog'. In: 218.2, 23 (June 2015), p. 23. DOI: 10.1088/0067-0049/218/2/23 (cited on page 47).

[108] A. Acharyya et al. 'Sensitivity of the Cherenkov Telescope Array to a dark matter signal from the Galactic centre'. In: *Journal of Cosmology and Astroparticle Physics* 2021.01 (2021), pp. 057–057. DOI: 10.1088/1475-7516/2021/01/057 (cited on page 70).

[109] Katrin Streil. 'Maximum Likelihood Method Study Including Systematic Errors of Instrument Response Functions in Gamma-ray Astronomy'. PhD thesis. Friedrich-alexander-Universitaet, in preparation (cited on page 72).

[110] Eilam Gross and Ofer Vitells. 'Trial factors for the look elsewhere effect in high energy physics'. In: *European Physical Journal C* 70.1-2 (Nov. 2010), pp. 525–530. DOI: 10.1140/epjc/s10052-010-1470-8 (cited on page 83).

[111] Georgios Choudalakis. 'On hypothesis testing, trials factor, hypertests and the BumpHunter'. In: *arXiv e-prints*, arXiv:1101.0390 (Jan. 2011), arXiv:1101.0390. DOI: 10.48550/arXiv.1101.0390 (cited on pages 83, 92).

[112] M. Wood et al. 'Fermipy: An open-source Python package for analysis of Fermi-LAT Data'. In: *35th International Cosmic Ray Conference (ICRC2017)*. Vol. 301. International Cosmic Ray Conference. July 2017, 824, p. 824. DOI: 10.22323/1.301.0824 (cited on page 83).

[113] Yu Wun Wong. 'Diffuse Gamma-Ray Emission from the Galactic Centre with H.E.S.S.' PhD thesis. Friedrich-alexander-Universitaet, 2023 (cited on page 96).

[114] Siming Liu et al. 'Stochastic Acceleration in the Galactic Center HESS Source'. In: *The Astrophysical Journal* 647.2 (2006), p. 1099. DOI: 10.1086/505171 (cited on page 107).

[115] S. P. Reynolds. 'Supernova remnants at high energy.' In: 46 (Sept. 2008), pp. 89–126. DOI: 10.1146/annurev.astro.46.060407.145237 (cited on page 107).